Wrocław University of Technology
Institute of Computer Engineering, Control and Robotics

Multimodal image processing in cytology

(Ph.D. dissertation)

Łukasz Mirosław

ADVISOR:
Prof. Dr. Ignacy Dulęba

WROCŁAW 2006

Contents

Introduction

The aim of this dissertation is to present dedicated algorithms of image processing developed to meet specific tasks related to identification and classification of multiple objects in images. Such needs appear more and more frequently e.g. in automated screenings and examinations in medicine and biology. The essence of the presented approaches was to infuse the well tested algorithms of image processing, pattern recognition, etc. with the problem specific knowledge. The problem domain was constrained by the analysis of images of cells acquired with different microscopy techniques that define a multimodal input data.

Multimodal images are generated when an object is visualized with more than one detector. In cytology, where cells are studied with different observation techniques, phase contrast and fluorescence microscopy play an important role. The phase contrast microscopy enables to observe living cells while the fluorescence microscopy allows to visualize structures of interest within the cell. In medical and biological researches, where large number of microscopy images (hundreds of thousands) has to be examined, the automated image processing algorithms seem advisable. The dissertation is focused on two research fields, where such algorithms are strongly desirable, namely study of gene functions and the cervical cancer diagnosis.

One of the key aspirations in system biology is to study the role of genes in organisms using high-throughput research techniques. Many experiments that quantify changes in the cell behavior in response to a given perturbation are based on the image analysis. The mitotic index is the crucial parameter that describes the cell cycle and is often used to examine cell proliferation. In high-content screenings its automated quantification is necessary to provide results in an acceptable time.

A cervical cancer is the second most frequent type of cancer among women worldwide and the first in many developing countries. Standard screening techniques, while successful in reducing the mortality, still have serious drawbacks among which misdiagnosis is the most significant. Therefore, alternative methods are search for. One among a few promising options is to study cervical smears with the use of the phase contrast microscopy. Practically immediate, this technique allows to diagnose numerous diseases at a reasonable price. The critical factor is the fast degradation of samples (it dries up after 3-4 hours) what necessitates digital recording of samples. As the method is intended for screening purposes and involves checking a huge amount of recorded samples, it is essential to provide an image analysis algorithm that will automate the task and unburden physicians from massive and messy selection process.

Before dedicated algorithms were developed, a considerable attention was paid to mine the problem domain knowledge, i.e. to understand the optics and microscopy principles and to discover specificity of images. Following the Occam's razor principle, *entia non sunt multiplicanda praeter necessitatem*, the simplest and literature-based solutions were tested at first. As the collected experience indicated, none of the standard methods performed satisfactory and each stage of the analysis flow needed to be revised to carry as much domain-specific knowledge as possible. Also, the analysis of single modalities was to no avail. Difficulties arise from the fact that analyzed images contain real, often noisy and contaminated objects with various appearance, size and structure. Their analysis has induced special considerations of the flow of the analysis.

Thus, the holistic approach is proposed where each step of the analysis was considered equally important. Incorporation of multimodality extended the range of possible solutions. It was possible to construct an original flow of dedicated algorithms that comprise already known techniques adapted to considered problems and combined with novel methods.

Current trends in microscopy prefer rather a passive visualization where images of specimen are taken automatically without paying any attention to their content. Such an approach is far from being optimal because many images are not always informative. This particular problem can be solved by active vision based microscopes (robots) which can be feedback controlled by the image analysis sys-

tem. The introduction of such systems will be possible when image analysis systems provide reliable accuracy and satisfactory performance. Algorithms presented in this thesis are intended to conform these requirements and can be considered as the first step toward image feedback-driven systems.

The interdisciplinary range of the dissertation and intended necessity of being self-contained has induced the introduction of numerous concepts from medicine and biology. They are collected in Chapter 1. Additionally, the most important biological and medical terms are explained in the glossary supplementing the thesis. Notations and the index of frequently used terms were also included. Chapter 2 contains a review of different concepts in segmentation of medical and biological images. A considerable attention was paid to revise methods in the field of segmentation of medical images and Markov Random Fields.

The system presented in Chapter 3 is aimed to support gene functions study by measuring a mitotic index from multimodal images acquired from two different sources, namely the phase contrast and fluorescence microscopy. Determining the value of this parameter is achieved by a selective detection of three types of cells in a novel manner. Correlation-based method detects mitotic cells from phase contrast images while normal and dead cells are detected from both modalities by dedicated pre-processing techniques followed by the watershed segmentation. Classical methods, such as filtering in the Fourier space and the rolling ball algorithm were adapted to the image domain to remove selectively unimportant information such as background, noise or image regions with low fluorescence signal. Further, the importance of the filtering stage was justified by a suitable example. In Chapter 3.2 an innovative cascade of classifiers is built to detect mitotic cells. The correlation-based detection algorithm is applied to form a list of candidate objects and originally developed gradient and evolutionary based validation methods are applied to analyze candidate correlation peaks more precisely to improve performance of the detection process.

The image processing algorithm, presented in Chapter 4, is aimed to support cervical cancer screenings by providing to a physician filtered images with unimportant objects excluded. An original approach exploits Statistical Geometrical Features to characterize classes of image regions that contain epithelial cells, contaminated medium and cell membranes. Sequential Forward Floating Selection is employed to identify the most representative features. Different feature selection criteria (scatter matrices, misclassification rate and Bhattacharyya distance) and different classifiers (Fisher Linear Discriminant, k-nearest-neighbor classifier and Kernel Fisher Discriminant) are compared to justify the proposed method. The shape of cells is identified with post processing techniques followed by the application of an active contour model. Alternative methods such as segmentation with Markov Random Fields are also evaluated. The thesis is concluded with Chapter 6.

Despite the presuppositional advantage of the multimodal analysis of images over standard approaches where single modes are considered, the empirical analysis of its efficiency needs to be derived. The dissertation raises this issue partially by restricting the evaluation only to a given problem domain defined by the microscopy technique and cell type. Results of this thesis are applicative. Algorithms presented in Chapter 3 were implemented and applied in biological experiments performed in Max Planck Institute of Cell Biology and Genetics, Dresden, Germany. Software used in experiments is presented in Chapter 5. Algorithms presented in Chapter 4 were successfully used as a first stage in the system that identified atypical cells in images of cervical smears. Experiments performed by Grzegorz Głąb MD, PhD and Marcin Smereka in Diagnostic Center of Obsterics and Gyneacology, Opole, Poland further justified the importance of the filtering stage and may improve the cervical cancer screenings.

advice when necessary. Gabi, Anne, Indrani, Mikolaj, Maciek, Antonio and all the members of the Buchholz Lab that made a great environment for research. Frank Buchholz for the invitation to work in his group, showing interesting challenges and continuous support and help in getting a scholarship. Laurence and Ralf for cooperation and images to analyze. Karol Kozak for discussions on various aspects of statistics, machine learning, new ideas and life in general. Irena, Ganka, Normund and Eckhard for a great time when we crowded one lab. Edmund for many discussions and technical support. I also learned a lot from Alireza, Michael and Khaled - my room mates. Prof. Rafajlowicz, the former head of the Institute of Engineering Cybernetics, for granting a one-year PhD scholarship. I also wanted to express my gratitude to Prof. Siegfried Fuchs, the former chair of Image Processing and Recognition group at the Dresden University of Technology, for the invitation to work in his department and creating supreme research conditions. Many thanks to former members of the group (Boris Flach, PhD and Dmitrij Schlesinger, PhD) for giving me insights into Markov Field Models. An important character in the group was my office and discussion-mate, Falk Uhlemann. Falk taught me many image processing tricks and showed a remarkable leniency to my German. I also thank Tanja Schilling for implementation and evaluation of methods presented in Chapter 4. I also thank Mayte Pisabarro, a group leader of Structural Bioinformatics at the BIOTEC for the invitation to join her group which helped me during my last months of my PhD. I also thank all of the group members, especially to Mandy for helping me out with the "red tapism". I cannot forget about my colleagues from my home Department of Fundamental Cybernetics and Robotics at the Wroclaw University of Technology. Thank you for your friendliness and many good remarks and comments. I would like to express my special gratitude to Artur Chorazyczewski for many fruitful discussions, contribution to the method presented in Chapter 3 and proofreading. I also obliged to Grzegorz Glab, PhD, MD and Marcin Smereka for cooperation in the cervical cancer diagnosis project.

Last but not least, many thanks to my family, especially my wife and daughter, my parents and parents-in-law for their continuous support during this time. Without you I would have never gone that far.

Notations

Some of the most commonly used notations are collected below. Standard conventions are exploited, for example a vector is denoted by a lower-case quantity in bold face and a matrix by upper case.

Bayesian Model:

$\Omega = \{\omega_1, \ldots, \omega_C\}$	class set
ω_i	label of class i
$\mathbf{x} = (x_1, \ldots, x_d)$	a measurement vector, a pattern or observation vector
n	number of samples $\mathbf{x}$
n_i	number of samples $\mathbf{x}$ in ω_i
P(x),p(x)	probability, density function of random variable x
g(x)	discriminant function
$P(\omega_i)$	prior probability of the given class ω_i
$P(x|y)$	conditional probability

The Markov Random Field model:

$\mathbb{F}$	set of all possible configurations
$\mathcal{C}$	cliques set
$\mathcal{N}$	neighborhood set
$S = \{(i,j) : 1 \le i, j \le N\}$	set of sites
$L = \{l : l = 1, 2, ..., N_L\}$	label set
#L	number of elements in L
$I(\cdot, \cdot)$	image of size $N \times M$
I(x,y)	intensity value at position (x,y)
$X = \{X^i, i = 1 \ldots n_e\}$	population
$\phi(X)$	fitness function
$Tr(\cdot)$	trace operand of a given matrix.
$\|A\|^2 = \sum_{ij} A_{ij}^2$	
I_T	template of the size $M \times M$
$c(\cdot, \cdot)$	correlation map
$e(\cdot, \cdot)$	edge map
$\zeta(\cdot, \cdot)$	vector field

1. Biological Background

Cell is the smallest unit in a living organism that is capable of integrating essential life processes. The schematic cell structure is presented in Fig.1.1. Structures of interest for algorithms presented in latter chapters are nucleus, cytoplasm and the cell membrane. The entire process of cell division including division of the nucleus and the cytoplasm is called mitosis. A dividing cell is called mitotic.
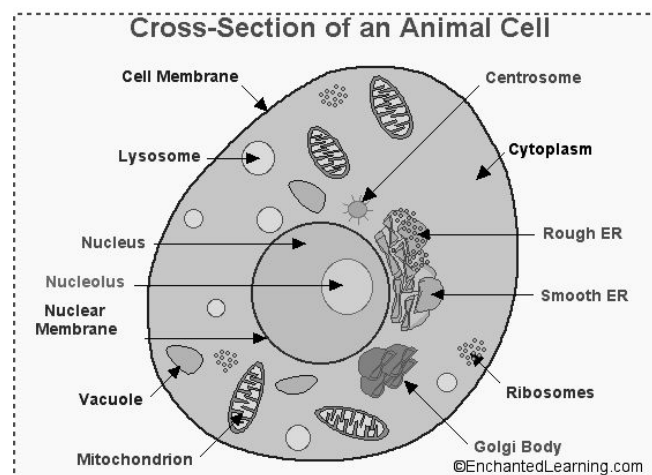

Figure 1.1. Scheme of a cell

Cells are transparent by their nature and, therefore, for their observation specialized microscopy techniques need to be applied. Phase contrast is the least toxic method that does not require staining. When the light passes trough a transparent part of the specimen, it is shifted (diffracted (D) wave) in relation to the uninfluenced light (surround (S) wave) and arrives about a quarter of a wavelength out of phase. This difference in phase is not detectable by the human eye. However, the change in phase can be increased to $1/2$ wavelength by a transparent phase-plate in the microscope and thereby causing a difference in brightness (particle (P) wave). Due to destructive interference, the transparent object appear darker against a lighter background. This is called dark or positive phase contrast (Fig.1.3(a)). Another possibility is to slow down the direct light so that the influenced light and unobstructed light arrive in step and interfere constructively. As a result the specimen appear brighter than a background (Fig.1.3(b)).

Automated interpretation of images with biological structures from phase contrast microscopy is difficult. Correct adjustment of the microscope is necessary to exploit the microscope's full potential and ensure the uniform and free from glare illumination (for example through the Kohler illumination). However, the phase contrast microscope generates phenomena such as shade-off effect or halos that are unavoidable with manipulations with microscope optics. Shade-off and halo effects are a natural consequence of the phase contrast optical system. Bright phase halos usually surround the boundaries between large fragments of the specimen and the medium (Fig.1.4). Halos occur in phase contrast microscopy because the circular phase-retarding ring located in the objective phase plate also transmits a small amount of diffracted light from the specimen. The shade-off phenomenon occurs because central parts of the specimen, having uniform thickness, diffract light differently than the highly re-

(a) Phase contrast microscope.

(b) Fluorescence microscope.
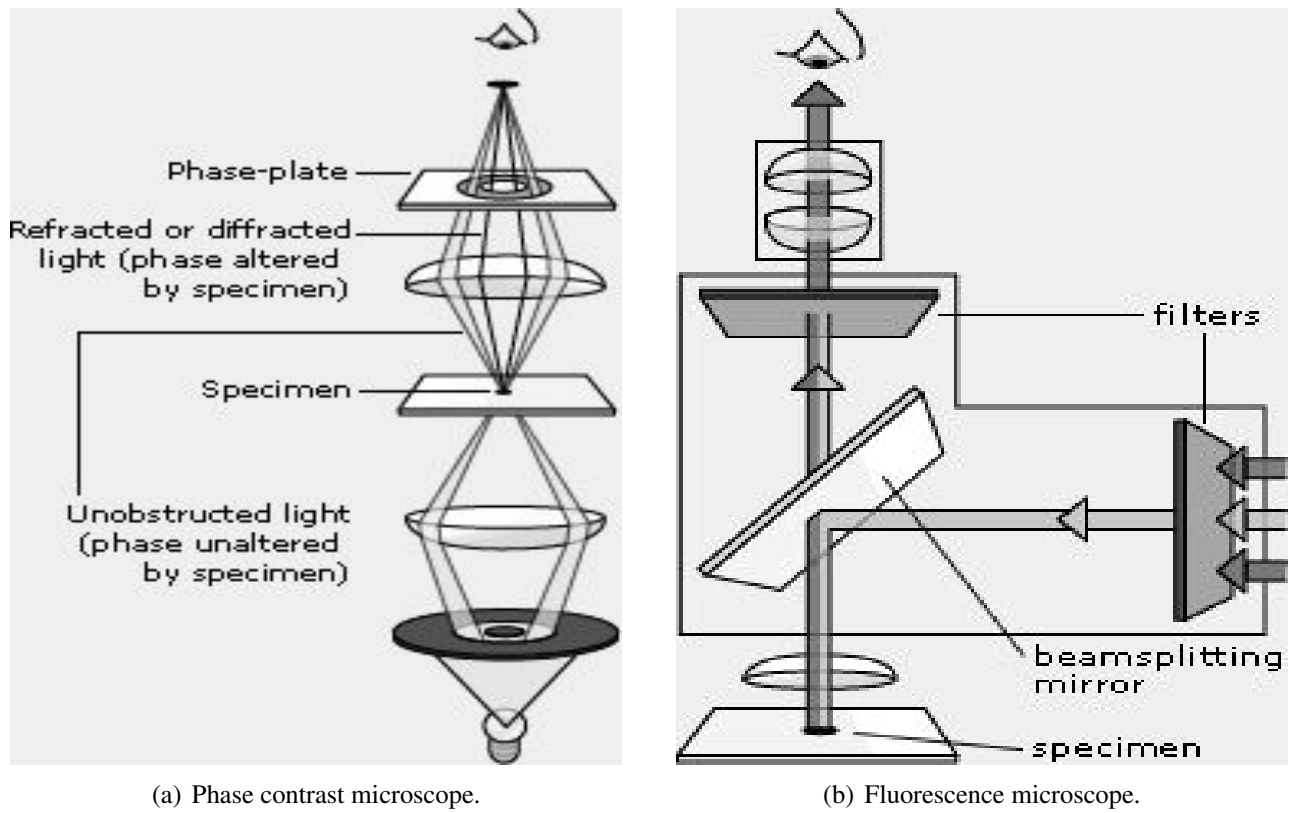
Figure 1.2. Principles of phase contrast and fluorescence microscopes. Source: nobelprize.org

(a) Positive phase contrast
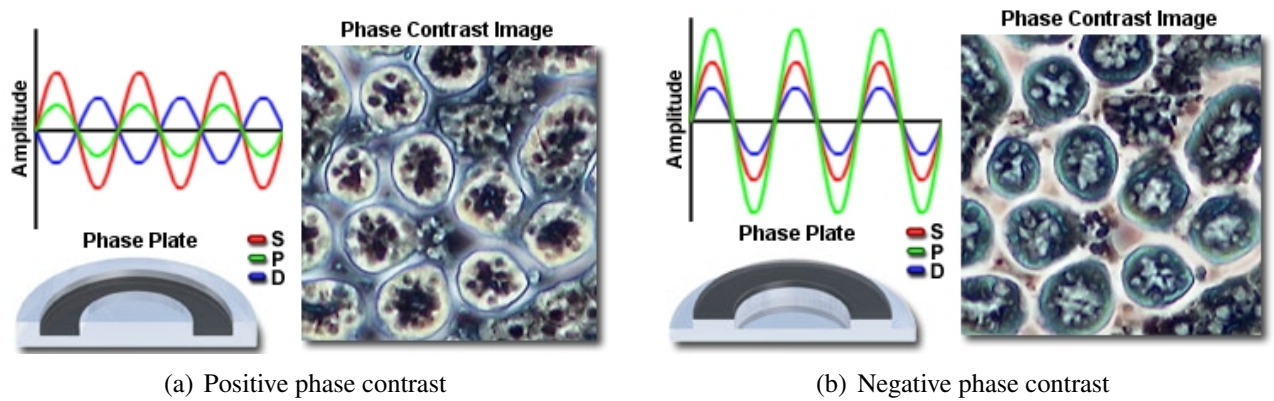
(b) Negative phase contrast

Figure 1.3. Negative and positive phase contrast of a kidney tissue. Source: Nikon MicroscopyU

fractive zones at edges and boundaries. While halo effect may simplify detection of the mitotic cell by enhancing boundaries between the specimen and the medium, shading off phenomenon makes the boundary between the cell and the medium hard to detect.

Another effect present in phase contrast images is uneven illumination. It manifests itself by the gradient in light intensity that traverses from one side of the image to the other. It is caused either by a wrong adjusted optical system or by the meniscus of the medium. The magnitude of this effect depends upon the magnification zoom ratio, but usually appears with one side of the image being much lighter than the opposite one. Consequences of above mentioned effects should determine the selection of applied image processing algorithms. Classical methods do not perform well on phase contrast images (see Chapter 4) and more sophisticated methods could avail [88].

When a specific component of the cell need to be observed, a different microscopy technique should be employed. Fluorescence microscopy is used to study specimens, which can be forced to fluoresce. It is based on the phenomenon that certain materials emit energy detectable as visible light when irradiated with the light of a specific wavelength (see Fig.1.2(b)). Many different fluorescent dyes can be used to stain different structures of a cell. Green Fluorescence Protein (GFP) can be fused on DNA level to the structure of interest. It is not toxic and, therefore, is widely used by biologists. Other stains are used to visualize nuclei. The 4'-6-Diamidino-2-phenylindole (DAPI) is known to form fluorescent complexes with the DNA in nuclei while the antibody histone H3 stains only those nuclei that undergo mitosis. Two of the latter stains are used in the experiments presented in Chapter 3.

Figure 1.4. An example of the halo effect (the round cell in the bottom center) and hard detectable cell membrane (the cell in the center)

Undesired effects in fluorescence microscopy that most contribute to the final image quality are uneven illumination and noise. The first phenomenon is formed by a meniscus, i.e. curved upper surface of the medium. The light that passes the meniscus is reflected differently and as the result the image is illuminated in a different manner. The noise, as generally random, reduces and increases the image brightness in each pixel position. It may be generated due to instability in a light source or image detector itself. Also charged couple device that detect photons include those that are present in the dark current in the device itself. Although these types of noise can be reduced by careful microscope design and proper wiring, there is an irreducible amount of noise superimposed on the signal when the image of the specimen is readout by the camera, amplified and digitized [86]. It is caused by the differences in arrival time of light to the sensor.

2. Literature Review

2.1. Segmentation of medical/biological images

Segmentation is a fundamental image processing technique. It has been successfully applied in medicine and biology automating or facilitating the delineation of anatomical and cytological structures. It partitions image into homogeneous regions that share a common feature such as brightness, texture, motion or shape, and simplifies further processing.

Segmentation can be regarded as a classification task. Image contains different areas that need to be assigned to different classes based on a classification strategy. Given a feature vector $\mathbf{x}$ and classes set $\Omega = \{\omega_i, i = 1...C\}$, where C denotes the number of classes, a decision rule based on probabilities can be stated as

Definition 1. *assign* $\mathbf{x}$ *to* ω_i *iff*

$$\forall j \neq i \quad P(\omega_i|\mathbf{x}) \geq P(\omega_j|\mathbf{x}). \tag{2.1}$$

The *a posteriori* probability $P(\omega_i|\mathbf{x})$ can be expressed using Bayes' theorem as follows

$$P(\omega_i|\mathbf{x}) = \frac{P(\mathbf{x}|\omega_i) \cdot P(\omega_i)}{P(\mathbf{x})} \tag{2.2}$$

where $P(\omega_i)$ and $P(\mathbf{x}|\omega_i)$ denote *a priori* probability and the class-conditional probability respectively and

$$0 \neq P(\mathbf{x}) = \sum_{i=1}^{C} P(\mathbf{x}|\omega_i) \cdot P(\omega_i). \tag{2.3}$$

Therefore a rule based on Def.1 can be written as

Definition 2. *assign* $\mathbf{x}$ *to* ω_i *iff*

$$\forall j \neq i \quad P(\mathbf{x}|\omega_i) \cdot P(\omega_i) > P(\mathbf{x}|\omega_j) \cdot P(\omega_j). \tag{2.4}$$

The rule is known as Bayes' rule for the minimum error. A classification rule can be also defined with discriminant functions $g_i, i = 1, \ldots, C$ of the pattern $\mathbf{x}$. In the case of C classes, the pattern is assigned to the class with the largest discriminant:

Definition 3. *assign* $\mathbf{x}$ *to* ω_i *iff*

$$\forall j \neq i \quad g_i(\mathbf{x}) \geq g_j(\mathbf{x}). \tag{2.5}$$

The optimal discriminant function can be defined as

$$g_i(\mathbf{x}) = P(\mathbf{x}|\omega_i)P(\omega_i)$$

which leads to the Bayes' decision rule but there are also other discriminant functions that lead to the same decisions [108]. The main difference between the discriminant functions and the Bayes' decision rule is that the form of discriminant functions is well defined and it is not imposed by class-conditional

distributions. Discriminant functions can be constructed based on *a priori* knowledge about patterns used or can be given analytically. Their parameters can be adjusted in a training procedure. Many different forms of discriminant functions were proposed in the literature but their discussion goes beyond the scope of this thesis. Interested reader is referred to [21, 108].

Segmentation methods can be divided into classes based on techniques. The simplest include edge detectors such as first derivative Roberts, Prewitt, Sobel or Frei-Chen operators, compound operators such as first derivative of Gaussian, or second derivative operators such as Laplacian [80, 96]. Other standard methods examine the image histogram, applied either to a single color band (gray level image) or a multiband image (color image). In general for light microscopy images, it is advisable to threshold stained nuclei in HSI space (three channels corresponding to Hue, Saturation and Intensity planes). The hue plane identifies where a particular stain is located, the saturation plane indicates amount of the stain while the intensity plane correspond to overall density of stained specimen [86]. In the case of texture segmentation, image thresholding may be sufficient provided additional operators are applied beforehand, such as Laplacian or Hurst operators. Generation of simple statistics from the image, such as variance or range may also provide different textures [86].

Morphological image processing techniques modify either a spatial form or a structure of objects in images. Originally developed for binary images the morphological basic operators such as dilation and erosion are now extended with hit-or-miss transformations or more sophisticated methods like shrinking, thinning, skeletonizing and thickening operations that enhance desired image features. These methods can be also applied to gray scale images but with some limitations. For example, the background and objects should be distinct and spatially smooth [80].

The morphological methods often fail in the case of significant global non-uniformity which manifests itself as the intensity gradient crossing the image, not visible in visual scene. In microscopy shading may originate from sample curvature, non-uniform illumination, imperfect, dirty or dusty optics, uneven spatial sensitivity of the sensor, dark-level camera response and/or camera nonlinearity [86].

Tomazevic et al. [97] evaluated and compared different retrospective *shading correction methods*. The problem of finding a shading free image I_U from the acquired image I is equivalent to deriving the inverse of the degradation model f^{-1} that can be applied to acquired image yielding a shading free image:

$$I_U = f^{-1}(I). \qquad (2.6)$$

A simple affine approximation of this model is often used:

$$I = I_U \cdot S_M + S_A \qquad (2.7)$$

where S_M and S_A correspond to the multiplicative and additive shading component, respectively. The problem is thus concerned with finding estimates of these components. Linear filtering technique assumes that only an additive component is present and it can be determined by a low-pass filter. Homomorphic filtering derives a multiplicative component and involves low-pass filtering of the logarithm of the acquired image. Morphological filtering assumes that objects of interests are limited in size and larger than the scale of background variations. Moreover, there should be a contrast in intensity between objects and a background. Under these circumstances, morphological operator may be used to filter out object and thus deriving an object-free estimation of a background. Non-parametric non-uniform intensity normalization searches for a smooth multiplicative field that maximizes frequency content of the intensity distribution. Parametric methods include surface fitting methods where intensity at points from background or an object class are used to estimate a background surface[97]. Because a manual selection of points is often a tedious task, an automated approaches have been proposed. For example one of the methods divides an image into grid of equal rectangles and representative points correspond to mean, median, minimal or maximal value in each rectangle [86].

The entropy minimization method assumes that shading increases entropy of the shading-free image.

Minimization of the entropy of the transformed image, where shading components are modelled by the second order polynomials, should result in the optimal corrected image. Tomazevic et al. [97] concluded that the method based on the entropy minimization is the most robust and insensitive to noise. However, it is also computationally expensive. Linear, homomorphic and morphological filtering methods are suitable for correcting images that contain small objects, thus can be applied to microscopic images with an appropriate magnification. Advantages of these methods result from a simple implementation and low computational costs. Parametric methods performed well on images with small- and medium-sized objects but the selection of representative points and suitable parameters may be troublesome. In the case of small objects, average filtering with sufficiently large mask results in a shading-free image [71].

Robust Automatic Threshold Selection [50] segments an image by using a local image statistics in 3D and 2D images with shading. Kittler et al. noticed that the threshold value is optimal for noise-free images. Additionally, an example of biased threshold value in case of images with Gaussian noise is provided.

Once an object of interest is segmented it is possible to measure its shape properties. *Shape descriptors* are used in image processing domain as a tool to determinate similarity between shapes and description of local properties of the shape. Global models describe a shape as a set of features or parts. Common descriptors rely on spherical harmonics [104], deformable regions, shock graphs [91], shape contexts or wavelet decomposition [3]. Fourier descriptors date back to Zahn's work [114], where a parametrized curve function is expanded into a Fourier series. The set of modules of the coefficients are called Fourier descriptors. They are invariant to the following transformations: translation or rotation of the shape, change of its origin or scale. The method also has its disadvantages. For instance, one cannot guarantee that a simple closed curve will be rendered reliably after truncating the set of Fourier descriptors. Sometimes, the curve generated has one or more crossovers.

The basic idea behind shape contexts [3] is following. Given a set of points from an image (e.g. extracted from a set of detected edge elements), the shape context captures the relative distribution of points in the plane relative to each point on the shape. Specifically, a histogram using log-polar coordinates is computed. Thus descriptors are obtained that are similar for homologous (corresponding) points and dissimilar for non-homologous points.

Other family of features used in segmentation is derived from the analysis of the image texture. Textures have proved to reflect human visual processes [99]. Among brightness, color and form, a texture belongs to important discrimination cues for human. An image texture defined as spatial variations in pixel intensities has been the subject of numerous research. They have been used in medical applications, such as digitized mammograms [90], analysis of ultrasound images [14], X-ray images [61], evaluation of bone structure in MR images [40]. Many examples such as remote sensing, document processing, automated inspection, analysis of Synthetic Aperture Radar images and medical image processing one can find in the Tuceryan's review paper [99]. There are three types of applications where texture features can be used: texture classification (identification of previously known texture classes in the image), texture segmentation (separation of regions in the image which have different texture regions and identify boundaries between them) and texture synthesis (used in image compression algorithms and image graphics where realistic surfaces need to be generated). The texture classes need not to be recognized in the latter case. Another instance of tasks called *shape from texture*, is aimed at extraction of 3D object shape from various cues such as texture, shading and stereo. Texture features fall into numerous families. The following groups can be enumerated: statistical, geometrical features and features derived from model based methods. However, these families are not independent [30]. The first family, statistical methods, take into account a statistical distribution of pixel intensities. Haralick [39] suggested the use of gray level co-occurrence matrix which has become a popular in definition of texture features such as energy, entropy, contrast, homogeneity or

	actual positive	actual negative
predicted positive	TP (true positive)	FP (false positive)
predicted negative	FN (false negative)	TN (true negative)

Table 2.1. Confusion matrix

correlation. These features suffer from many drawbacks and the choice of parameters of the method as well as computational effort is still investigated. Autocorrelation features inform about the repetitive nature of placement of texture elements in the image. They can be used to assess the texture coarness and fineness. Moreover, they are also related to the energy spectrum of the Fourier Transform which further indicates the texture directional properties.

The second family of features, geometrical methods, characterize a texture by means of geometric properties of its primitives (texture elements). Voronoi tessellation features are extracted from properties of Voronoi polygons. A significant difference in features indicates a texture edge. The method successfully segmented gray level texture images as well as synthetic textures [98]. Model based methods rely on construction of any image model that not only describes the texture but also can be used to synthesize it. Model parameters describe important texture features. Ahuja and Schachter [1] divided image models based on different levels of abstraction and defined them as a description that captures only relevant image features and leaves other ones unspecified. Low-level models characterize spatial variations in intensity and include pixel-based and region-based models. High-level models involve semantic description. Pixel-based models require that values of the variables (pixels) meet certain constraints. If all the variables are considered independently and values are constrained individually, the result is a random noise. If values of variables are generated independently from the Gaussian distribution, the result is the Gaussian noise. Such models do not consider spatial arrangements of pixels and therefore are not interesting for most of natural textures.

As model based methods have proved to be efficient in segmentation, they were also tested in segmentation of phase contrast images. The concept of a random model is introduced in Section 2.1 while its evaluation study is presented in Chapter 4 where a simple multi-logistic model was tested with two minimization techniques: Iterated Conditional Modes (ICM) and Gibbs sampler.

Evaluation of segmentation methods The evaluation of image processing systems justifies their applicability and allows to optimize their behavior. Therefore, it is desirable to define measures of systems' performance with respect to specific needs.

Detection of a cell can be considered as a binary decision problem where a classifier labels objects either as positive or negative. The decision made by the classifier can be represented in the framework known as a confusion matrix or contingency table. The confusion matrix comprises four categories: True positives (TP) are examples correctly labeled as positives. False positives (FP) refer to negative examples incorrectly labeled as positive. True negatives (TN) correspond to negatives correctly labeled as negative. Finally, false negatives (FN) refer to positive examples incorrectly labeled as negative. From the confusion matrix coefficients called sensitivity and specificity can be calculated. The first parameter measures the fraction of negative examples that are misclassified as positive. The second one measures the fraction of positive examples that are correctly labeled. They are defined as follows:

$$sensitivity = \frac{TN}{TN+FP}, \tag{2.8}$$

$$specificity = \frac{TP}{TP+FN}. \tag{2.9}$$

Sensitivity and specificity are also known True Positive Factor (TPF) and False Positive Factor (FPF). Trace of the confusion matrix defines the accuracy of a given method. Large values (approaching 1) of mentioned parameters are preferred.

Markov Random Fields

Graphical modeling provides a mathematical framework that represents the logical structure of a joint probability distribution in the form of a network or graph. The graphs can be either directed, such as Bayesian Networks, or undirected, such as Markov Random Field (MRF). Contrary to one-dimensional time series models that are not particularly useful in image analysis, MRF models are able to constraint pixels in two-dimensional neighborhood i.e. that pixel intensity depends only on its neighborhood. The method was also adopted for image analysis within the Bayesian framework [34] where the model is able to capture significant physical characteristics of the scene. Such an approach is useful when dealing with images that reflect a known physical phenomenon.

Often it is not possible to relate spatial variation to a known physical process. In such cases, a variety of schemes may be used to specify the relationship between image features. The term "field" associates a value of property of interest with a co-ordinate system. Hidden Markov Models refer to those MRF where parts of the nodes (variables) are not observed or missing.

MRF models are constructed from observed values. In image processing observed values correspond to pixel intensities. These values are related by a stochastic function to the values of interests, here labels of individual pixels that form a segmented image. Therefore an image segmentation can be considered as a labeling process that is more general and therefore it can be described as an optimization problem. MRF are models that define a joint probability distributions between observation sequences (pixel intensities) and their corresponding label sequences defined as random variables. In order to define the joint distribution, models have to enumerate all possible observation sequences. This task is often intractable because the number of all observed sequences is enormous (for a binary image of the size 300×300, the number of possible segmentations is equal to $2^{300 \times 300}$), unless elements in observation sequences (unlabeled pixels) are represented as independent one from another.

As MRF will be tested in Section 4.2 this model is presented in details following Li's work [57]. Let $S = \{(j,k) : 1 \leq j,k \leq N\}$ denote a rectangular lattice of sites that correspond to pixels of an $N \times N$ image in the 2D plane. A segmentation task, also termed as a labeling task, is to assign a label from the label set L to each of the sites in S. To each site $i \in S$ a function with domain S and segmented image L assigns a unique label (Fig.2.1)

$$f : S \rightarrow L.$$

The set of all possible configurations, also called the configuration space, is denoted as $\mathbb{F}$ ($\mathbb{F} = L^{N \times N}$).

For binary images $L = \{l : l = 0 \lor l = 1\}$ while for gray-level images $L = \{l \in \{0, N_L\}\}$ ($N_L = 255$). In a multiclass segmentation task $L = \{l : l = 0, 1, ..., N_L\}$ for N_L different segments. In vision, a labeling or configuration f corresponds to segmented image.

Definition 4. *A neighborhood system $\mathcal{N} = \{\mathcal{N}_i, \forall i \in S\}$ is a collection of subsets of S for which*
  1. a site is not neighboring to itself: $i \notin \mathcal{N}_i$
  2. the neighboring relationship is mutual: $i \in \mathcal{N}_{i'} \Leftrightarrow i' \in \mathcal{N}_i$

$\mathcal{N}_i$ is the set of sites neighboring i and

Definition 5. *A clique c is a subset of S for which every pair of sites are neighbors.*

Definition 6. *A clique set C in the neighborhood system $\mathcal{N}_i$ is $C = \{c | c \subset \mathcal{N}_i\}$*

Definition 7. *A random field is the MRF with respect to the neighborhood system $\mathcal{N}$ iff*

(a) A labeling of sites can be considered as a mapping from the set of sites S to the set of labels L.

(b) Neighborhood and cliques on a lattice of regular sites.
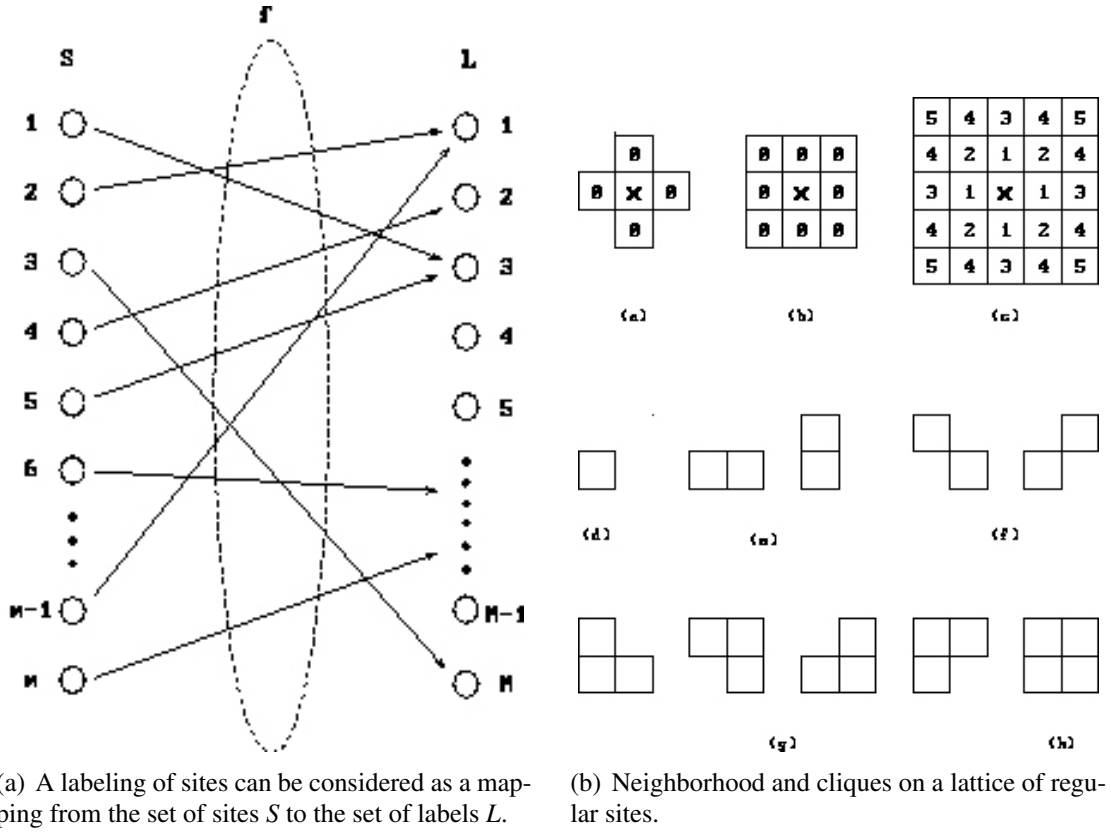
Figure 2.1. Labeling and neighborhood systems. Source [57].

1. $P(f) > 0$ *for all $f \in \mathbb{F}$ (positivity)*
2. $P(f_i|f_{S-i}) = P(f_i|f_{\mathcal{N}_i})$ *(Markovianity)*

where $S - i$ is a set difference, f_{S-i} is the set of labels at the site $S - i$ and $f_{\mathcal{N}_i} = \{f_{i'}|i' \in \mathcal{N}_i\}$.

Definition 8. *f is the Gibbs Random Field (GRF) with respect to the neighborhood system $\mathcal{N}$ iff*

$$P(f) = \frac{1}{Z} \exp \left(-\frac{1}{T} U(f) \right) \tag{2.10}$$

where $Z = \sum_{f \in \mathbb{F}} \exp \left[-\frac{1}{T} U(f) \right]$ is a normalizing constant. $U(f) = \sum_{c \in C} V_c(f)$ is the total energy function and $V_c(f)$ denotes a potential function. $P(f)$ measures the probability of the occurrence of a particular configuration f. The more probable configurations are those with lower energies. A particular MRF model tends to favor the corresponding class of configurations, by associating them with larger probability than others. The temperature parameter T controls the sharpness of the distribution. When the temperature is high, all configurations tend to be equally distributed. Near the zero temperature, the distribution concentrates around the global energy minima.

The MRF is characterized by its local property (the Markovianity) whereas GRF is characterized by its global property (the Gibbs distribution). These two properties are related with each other by the Hammersley-Clifford theorem.

Theorem 1. (Hammersley-Clifford) *A random field f is the GRF with respect to the neighborhood system $\mathcal{N}$ iff f is the MRF with respect to $\mathcal{N}$.*

Its proof can be found in [34]. The theorem sets the equivalence between MRF and GRF and allows to use GRF to represent the corresponding MRF. Alternatively, the theorem provides a way to define a joint probability using the knowledge of conditional probability for a neighborhood at the points.

There are many models to define the energy function $U(f)$ [57]. The simplest auto-models derive contextual constraints on two labels coded as pair-site clique potentials. They are widely used due to their simple form and low computational costs. The models can be also classified according to assumptions concerning the label set. In an auto-logistic model labels take values from a discrete label set. When a neighborhood system is defined on a lattice (4 nearest neighbors 2D lattice or 2 nearest neighbors for 1D lattice), the auto-logistic model is reduced to the Ising model [57]. An auto-model becomes an auto-binomial model if labels can attain multiple values. An auto model is said to be an auto-normal model, also called a Gaussian MRF , if the label set is a real line and the joint probability is multivariate normal. The auto-logistic model can be generalized to the multi-level logistic model also called Strauss process or the generalized Ising model. The model assumes that clique potentials depend on their size, location and orientation as well as on a local configuration of the neighborhood system. Labels take values from a label set. The energy function is positive if all sites of a clique have the same label and negative one otherwise.

In vision applications it is reasonable to assume a smoothness prior. This prior states that the evolution of physical processes is not sudden and generally does not change abruptly. The temporal and spatial changes usually exhibit a coherence and smoothness. For example many objects in human environment have the same textures pattern. It is also very likely that in medical images background pixels will lie adjacent to other background pixels. Likewise, the object (cell, particle) pixels will be located in the neighborhood of other object pixels.

It has been developed into a general framework called regularization. Smoothness prior is usually incorporated into a model by an additional prior probability or an energy term measuring an extent to which the smoothness assumption is violated by labels. In regularization, an energy consists of smoothness and closeness terms, that impose constraints from data, and the minimal solution is a compromise between the two constraints allowing a conversion of ill-posed problem into well-posed problem. In the Hadamard sense an ill-posed problem is a problem if its solution (1) does not exist, (2) is not unique or (3) does not depend continuously on initial data [57]. Good examples are surface reconstruction and interpolation.

The aim of the MRF estimation is to find the most likely realization of the segmentation field f given observed field I (image). It can be achieved within the maximum a posteriori (MAP) framework. The MAP-MRF framework, advocated by Geman and Geman [34], is a special solution in the Bayes framework and minimizes an energy function which is equivalent to maximizing the posteriori conditional probability distribution (Gibbs distribution in this case).

$$\hat{f} = argmax_{f \in \mathbb{F}}\{P(I|f)P(f)\} \qquad (2.11)$$

where $\hat{f}$ denotes a true labeling of the MRF f. To simplify calculations the number of pixel classes is often estimated a priori but the computation of $P(I|f)$ requires the estimation of model parameters. The expectation maximization approach [92] is a standard method to estimate parameters of the model when available data are insufficient or incomplete. It consists of two steps: the expectation step where the current expectation formula is calculated with respect to unknown variables and the maximization step where the new estimate of parameters is calculated. Once, model parameters are estimated, the calculation of MAP criterion can be performed. If the energy function is convex the global minimum is obtained by deterministic algorithms, such as ICM proposed by Besag [6]. For non-convex energy functions sampling methods are usually employed, for example the Gibbs sampler [34] or the Metropolis sampler [63]. With the use of annealing scheme [49] convergence to the global minimum is guaranteed [34].

MRF models have been used in many areas of speech recognition and image processing. Genovese [35] presented a statistical model of functional magnetic resonance imaging data incorporating the noise process and structure of time dealing with drift and changes in shape of hemodynamic response.

The author admitted, that the algorithm fitting model parameters via Markov Chain Monte Carlo simulations is computationally intensive. Comparison of convergence methods by Cowles [17] stated that none of thirteen methods perform well when applied alone and a combination of strategies was recommended. Djafari and Sauer [73] proposed a method to reconstruct X-ray tomographic images from compact binary objects based on a small number of their projections. The coordinates of the of the object are estimated directly from the projections using Bayesian MAP estimation framework of a Gaussian Model. To find the optimal solution, two methods were tested: the global optimization algorithm based on simulated annealing that theoretically is independent on initialization and the local descent-based method based on the ICM method. Both methods work satisfactory but ICM approach may be trapped at local minima.

Cai and Liu constructed a model that segments handwritten numerals and showed its high performance [10]. Flach et al. [25] assumed the Gibbs distribution of a prior model of possible scene segmentation and used the Potts model to segment multi-modal images from magnetic resonance and position emission tomography. Deng and Clausi [19] introduced a function-based weighting parameter between two components into standard two-component segmentation model that automatically estimates model parameters. The energy function was defined as a sum of multi-level logistic model and feature model included data derived from the Gaussian distribution. Gibbs and Metropolis sampler were applied to implement the MAP criterion and Expectation Maximization (EM) algorithm estimated model parameters without training data. Their method was successfully employed in segmentation of Synthetic Aperture Radar (SAR) sea ice images and artificial and real scene color images.

Dias and Leitao [20] presented a method for endocardial (inner) and epicardial (outer) contour estimation from sequences of echocardiographic images. The complete probabilistic model was built within the Bayesian framework. As estimation criterion the MAP was adopted. Authors introduced an algorithm called Iterative Multigrid Dynamic Programming that is fully data driven without ad-hoc parameters. As it name suggests, it embodies iterative, dynamic programming and multrigrid concept.

Kato [46] proposed an unsupervised segmentation method for images with unknown number of pixel classes. He built a Bayesian color space model using the Potts model where the external field (observations) is represented as a mixture of Gaussian distributions while inter-pixel interactions favor similar labels at neighboring sites. The model parameters to be estimated were the hidden label field configuration, the Gaussian mixture parameter, parameters of the MRF and the number of mixture components. The Reversible Jump Monte Carlo Markov Chain Sampler was used to sample the whole a posteriori distribution in order to obtain a MAP estimate via simulated annealing. Although the segmentation results of color real images was impressive, the computation time of segmentation of a single image was long (from 9 min up to 395 min).
Application of MRF in segmentation of epithelial cells in phase contrast images is presented in Sec. 4.2.

Segmentation of cells Santos et al. performed automatic discrimination and quantification of alive and dead cells in phase contrast microscopy with texture features derived from co-occurence matrix and histogram [87]. Once images are automatically segmented, the approximate number of live and dead cells is obtained by dividing each area by the average size of each cell type. The method was tested on three different cell cultures and proved to be reliable. However, the number of cells is approximated from segmented regions and segmentation of each single cells is not possible.

Also in the field of cytology some results seem to be promising. In breast cancer treatment the system detects cancerous-like cells with watershed and morphological operations [103]. Another system use mathematical morphology tools such as watersheds and color information in several color spaces. An extension of watershed as the optimal region-growing operator has been used [56].

Ji et al. presented an algorithm to segment colposcopic images with texture features[44]. The images were preprocessed with the rolling ball algorithm to subtract background, followed by adaptive threshold algorithm that is sensitive to variations in local contrast. Next steps included sceletonization

and detection of line segments and merging of short line segments. The authors chose texture features that optimally characterized cervical textures. Textures were obtained directly from the vectorized image and normalized distributions of length and orientation of previously detected line segments. It was concluded that reduction of feature set (from 24 to 13) decreased the discrimination performance from 87.03 % to 80 % which is acceptable compared to computational saving of almost 40 %.

Segmentation and recognition are usually considered as separated processes. However, there exist models combining both of them. For example a mechanism based on spectral graph partitioning was introduced by Yu[113]. The image is partitioned into patches that are grouped later on. The patch grouping discovers a set of patches that conform best to the object configuration, while the goal of pixel grouping is to find a set of pixels that have the best low-level feature similarity. These two processes were performed as one joint optimization task. The method was evaluated only in the human detection application but results are promising.

Andrade et al. introduced an Interactive Algorithm for Image Smoothing and Segmentation in [18]. They employed a non-linear partial differential equation to smooth the image while preserving contours (anisotropic filter). Then user marks region of interests and sort all pixels in ascending order according to certain criteria. Finally, labels were assigned according to a set of rules (region growing and merging).

Classification of cells in fluorescence images has been addressed in many medical applications. Wurflinger proposed a method based on repeated staining of a cell smear. The correlation of features and data extracted from different stains sufficed to classify cell nuclei and may yield an increase of diagnostic reliability in early cancer detection [110]. Perner constructed an automated image analysis system that detects Hep-2 cells which are used for the identification of antinuclear autoantibodies. The system classifies cells into 6 classes on the basis on most relevant features extracted from fluorescence images [79] with high accuracy. Although successful in certain applications the methods analyze images with stained and fixed cells. Since observed cells are immobilized further extension of applications to include also the analysis of the cell motion and behavior is not possible.

3. Multimodal Image Processing in Gene Function Analysis

Recent publications on human and mouse genome have revealed that the genomes contain 30,000 - 40,000 genes [23]. The functional information can be assigned to only 40% of them. The function of the rest is unknown and has become a challenging target for research conducted by biologists. Classical genetics used phenotypes, observable physical or biochemical characteristics of an organism, to deduce the functions of genes without any knowledge of molecular biology. Fast and reliable identification of the role of a chosen gene has become possible when a mechanism called RNA interference (RNAi) was discovered [38]. It was stated that when a chemical compound called small interfering RNA (siRNA) is transfected to cells, the gene, that is encoded in that chemical compound, is no longer expressed – its function is suppressed. Therefore, this process, known as "gene knockdown", could be applied for experimental analysis of the function of genes in organisms [51]. As quick as the method was adopted, genes with different functions have been successfully knocked down in various organisms such as plants[100], flies[15] and mammals[62].

HeLa is a cancerous cell line that belongs to the most commonly used human cell lines because it is easy to maintain and transfect. The application of siRNA to the HeLa cells has lead to the discovery of many genes related to cancer[51, 53]. These genes can be further investigated as targets for therapeutic interventions.

The automated production of siRNAs and their application in high-throughput screens can simplify the identification of even larger amount of genes. Libraries containing large amount of siRNAs that knock down different genes significantly speed up the analysis of their functions. Concomitant with the recent advances in genomics, combinatorial chemistry, laboratory automation and information systems such experiments could analyze tens of thousands of samples per day.

The data from such screen is often in the form of images of biological samples acquired by automated microscopes. Gene function is often represented by a phenotype that can be measured in these images. In most cases a phenotype is exhibited by a single cell appearance, behavior or by statistics computed for all cells, such as a number of specific cells. The statistical analysis of these parameters can indirectly deliver information about the gene function. Therefore, the accurate detection and analysis of phenotypes in large numbers of images strongly relies on image processing.

One of parameters that indicate how the mitosis proceeds is the mitotic index. It is defined as the quotient of cells that stay in mitosis (nM) and the total number of cells (nN). Dead cells (nD) are excluded from considerations.

$$MI = \frac{nM}{nN - nD} \tag{3.1}$$

For normal cell cultures the mitotic index does not exceed 5%. Greater values demonstrate a disturbance in the mitosis and may suggest that a "knocked down" gene played an important role in this process. Therefore, the automatic quantification of mitotic and normal cells is necessary to determine genes that impact the mitosis. Dead cells should be also detected and excluded from considerations.

Standard methods perform a calculation of the mitotic index directly from fluorescence images [75, 84]. Fluorescence dyes added to nuclei of normal and mitotic cells make these structures visible. The task is simplified to the detection of fluorescence spots and has been addressed in [41, 109]. The main disadvantage of standard methods is a high toxicity of dyes that immobilize cells and limit

measurements.

The alternative would be to detect cells from phase contrast images. The method is the least toxic method and allows to study changes of the mitotic index over time in living cell cultures.

Three types of cells observed in the phase contrast microscopy exhibit different appearance. Mitotic cells can be distinguished from other cells by a characteristic round shape. As a consequence of a spherical shape of a cell that rounds up during mitosis the light that passes the cell is shifted stronger in phase and, therefore, gives higher contrast. Normal cells are flat and long-shaped. The contrast between the cell membrane and a medium is weak and difficult to detect. As the contrast depends on the amount of the protein in a sample, dead cells are brighter, the structure of the cell membrane and the nucleus is broken, the cytoplasm is more dense and the cell is shapeless.

To test the usefulness of classical image processing methods that use intensity, contrast, or the cell shape, different approaches were evaluated. Edge detectors (Fig.3.1(b)), global and local threshold methods (Fig.3.1(c)) did not perform well due to different intensity profiles of cells and uneven illumination (Fig. 3.1(a)). Binary operators and morphological operators were also tested to detect mitotic cells from negative phase contrast images but due to high number of parameters and limited efficiency the method was not further investigated [71, 67] (Fig.3.1(d)).

Because of a high toxicity of fluorescence dyes and limitation of phase contrast method, it was presumed that the combination of two modalities could provide enough information to calculate the mitotic index. The suggested classifier scheme is presented in Fig.3.2.

A pair of input images (I_{PC} and I_{FL}) are transformed to intermediate forms from which a feature set **x** is calculated. Φ_2 transforms the phase contrast image to a correlation map I_C and Φ_1 detects nuclei from fluorescence images and saves them in the list Q. Features are taken either from the correlation map (x_1, x_3) or from the phase contrast image (x_2, x_4). Superscript Q (x_3^Q, x_4^Q) indicates that features were calculated for each detected nucleus q_i.

Discriminant functions g_1 and g_2 use information from both modalities to generate the list Y of classified cells into three classes (mitotic (ω_m), normal (ω_n) and dead cells (ω_d)). Description of all transformations and features are presented later in this chapter.

In order to justify the choice of the microscopy technique and a cell line different imaging scenarios were evaluated:

1. TDS HeLa cell line imaged with the positive phase contrast microscopy and fluorescence microscopy (nuclei are enhanced by the DAPI stain). See Fig.3.4(a) and Fig. 3.4(b).
2. TDS HeLa cell line imaged with the negative phase contrast microscopy and fluorescence microscopy (cytoplasm is enhanced by the GFP-histone marker). See Fig.3.3(a) and Fig.3.3(b).
3. Kyoto HeLa cell line imaged with the positive phase contrast microscopy. See Fig.3.5(a).

Each cell line was imaged with the CCD camera attached to the Axiovert 200 Microscope with the 20X objective. The imaging took place every 10 minute in 96-well plates.

Active vision One of main concepts of active vision is based on the premise that the observer (human, robot or microscope) may be able to understand a visual environment more effectively and efficiently if the sensor analyzes information selectively. Let us consider the microscope as a manipulator with three degrees of freedom where the stage with a sample is moved in the (x,y) plane and the focus is fixed along the z-axis. In this case, the acquisition camera that records images of the sample plays the role of the manipulator's sensor (effector). In more conventional, passive approach the sensor (CCD camera) is supposed to analyze the whole scene, attempting to make sense of all that it sees. The camera passively scans the sample area in a line-by-line manner and the final image is formed by sequential readings marked with positional information.

In active vision based microscopes, instead of imaging the whole area in the field, only selected region of interests will be stored. Images without objects or with insignificant structures will not be considered. For that purpose the acquisition should be feedback controlled by the image processing software.
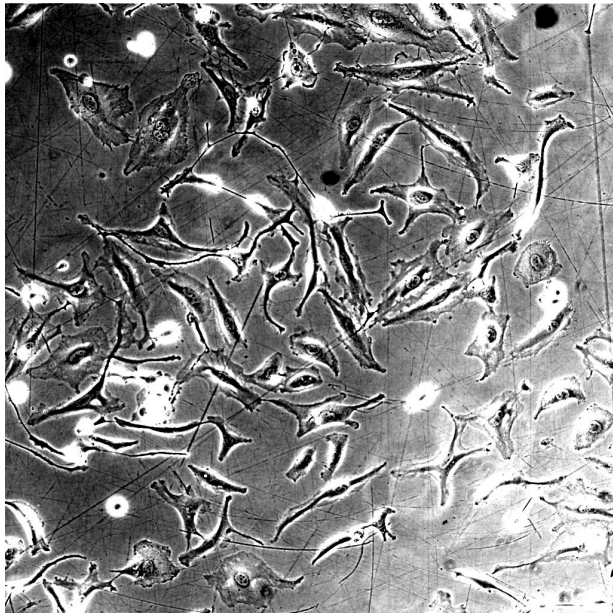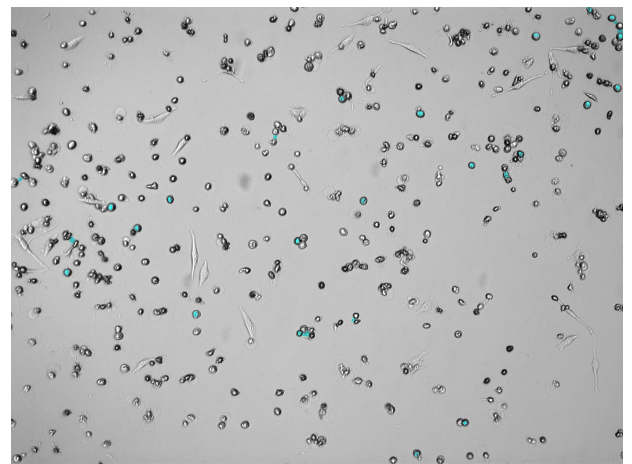
(a) Original phase contrast image

(b) Example of an edge detector (Sobel)

(c) Robust Automatic Threshold Selection [50].

(d) Top-hat transform.

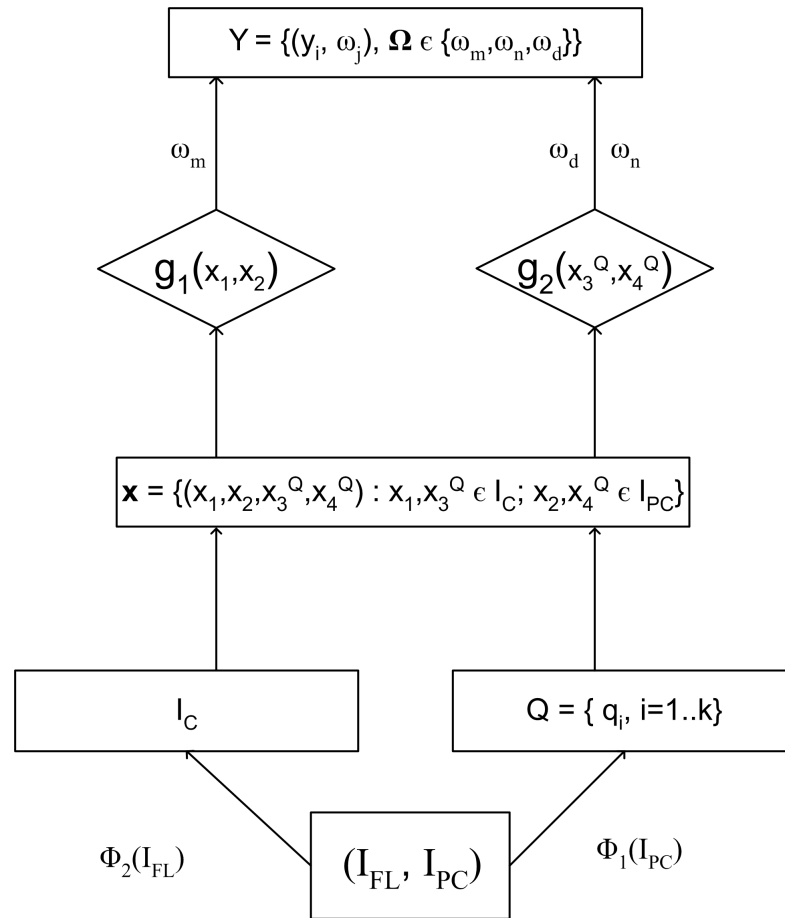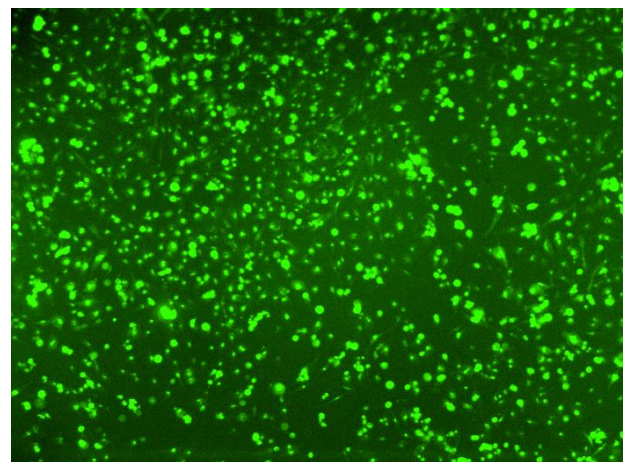Figure 3.1. Phase contrast image analyzed with different image processing methods.

$$Y = \{(y_i, \omega_j), \mathbf{\Omega} \in \{\omega_m, \omega_n, \omega_d\}\}$$

$$\omega_m \qquad\qquad \omega_d \quad \omega_n$$

$$g_1(x_1, x_2) \qquad\qquad g_2(x_3^Q, x_4^Q)$$

$$\mathbf{x} = \{(x_1, x_2, x_3^Q, x_4^Q) : x_1, x_3^Q \in I_C;\ x_2, x_4^Q \in I_{PC}\}$$

$$I_C \qquad\qquad Q = \{q_i, i=1..k\}$$

$$\Phi_2(I_{FL}) \qquad (I_{FL}, I_{PC}) \qquad \Phi_1(I_{PC})$$
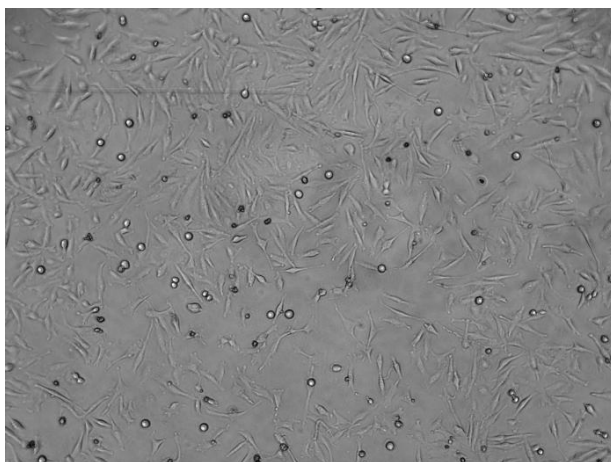
Figure 3.2. Classifier scheme.

Figure 3.3. TDS HeLa cell line imaged by the negative phase contrast and fluorescence microscopy (GFP)
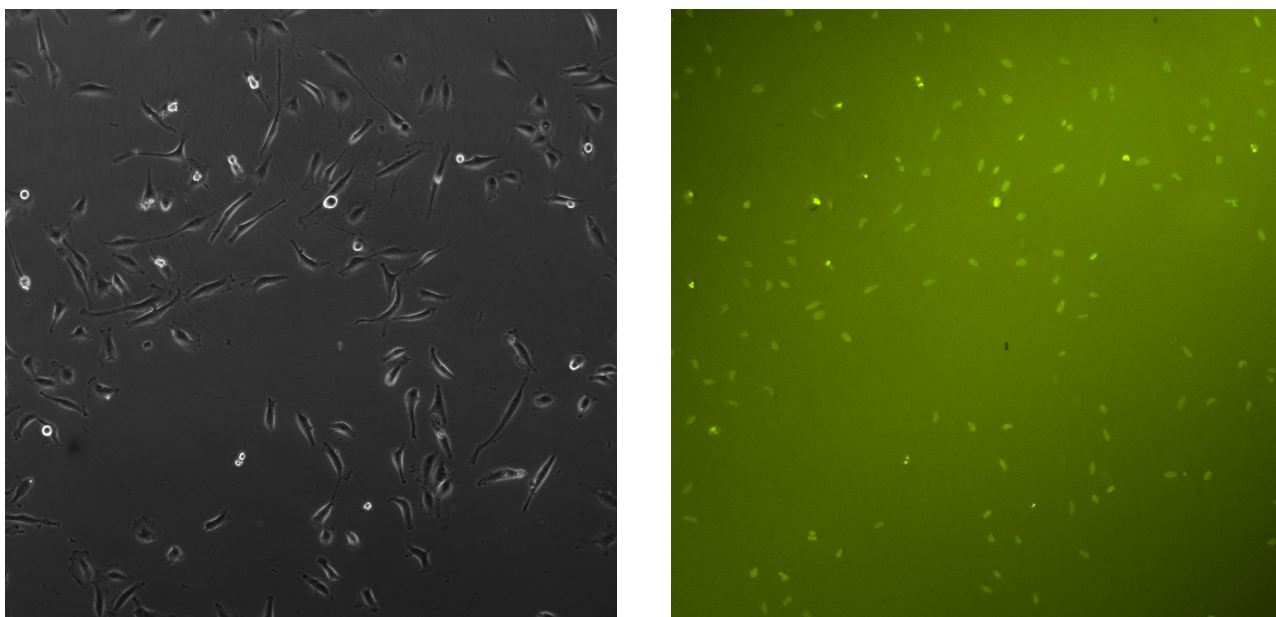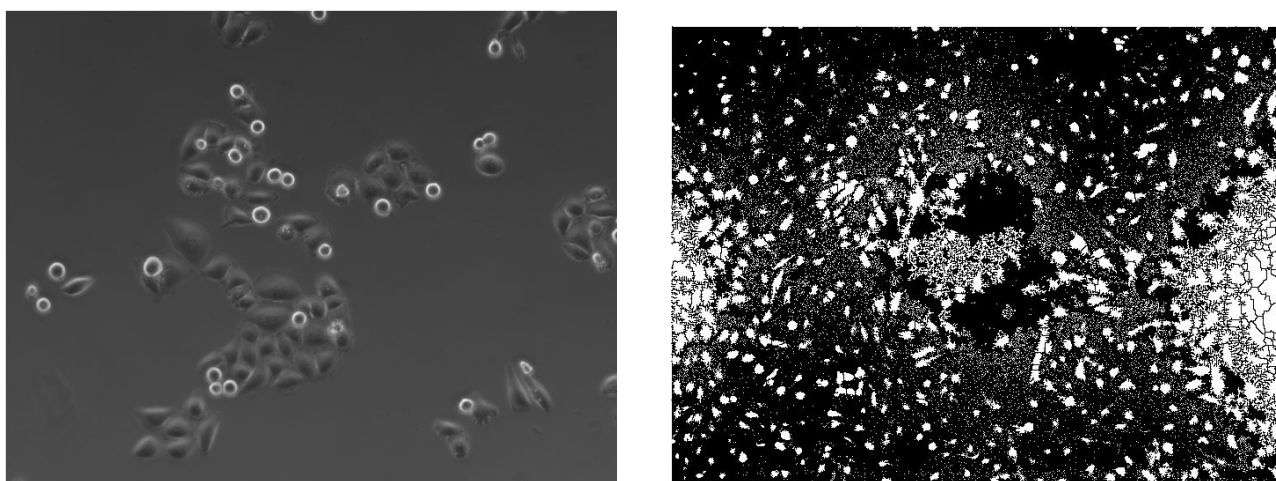
Figure 3.4. TDS HeLa cell line imaged by the positive phase contrast and fluorescence microscopy (DAPI)

(a) Kyoto HeLa cell line, positive phase contrast

(b) Segmented image without preprocessing.

Figure 3.5. Kyoto HeLa cell line imaged in positive phase contrast (a). Watershed segmentation performed on an image without preprocessing steps (b).

Such an approach will unburden the storage capacities by acquiring a relatively small number of images. The possibility of imaging a single cell will deepen the knowledge about its biological processes. Information about the behavior, evolution and the life cycle of a single cell is more useful than statistics computed for the whole cell population.

To our knowledge, there are a few active vision based systems and even fewer in the field of automated microscopy. The ultraprecision six-axis visual servo-control system developed by Kim [48], is a white-light interferometer that is partially controlled by image processing. The system is capable of real-time visual tracking of six-degree-of-freedom rigid body motion with near-nanometer precision. Yang [112] constructed the active visual inspection planning system for active visual inspection of three-dimensional manufacturing computer-aided design (CAD) models that obtains the optimal sensor placement by introducing various sensor constraints, such as resolution, focus, field-of-view, and visibility constraints. High resolution optical systems with controllable intrinsic and extrinsic parameters for microassembly applications is another example that incorporates the active vision approach [101]. The authors presented results of two active vision strategies, depth-from-defocus and visual servoing using an optical microscope. Conrad [16] presentes a system for identification of Subcellular Phenotypes on Human Cell Array. The automated fluorescence microscope is feedback controlled by the image analysis algorithm that selects nuclei for further more specific imaging.

Feedback controlled systems require filtering and segmentation stages to be accurate, fast and dedicated to solve a concrete problem. In that sense, the algorithm presented in the next section that quantifies cells from multimodal images can be reckoned as a first step toward active-vision-based microscopy.

3.1. The analysis of fluorescence images

To decide which of image sets is the best for the calculation of the mitotic index, different algorithms were developed to analyze fluorescence images with cells stained with the GFP-histone marker and the DAPI stain. The analysis flow for both image classes is similar. Firstly, images are pre-processed and a list of cells is generated. Clustered cells are further separated with a watershed technique. Finally, detected cells are classified as normal or dead. Employed methods, already known in the literature, were adopted to a particular fluorescence image class using cell line specificness in order to construct dedicated algorithms.

Pre-processing

Pre-processing step is critical in image processing. Noise, uneven background or poor contrast complicate the segmentation and should be either eliminated from images or significantly reduced.
An example of the watershed segmentation performed on the image that underwent no pre-processing presents Fig. 3.5(b).

In this section, two pre-processing algorithms are presented that extract the information from fluorescence images. Specificness of a fluorescence dye and the microscope used impose the flow and characteristic of applied algorithms. As both of GFP and DAPI image classes had the non-uniform background and the noise, thresholding techniques could not be successful and the shading correction had to be applied.

Images dyed with the GFP-histone marker Non-uniform background, widespread fluorescence signal in the cytoplasm and low signal-to-noise ratio highly obstructs detection of cells (Fig.3.3(b)). To reduce these effects a combination of two Gaussian filters and contrast stretching techniques were applied. A Gaussian filter is defined as a product of two univariate Gaussian distributions centered at $\mu = 0$:

$$G(x,y) = \frac{1}{\sqrt{2\pi\sigma^2}}\exp\left(-\frac{(x-\mu)^2}{2\sigma^2}\right) \cdot \frac{1}{\sqrt{2\pi\sigma^2}}\exp\left(-\frac{(y-\mu)^2}{2\sigma^2}\right) = \frac{1}{2\pi\sigma^2}\exp\left(-\frac{x^2+y^2}{2\sigma^2}\right). \quad (3.2)$$

The width of the Gaussian increases as σ increases.
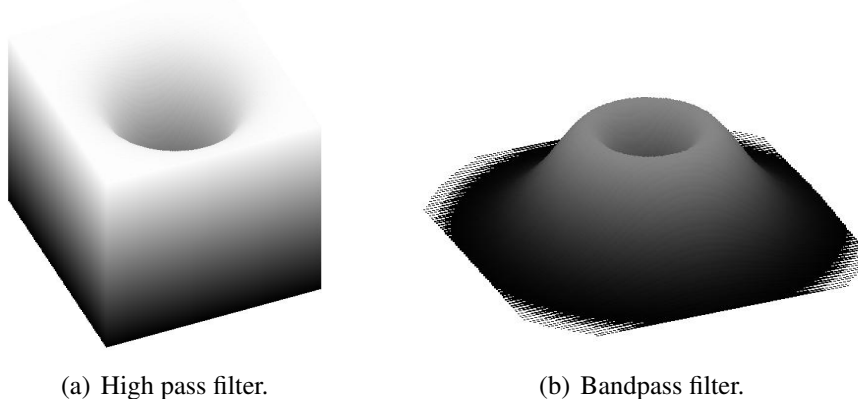

(a) High pass filter. (b) Bandpass filter.

Figure 3.6. Plots of applied filters.

To compensate for the uneven background a high-pass filter was used to remove low frequencies responsible for the global intensity gradient (Fig.3.6(a)). It was realized by subtracting a version of the image, which was smoothed by a filter with σ of the given size. Next, a band-pass filter (Fig.3.6(b))

was applied that discards all but a handful of spatial frequencies that are present in the original image. The band-pass filter was realized as a concatenation of the high and low pass filters. The low-pass filter removed high frequencies that often include random noise. As only the strongest signal sufficed to detect a cell, pixels that belonged to the background and the low signal were also removed. A final step consisted in contrast stretching that selectively enhanced only the strongest signal present in cells. Results of these pre-processing steps are depicted in Fig.3.7(b). Parameters of this step are the size of filters σ. Precautionary means were taken to minimize the undesired effects of wrong set parameters. For example, too large values of the high pass filter accidentally removed cells. If the low pass filter was too small the uneven illumination remained in the image.

Experiments have shown that best results were achieved for the high pass filter of the size $\sigma = 10$ (Fig.3.6(a)). Band-pass filter was realized a sequence of the low and high pass filters with σ equal to 16 and 8, respectively. These values guaranteed the strongest signal to be emphasized.
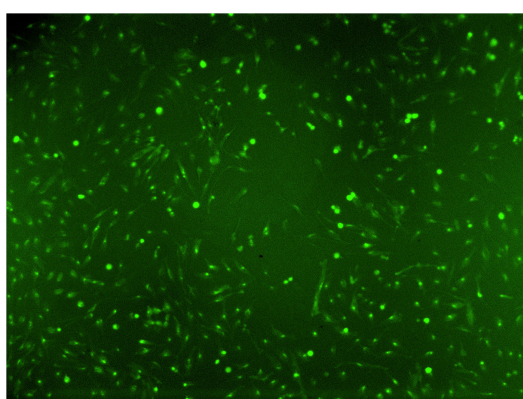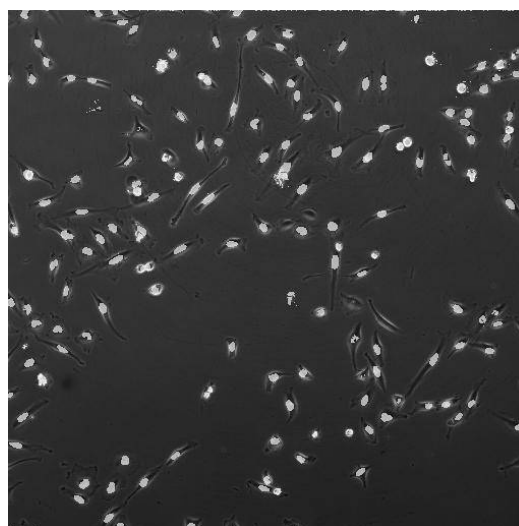

(a) Original image with nuclei in cells are stained with the GFP-histone marker.
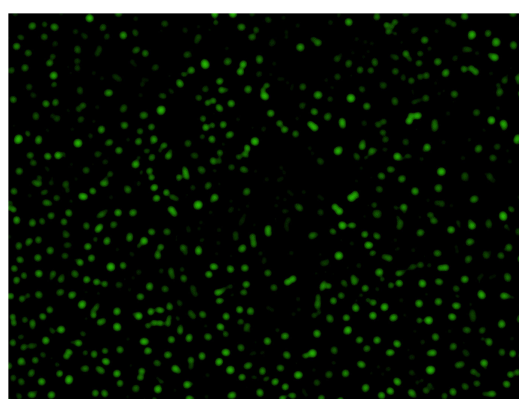
(b) Pre-processed image.
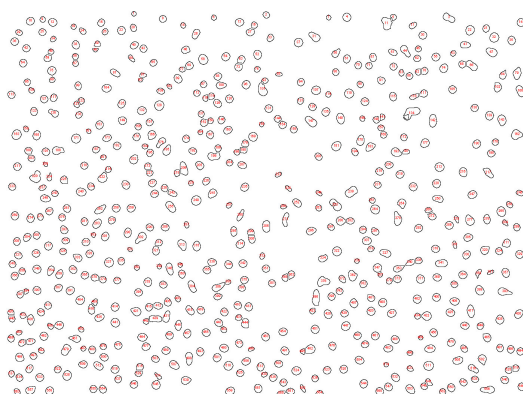
(c) Detected nuclei.

(d) Detected nuclei (DAPI) combined with the phase contrast image.

Figure 3.7. Results of pre-processing methods.

In the next step an adaptive threshold technique [83] was employed and a list of detected nuclei was generated. The adaptive thresholding function divides the image into objects and background in the iterative process. For a test threshold value the average intensity of pixels at or below the threshold (Thr_b) are computed as well as the average intensity above the threshold (Thr_o). Then, it computes the average of those two, increments the threshold (Thr), and repeats the process. Incrementing stops

when the threshold is larger than the composite average $Thr \geq (Thr_o + Thr_b)/2$.

Images with the DAPI stain The DAPI stain induced a different pre-processing technique. As images were acquired with a lower noise level, a rolling ball algorithm [94] sufficed to enhance the DAPI signal present in nuclei and remove the uneven background. The principles of the algorithm follows. The center of the filtering object, a patch from the top of a sphere, is moved along each scan line of the image. Any point with an intensity being either on or below the patch during this process is considered as a part of the background and attains a zero value. In that way, the intensity of pixels belonging to differently illuminated background will be below the patch. Only very light objects, that belong to the fluorescence signal remains unchanged (their intensity is over the patch). The method has got one parameter, a sphere radius. Generally, the sphere (ball) radius should be at least as large as the diameter of the largest object in the image. If it is smaller then more nuclei pixels are considered as the background and the computation lasts longer. For larger values the ability to remove the uneven illumination gets worse.

During experiments the best results where achieved for a sphere radius set to 50 to guarantee the elimination of background pixels only. Filtering took 5 [sec] (PC AMD Athlon 900MHz, 512 MB RAM). The final step consisted in a median filtering that replaces each pixel with the mean intensity value calculated in the 3×3 neighborhood. This step enhanced the quality of the adaptive local threshold that was applied afterward.

Separation of clustered cells. As many clustered nuclei were present in pre-processed images, their separation was necessary.

The watershed segmentation is a method automatically separating or cutting apart objects that touch each other. It was successfully used in many medical applications such as transmission electron microscopy, SEM micrographs, 3D holographic pictures, radiography [7]. In the field of cytology watershed was used to segment clustered cells in the fluorescence microscopy [59] or segmentation of white blood cells in bone marrow images [78].

The intuitive description of the method is quite simple: if the image is considered as a topographic relief where its every point is related to the image gray level, then the watersheds are the lines that separate lakes formed by a hypothetic rain that gradually falls on this relief. A detailed description of the watershed segmentation can be found in [37, 74]. The are numerous implementation of watershed transform [74]. In our application the method introduced in [86] was applied. It calculates the Euclidean distance map (EDM) for an input image. For each point in the EDM that belongs to the cell, its Euclidean distance to the nearest background pixel is determined. The EDM is then used to find ultimate eroded points (UEP), i.e. the peaks or local maxima of the EDM. The UEPs are then dilated either until the edge of the cell is reached, or the edge of the region of another (growing) UEP is met. The watershed transform has important drawbacks that worsen the segmentation. It has been widely treated in the literature [37] and cover following problems: oversegmentation, sensitivity to noise, poor detection for low contrast object boundaries and poor detection of thin structures. Because these problems were rarely encountered in the pre-processed images no additional post-processing steps were applied. The output of the method is presented in Fig. 3.7(c). All detected nuclei are further classified by a discriminant function described in Sec.3.1 and Sec.3.2. Watershed operation took about 3 [sec] (PC AMD Athlon 900MHz, 512 MB RAM).

Evaluation of pre-processing methods In order to decide which pre-processing method performs better, they were applied to both of image classes. Tab. 3.1 presents results of the evaluation. Higher specificity values and lower computational time indicate that the rolling ball method performs better.

Image	Specificity [%]		Computation [sec]	
	Band-pass filtering	Rolling ball	Band-pass filtering	Rolling ball
GFP	65	98	120	4
DAPI	89	99	33	5

Table 3.1. Evaluation of filtering methods performed on the training set (419 (DAPI) and 578 (GFP) measure points).

Moreover, the method has fewer number of parameters than the band-pass filtering. Therefore, the rolling ball algorithm was chosen to detect cells.

Classification of normal and dead cells

The active vision, understood as a selective analysis of image fragments, covered by detected nuclei, allows to classify cells in an efficient way. Various statistics were computed for areas covered by detected nuclei by taking into consideration appearance of cells in different modalities. Because of the dense structure dead cells appear bright on positive phase contrast images and dark on negative phase contrast images (see Figs. 3.3(a), 3.4(a) and 3.5(a)). Their correlation with templates (a method is described in Sec.3.2) is higher than for normal cells. Finally, comparing to normal cells the fluorescence signal of the GFP marker is stronger in destructed DNA fragments of dying cells. Therefore, it was presumed that following features, calculated for regions covered by detected nuclei, could help to discriminate normal and dead cells: mean intensity in phase contrast image (denoted as *meanPC*), mean intensity in fluorescence image (*meanGFP*) and mean intensity in the correlation map (*meanCorr*).

It was important to construct a cheap classifier therefore a 2D feature space was evaluated with easy to implement linear and quadratic discriminant functions. As a reference a k-nearest-neighbors classifier was also evaluated.

In the Bayesian framework (cf. Eq.(2.2)) the MAP classification rule assigns the pattern $\mathbf{x}$ with d features to a class for which a posteriori probability is maximal (or equivalently $\log(p(\omega_i|\mathbf{x}))$ is maximal). It is equivalent to the discriminant rule (Eq.(2.1)) where

$$g_i(\mathbf{x}) = \log p(\omega_i|\mathbf{x}) = \log(p(\mathbf{x}|\omega_i)) + \log(p(\omega_i)) - \log p(\mathbf{x}). \tag{3.3}$$

In the linear and quadratic discriminant analysis the form of the class-conditional probability distribution may be assumed as the multivariate Gaussian:

$$p(\mathbf{x}|\omega_i) = \frac{1}{(2\pi)^{d/2}|Cov_i|^{1/2}} \exp(-\frac{1}{2}(\mathbf{x} - \mu_i)^T \cdot Cov_i^{-1}(\mathbf{x} - \mu_i)). \tag{3.4}$$

When constant terms are eliminated above assumptions transform Eq.(3.3) into

$$g_i(\mathbf{x}) = \log(p(\omega_i)) - \frac{1}{2}\log(|Cov_i|) - \frac{1}{2}(\mathbf{x} - \mu_i)^T Cov_i^{-1}(\mathbf{x} - \mu_i). \tag{3.5}$$

The term $p(\mathbf{x})$ was excluded because it does not depend on a class. In the normal-based quadratic discriminant analysis a pattern $\mathbf{x}$ is classified according to $g_i(\mathbf{x})$ $i = 1\ldots C$ from Eq.(2.5). Further suppose that the classes have a common covariance matrix ($Cov_i = Cov$), in which case the discriminant function is transformed to a linear form

$$g_i(\mathbf{x}) = \log(p(\omega_i)) - \frac{1}{2}\mu_i^T Cov^{-1}\mu_i + \mathbf{x}^T Cov^{-1}\mu_i. \tag{3.6}$$

Features	Classifier		
	Quadratic	Linear	kNN
meanCorr vs. meanGFP	11.5	11.5	8.7
meanCorr vs. meanPC	10.6	10.2	6.7
meanPC vs. meanGFP	10.4	10.7	7.2

Table 3.2. Apparent error rate of classifiers [%]

For convenience the prior probability was estimated by empirical frequencies of the training set:

$$p(\omega_i) = \frac{n_i}{n}$$

where n_i is the number of patterns in ω_i and n is the total number of samples.

Classifiers were constructed according to Eqs. (3.6) and (3.5) from the training set that comprised around 1000 manually classified measure points obtained from 6 randomly chosen images (DAPI stained fluorescence image and positive phase contrast image of HeLa cells). Linear and quadratic discriminant analysis were evaluated by means of the minimum apparent error rate on the training set (Figs.3.8 and 3.9).

Linear classifier not only derived the lowest error rate for features *meanCorr* and *meanPC* but also allowed to use a single threshold value to classify normal and dead cell as indicated in Fig.3.8.

The specificity (cf. Eq.(2.9)) of the method on the test data (6 random images) was equal to 71.38%.
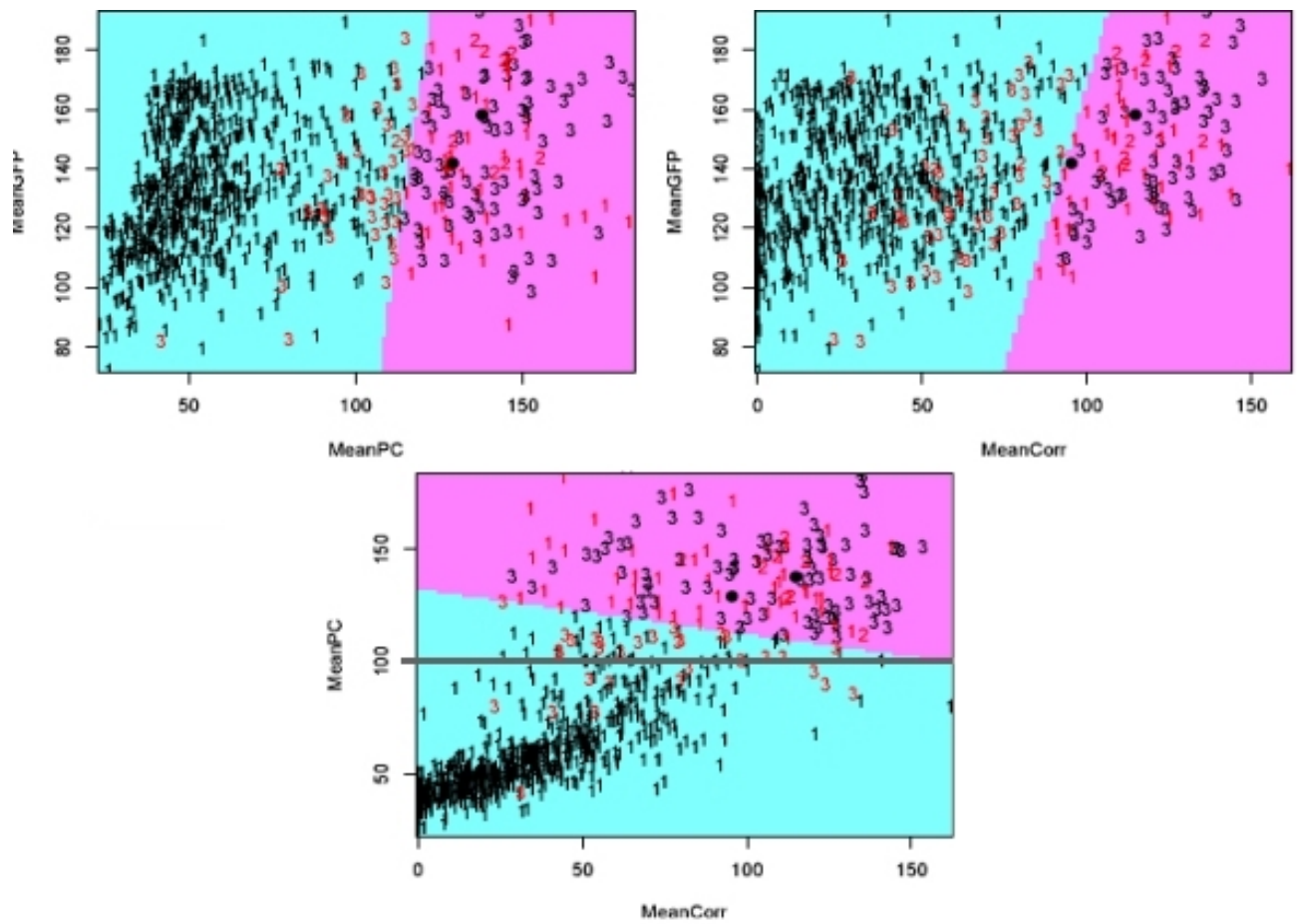
Figure 3.8. Linear discriminant classifier. The apparent error rate is equal 10.7% (top-left), 11.5% (top-right) and 10.2% (bottom). Manually segmented cells are labeled as '1' (normal nuclei) and '3' (dead nuclei).
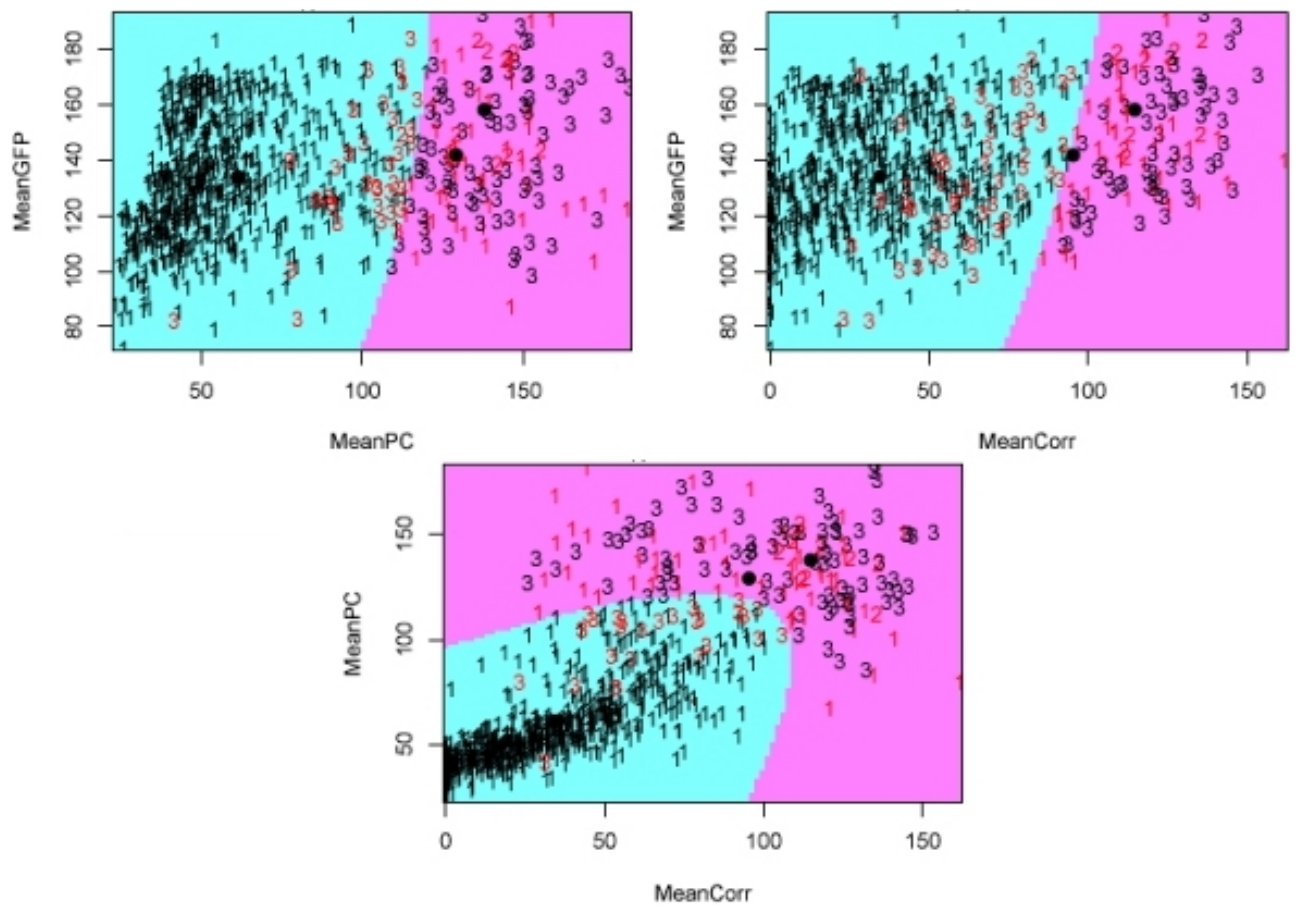
Figure 3.9. Quadratic discriminant classifier. The apparent error rate is equal 10.4% (top-left), 11.5% (top-right) and 10.6% (bottom). Manually segmented cells are labeled as '1' (normal nuclei) and '3' (dead nuclei).

3.2. Correlation based method to detect mitotic cells

Phase contrast microscopy offers the least toxic method to record time lapse movies of life cells. The combination of this technique with the fluorescence microscopy reduces the time cells are exposed on the incident light, which, in turn, also reduces the effect of photobleaching. Therefore, an algorithm was developed that recognizes mitotic cells from phase contrast recordings of two subclones of HeLa cells, Kyoto (Fig.3.5(a)) and TDS (Fig.3.3(a)) that contain cells with different shapes. Both positive and negative phase contrast images were tested to evaluate whether one or the other would be more reliable to identify mitotic cells in growing populations. The *a priori* knowledge about the cell appearance was used to design the correlation-based method followed by the validation algorithm aimed at improving the detection of mitotic cells. The efficiency of the method was demonstrated by analyzing two different image classes.

Detection of objects with image processing methods has already been investigated. Many of them have been employed in the cryo-electron microscopy where automatic particle detection has been studied for a long time. Several approaches with different degrees of success were recently reviewed by Nicholson and Glaeser [76]. Authors compared methods that use template matching based on cross-correlation, edge detection, methods based on intensity comparisons, texture-based methods, and neural networks. They concluded, that none of the methods used alone performs good enough. Thus, it is presumed that combination of different approaches could provide better results. Among alternative methods, template matching proved to be an efficient method of finding candidate particles in various lighting conditions. As images from phase contrast microscopy and from cryo-electron are similar in terms of uneven illumination and the consistent definition of the object's model, the template matching approach was chosen to detect mitotic cells of various cell lines imaged by two different phase contrast microscopy techniques. Moreover, the round shape of mitotic cells allows to construct a small number of rotation invariant templates that depend only on the scale.

Template matching In template matching approach the template image I_T, which is assumed to be similar to the target object, is shifted with respect to the original image I by the vector (x', y'). In the shifted position the scalar product[1] of the two images is computed and placed in the cross-correlation map at the position (x', y'). The vector (x', y') includes all possible positions on the sampling grid [76]. Degree of similarity is indicated by the height of intensity peaks that will be formed at positions corresponding to detected objects. In the spatial domain, this operation is described by the formula

$$\forall_{(x',y')\in[0,N-M]} \quad \gamma(x',y') = \sum_{x,y=1}^{M} I_T(x,y)I(x+x',y+y'), \qquad (3.7)$$

where I is the original image of the size $N \times N$ and I_T is the template image of the size $M \times M$.

There are several disadvantages of using Eq.(3.7): the range of $\gamma(x',y')$ depends on the size of the template, the correlation is not invariant to changes in image intensity such as uneven illumination. The *correlation coefficient* overcomes those drawbacks by normalizing both the image and the template (Eq.(3.7) is replaced by Eq.(3.8))

$$c(x',y') = \frac{\sum_{x,y=1}^{M}(I(x,y)-\bar{I}) \cdot (I_T(x+x',y+y')-\overline{I_T})}{\sqrt{\sum_{x,y=1}^{M}(I(x,y)-\bar{I})^2 \sum_{x,y=1}^{M}(I_T(x+x',y+y')-\overline{I_T})^2}} \qquad (3.8)$$

where $\bar{I}$ stands for the mean of I in the region under the template, and $\overline{I_T}$ is the mean of the template

$$\overline{I_T} = \frac{\sum_{x,y=1}^{M} I_T(x,y)}{M^2}, \quad \bar{I} = \frac{\sum_{x,y=I_T} I(x,y)}{M^2}.$$

---

[1] The scalar product of two images is equivalent to element-wise multiplication of two matrices.

When considering the numerator in Eq.(3.8) with removed mean values $\bar{I}$ and $\bar{I_T}$ the operation requires approximately $N^2(M-N+1)^2$ additions and $N^2(M-N+1)^2$ multiplications [55]. This modification also leads to increase of computational costs. Taking advantage of the correlation theorem, the correlation can be computed faster [55] in the frequency domain:

$$c = F^{-1}(F(I)F^*(I_T)) \tag{3.9}$$

where F indicates the Fourier transform operation, F^{-1} denotes its inverse. The complex conjugate $F^*(I_T)$ is the image in which all values are replaced by their complex conjugates. The complex conjugate of a complex number $a+bi$ is the complex number $a-bi$ (the sign of the imaginary part is changed).

The two dimensional discrete Fourier transform over $(N \times N)$ image I is defined as

$$F(k,l) = \frac{1}{N^2} \sum_{x=0}^{N-1} \sum_{y=0}^{N-1} I(x,y) \exp -i2\pi \left(\frac{kx}{N} + \frac{ly}{N} \right) \tag{3.10}$$

and its inverse as

$$F^{-1}(F(k,l)) = I(x,y) = \frac{1}{N^2} \sum_{k=0}^{N-1} \sum_{l=0}^{N-1} F(k,l) \exp i2\pi \left(\frac{kx}{N} + \frac{ly}{N} \right). \tag{3.11}$$

The effective implementation of the FFT algorithm (the butterfly algorithm) requires the template and the image to be extended to the size equal to a power of two [81]. To ensure the effective multiplication (Eq.(3.9)), the size of the template image was extended ($M = N$) by filling the template image with its mean value. The complexity of the transform is $12N^2 \log_2 N$ real multiplications and $12N^2 \log_2 N$ real additions [55]. The transform is therefore faster than its 'spatial' version [85].

Templates can be obtained either from a computational model or from experimental data. The presented method evaluates both approaches. Other possibilities regarding the generation of templates include averaged templates, projections from 3D models, or two-dimensional Gaussian function of the size close to the target object and are evaluated in [76]. The review also discusses modified cross-correlation-based methods in the form of SPD (synthetic discriminant function) - MINACE (constraint of minimum noise and correlation energy) filter. This filter attempts to obtain sharper peaks while avoiding instability in the presence of noise. Other mentioned improvements consider the phase only matched filter and the symmetric phase only matched filter. Cross-correlation could be also improved by using the shape information of the peak.

In cryo-electron microscopy [77] the cross-correlation function was compared with local correlation coefficients followed by smoothing by the anisotropic diffusion. The results showed that, in this particular problem, correlating with multiple references has little advantage over using single reference. The authors also concluded that smoothing the image before the correlation does not produce dramatic improvements in particle detection.

Dufour and Miller [22] proposed the method to locate an object in the image when its size and rotation are unknown. By using a diffusion-like equation they produce a library of templates which was then used to perform the object detection, described as minimization of the maximum likelihood solution which lead to higher detection rates and required higher computational time.

Important drawback of cross-correlation technique is that it depends on rotation and scaling of the template. This imposes the use of multiple templates with various sizes with different orientations. The choice of the number of templates is usually a difficult task due to trade-off between the quality of results and computational costs. Moreover, due to spatial variations in image intensities and different peak heights, additional post-processing steps, such as a search for correlation peaks, have to be taken.

Validation of candidate peaks The correlation map c attains higher values at positions where the image matches the template. Those intensity peaks indicate possible positions of target objects. Due to the fact that there were still little differences in shape and size between templates and mitotic cells, not only high but sometimes low peaks correspond to target objects. Therefore matched filters allow to achieve reasonably efficiency to detect candidate objects only and further validation of detected peaks is necessary [76]. There are many techniques of searching for peaks. Ludtke et al. [58] as well as Nicholson [77] combined different correlation-maps, each from a different template, by selecting the maximal value at each pixel location from the set of cross-correlation map. Since some particles can have multiple peaks really close to each other the cross-correlation image map is then low-pass filtered [58]. It overcomes the problem of choosing the same particle many times. Slightly different algorithm is presented in [77]. Candidate peaks are detected by a suitable threshold and then pruned on the basis of peaks adjacency. Peaks within user-selected distance (usually slightly larger than the size of the target object) are eliminated in favor of the highest peak. This attempt leads to removal of contaminations and aggregates objects larger than true ones.

Another validation algorithm is proposed in color image segmentation task [107] using mean shift algorithm developed by Fukunaga [29]. One of the features of mean shift vector is that it always points toward the direction of the maximum increase in the density and is very sensitive to local peaks. The authors validated the peaks by calculating the normalized contrast for the valley and two neighboring peaks and excluding the smaller peak if the difference between the valley and the smaller peak is small. Another family of algorithms pruning the candidate objects are performed to the original image, provided the list of candidate peaks is present indicating the positions of candidate target objects. Kivioja et al. [54] propose a ring filter which calculates at every pixel position the average intensity inside the round particle, and intensity in a ring surrounding it. The filter values are formed by the difference between the average intensities inside the circle and those at the ring. The authors proved that the method was successful in detection of spherical virus particles. In the same task Boier Martin et al. [60] described the cross-point which is applied directly on the original image. The image is scanned twice in the same manner. The first scan is done starting from the top of the image, the second from the bottom. The output binary image is created according to the difference in intensities of pixels pairs located at a fixed distance in the horizontal and vertical direction. If in both cases the difference between pixels is larger than a given threshold, the output pixel at this position is marked as hit. The final image is an average sum of the two binary images.
Both of the methods are suitable mainly for the cryo-electron microscopy as they depend strongly on properties of the original image and particles themselves.

We have focused on the detection of mitotic cells. One of the simplest features of many mitotic cells is that they round up during mitosis. It was also observed that the inside of mitotic cells, in both phase contrast techniques, have rather homogeneous intensity which changes dramatically at the cell periphery. These observations lead to the choice of four features that may help to identify mitotic cells: area, eccentricity[2], intensity level of the cell membrane and intensity of the cell inside. Their distributions are presented in Fig.3.11 (calculated from the training data). This *a priori* knowledge was used to design the detection method based on the template matching technique.

Description of the method From 360 images per movie available, four series of 31 8-bit images of the size 1392×1040 (TDS HeLa cell line) or 736×570 (Kyoto HeLa cell line) were selected randomly. The aim of the detection algorithm is to process a high number of movies. Thus, we have performed the cross-correlation in the Fourier space (Eq. (3.9)) and limited number of templates [69]. The templates were designed either artificially or from test data (Fig.3.10(b)). In the latter case, the

---

[2] The eccentricity of a shape is a measure that describes its circularity. For the ellipse with the same second moments as the shape, the eccentricity is the ratio of the distance between the foci of the ellipse and its major axis length.

(a) The surf plot of the mitotic cell.

(b) Templates used for cross-correlation. Left panel: artificial templates, right panel: templates from test data, top row: Kyoto cell line, bottom row: TDS cell line
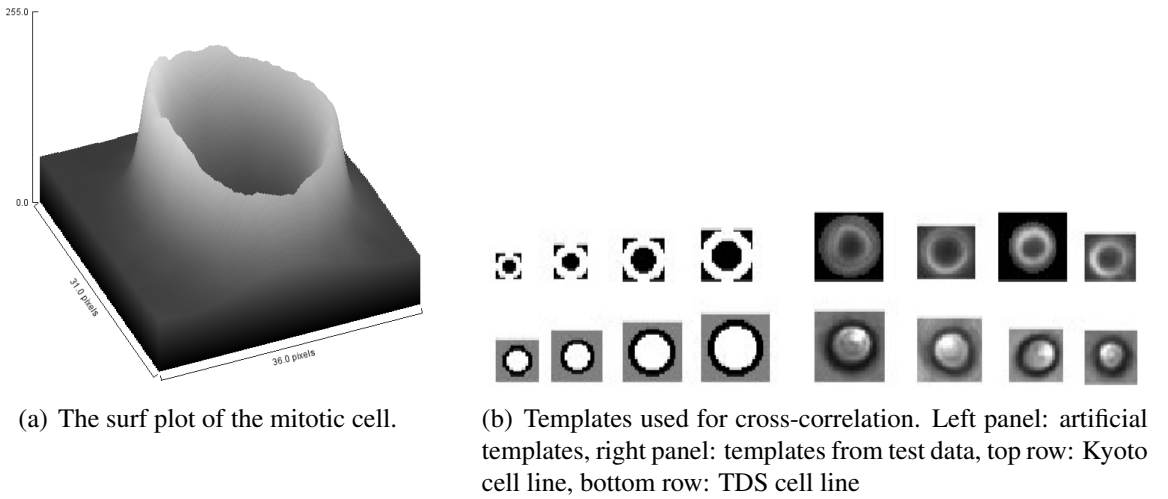
Figure 3.10. Original and artificial templates.

templates were formed by cropping mitotic cells from test images. The model of Kyoto mitotic cells was a black circle with white boundary. Similarly, the model of TDS mitotic cells was a white circle with black boundary. Due to higher brightness of images, the background was gray (intensity 128). The experimental estimated radii of target cells varied from 20 to 32 pixels and the cell membrane was about 2 pixels thick (cf. Fig.3.11). In both cases, radii of templates were chosen to cover the whole range by equi-length partition ($r = \{20, 24, 28, 32\}$). As templates were of circular shape they did not depend on rotation.

The method flow In the pre-processing step images were smoothened by the (3×3) median filter [86] to suppress local fluctuations in pixel intensities. The detection algorithm is described by the following steps:

Step 1: Correlate the given image I with each of the templates I_k, $k = 1, \ldots, n_t$ according to Eq. (3.9). As the result correlation maps c_k are generated.

Step 2: Determine the maximum correlation value at each pixel position (x,y):

$$\forall_{(x,y)} \in I, \quad I_{max}(x,y) = \max_{k=1}^{n_t} c_k(x,y). \tag{3.12}$$

Step 3: Peaks detection and validation (Peak searches)

The highest peaks are detected by using a suitable threshold ρ determined by visual inspection of cross-correlation results. A candidate object is centered in image I at the position (x,y) iff $I_{max}(x,y) \geq \rho$.

Because the peaks in I_{max} have different heights this operation generates many false positives. Therefore, there is a need to validate candidate objects. Presuming that peaks coordinates indicate positions of candidate target objects, the validation is performed on the original image I to exclude false positives from the object list. Two validation methods were compared. The first one is a modification of the cross-point method developed by Boyer [60], called the *modified local gradient*. The second one is our contribution and is based on the evolutionary approach.

The modified local gradient method Using the mean intensity of the image (which, as observed, is close to the intensity of the cell-inside) the gradient is calculated along four directions (up, down, left, right) originated at the object center. If a prescribed gradient is detected in all the directions at a certain distance from the center, the object is classified as a mitotic cell. Otherwise, the object is removed
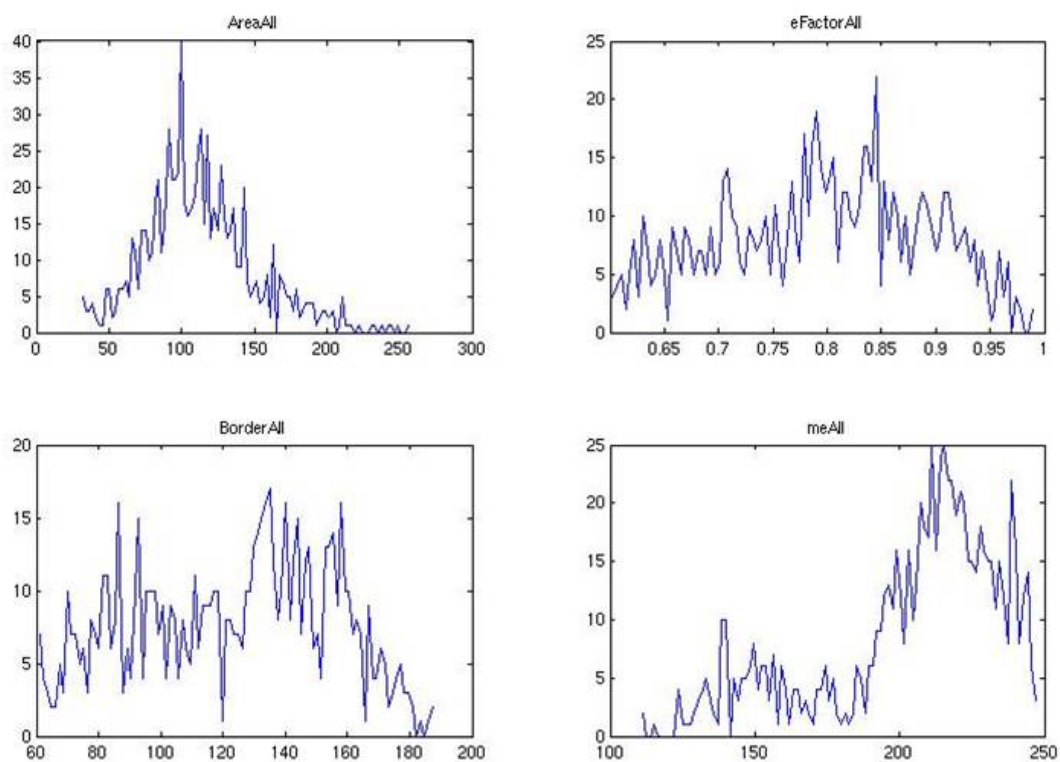
Figure 3.11. Distribution of features used in detection of mitotic cells (values of a given feature vs. their frequency). Following features were measured: area (top-left), eccentricity (top-right), intensity level of the cell membrane (bottom-left) and intensity of the cell inside (bottom-right).

from the list of target objects. An object is also neglected if the gradient found is to close to the center of the cell or if peaks are to close to each other (closer than the radius of the cell). The parameters of this step are the following: the difference in gradients between the inside of a cell and its boundary, the range where the gradient is to be observed. They have to be estimated during the learning procedure.

The resulting list of objects is assumed to be the list of detected mitotic cells. The output image is depicted in Fig.3.12.

(a) HeLa Kyoto cell line, positive phase contrast   (b) HeLa TDS cell line, negative phase contrast
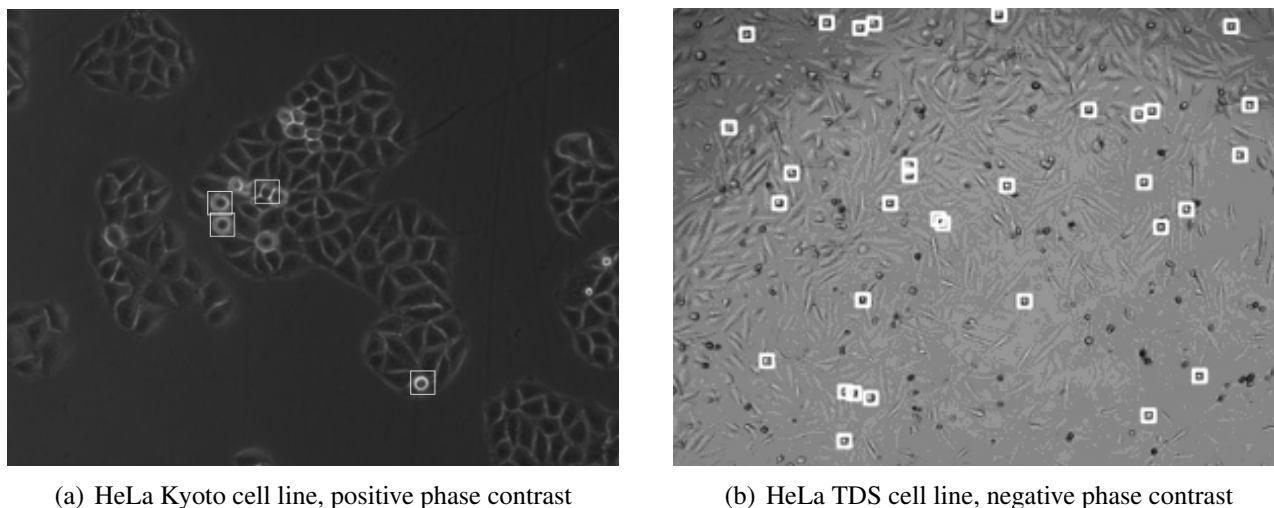
Figure 3.12. Sample images with marked detected mitotic cells for Kyoto and TDS cell lines (imaged by two phase contrast techniques).

The detection method was evaluated for many images taken in various conditions. The comparison of original and artificial templates was also performed. The results are presented in Fig. 3.13 by means of sensitivity and specificity for both imaging techniques (also known as TPF and FPF (here $FPF = 1 - FP/(FP+TN)$), see Eqs.(2.9) and (2.8)). These results were obtained using real images segmented by an expert. The Fig. 3.13 shows that, in average, the specificity is equal to 90.8% for positive phase contrast (TDS cell line)
indexcell line!TDS HeLa and 82.3% for negative phase contrast (Kyoto cell line).
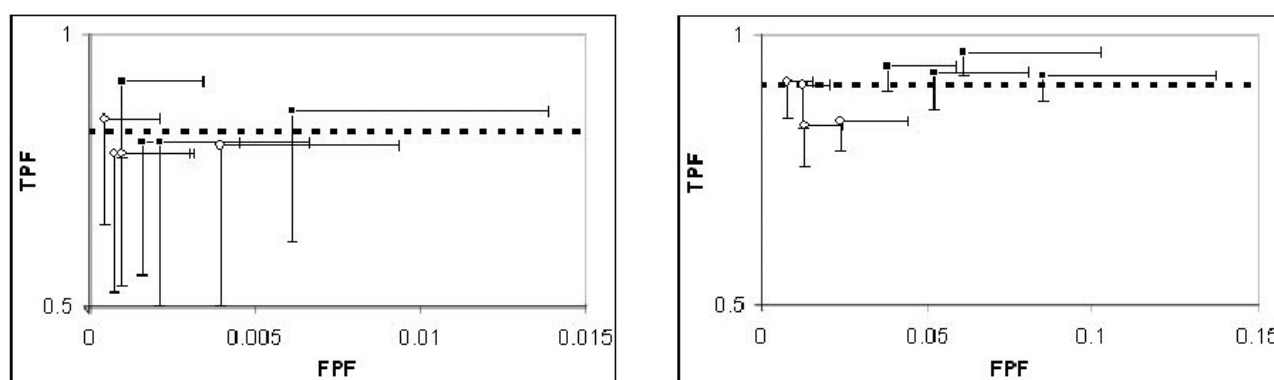

Figure 3.13. TPF vs. FPF measured for negative (left) and positive phase contrast (right). Each element (quadrants for artificial templates, circles for real templates) represent mean value and standard deviation for one film. Dotted line represents the mean value of all results.

The algorithm was implemented in Java using Image Processing Library provided by ImageJ [82]. The whole process of detection for one image and one set of four templates took couple of seconds,

when performed on Power Mac G5 with two 2 GHz processors and 2 GB RAM and up to 22 seconds when performed on PC with Intel Pentium 4 3.06 GHz processor and 2GB RAM.

Evolutionary approach to validation Evolutionary algorithms are stochastic optimization methods that mimic processes derived from natural biological evolution [2, 64, 72]. Candidate solutions of the optimization problem are individuals in a population that evolves iteratively. Processes borrowed from the biological evolution such as reproduction, mutation, recombination, natural selection or survival of the fittest are used to promote individuals that are close to the optimal solution. The use of a population of solutions helps the evolutionary algorithm to avoid being trapped at a local optimum, in cases when a better optimum may be found in its vicinity.

The applied method was based on the evolutionary algorithm with soft selection[31]. Unlike a standard approach when the fittest individuals are selected, the soft selection promotes more frequently these individuals which are better suited to their environment. The mutation step ensured the exploration of the search space. During the optimization process the algorithm changes the parameters of the artificial circle in order to achieve higher fitness function values, and, in turn, to match mitotic cells.

The radius of the cell and position of its center defined the R^3 search space. 8 individuals were initiated with the same coordinates of a candidate (x, y) and 4 different radii values (each radius was given to 2 individuals). The individuals formed the initial population $X = \{x_i, \quad i = 1 \ldots n_e\}$ with $x^i = (x_i, y_i, r_i)^T$. Each center was set at a tested candidate peak and radii were equal to radii of the templates. Mutation was Gaussian shaped with the standard deviation σ

$$Y = X + \xi_{N(\mu,\sigma)}$$

where Y denotes the next generation and ξ is a random variable with values taken from a normal distribution defined as

$$N(\mu, \sigma; x) = \frac{1}{\sigma\sqrt{2\pi}} \exp\left(-\frac{(x-\mu)^2}{2\sigma^2}\right).$$

Non-negative fitness function $\phi(\cdot)$ was calculated for each individual on the phase contrast image I. It was equal to the average of $I(x, y)$ values at positions defined by a circle $(x - s_x)^2 + (y - s_y)^2 = r^2$ (for negative phase contrast images the inverse of the average was taken). s_x and s_y correspond to the center of a candidate peak.

After $t = t_{max}$ generations the fitness of best individual indicated a final individual (solution).
Step 1: initialization $X^t = \{x_1^t \ldots, x_{n_e}^t\} : x_i^t = (s_x, s_y, r)^T$, r varies, time $t = 0$
Step 2: initial evaluation of X^t :

$$\phi(X^t) = \{q_1^t, \ldots, q_{n_e}^t\}, \quad q_i^t = \phi(x_i^t) \tag{3.13}$$

and selection of the current best item $q^* = max_i(q_i^t)$
Step 3: iteration ($t < t_{max}$)

1. evaluation of X^t (Eq.(3.13))
2. the choice of the best item among q_i^t

$$q^* = max_i(q^*, q_i^t)$$

3. soft selection

$$P(x_i^t) = \frac{\phi(x_i^t)}{\sum_{j=1}^{n_e} \phi(x_j^t)}$$

4. mutation

$$y_i^t = x_i^t + N(0, \sigma)$$

5. new population
    $X^{t+1} = Y^t$

6. next step of the iteration
    $t \leftarrow t + 1$

Parameters of the method are σ and the number of individuals n_e. $P(x_i)$ denotes a probability of choosing the *i*th individual. As small populations have the ability to escape local optima and cross fitness valleys to reach higher-fitness regions of a fitness landscape (this phenomenon is often termed as a "saddle crossing" ability) [26, 32, 33] 8 individuals were used. For $\sigma = 0.3$ possible variations of the position are up to the unit change on the image grid (with 99.99% confidence). Experiments indicated that after 150 iterations, the position of the best individual matched the center of the mitotic cell, therefore, the t_{max} parameter was set to 200 iterations which sufficed to find the local optimum. No training is required to set the parameters. Validation of one phase contrast image took about 6 [sec] (PC AMD Athlon 900MHz, 512 MB RAM) and the specificity of the method was equal to 77.71 % and 86.00 % (two independent tests) for negative phase contrast images and 81.11 % for positive phase contrast images. More detailed description of the method can be found in [68].

Biological evaluation To evaluate the method in practice, a biological experiment was constructed. The aim of the experiment was to calculate the mitotic index from phase contrast and fluorescence images with algorithms presented in previous sections. The evaluation of the detection method performed on different data sets as well as the comparison of validation methods justified the experimental setup. As better results were achieved for negative PC images, TDS HeLa cells stained with the GFP were examined.

Despite a slightly worse specificity, the evolutionary validation was chosen. The method required less number of parameters which could be set without the training procedure. The mitotic index was calculated by dividing a number of mitotic cells (present in PC images) by a number of normal cells (present in fluorescence images). Dead cells were also detected with a method described in Sec.3.1 and excluded from consideration. HeLa cells were transfected with esiRNA against CDC16 (expression of the gene CDC16 was supressed) which is known to give an increase in mitotic index. The comparison with negative control (unmodified cells), that is known to give 3-5% mitotic index, is presented in Fig.3.2.

The increase in the mitotic index both for a control and CDC16 are consistent with the theory (the increase were also present in experiments presented in [75]) and show that the analysis of multimodal images leads to satisfactory results. Although the specificity of different algorithms' stages is around 80%, due to large number of cells and images, it is acceptable in practice. In comparison to fixed cells analysis where the mitotic cells are calculated for only one timepoint, the method allows to analyse the mitotic index evaluation over time in living cell populations. Further analysis of properties of the mitotic index curves may result in detection of additional phenotypes.

Discussion

A simple and fast method aiming at calculation of the mitotic index from two modalities was presented. Two cell lines and different microscopy techniques were examined. Therefore, it is pre-
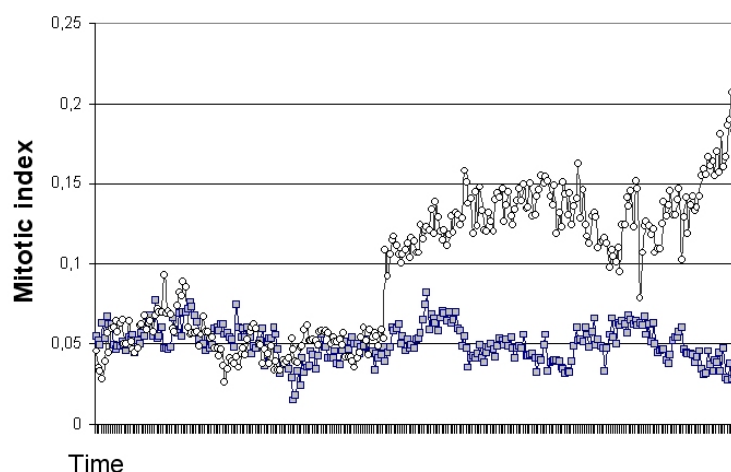
Figure 3.14. The mitotic index for control (quadrants) and CDC16 (circles) cells.

sumed that the method can be also used for other types of cell lines as long as target objects have distinguishable morphology.

In the case of mitotic cells, their round, regular shape and characteristic intensity pattern allowed to limit the number of templates to only a few. We observed that four templates with an evenly spread radii range were sufficient for the reliable detection. It is also noticeable that artificial templates perform quite well comparing with templates derived from test data. It allows to use them for a preliminary detection despite different lighting conditions. The tests also revealed importance of the validation algorithm which significantly decreases the high number of false positives obtained after first three steps of the algorithm (correlation and thresholding). Two validation algorithms were also presented. Due to limitations of the modified local gradient method, an alternative, the evolutionary algorithm was constructed. Future enhancements may consist in the use of a local threshold (for example calculated around each peak) instead of a global one.

It is also possible to set parameters such as threshold automatically, according to some a priori knowledge about the microscopy technique or features of the object itself. The only parameters to be set would be the size of a target object (minimal and maximal cell radius).

Designing a system that automatically selects cells is a very difficult task due to problems with modeling visual processes in recognition of faulty cells [54]. The proposed method may be considered as an example of automated system that solves a specific task, determination of the mitotic index in multimodal images. The method has proved its reliability in biological experiments [52]. Moreover, the use of multimodality reduces the toxicity of cells and, as such, could be applied to living cells.

4. Cervical Cancer Diagnosis Support

4.1. Introduction

Phase contrast microscopy [4, 8, 115] holds considerable promise in cervical cancer diagnosis, second most frequent type of cancer worldwide (Fig.4.1).

Evaluation of samples directly after the examination and large diagnosis spectrum makes this method a recommendable alternative to Papanicolau (Pap) smear test. Although successful in reducing cervical cancer mortality, Pap tests have many drawbacks including high false positives and false negatives ratio, limited identification of premalignant and malignant disease of cervix.

On the contrary, study of the smear with phase contrast microscopy allows simultaneous cytohormonal evaluation, indication of components in vaginal eco-system, determination of menstruation cycles and oncological diagnosis [28, 36, 43, 65, 66, 95]. Moreover, observed cell samples have to be neither stained nor dyed which yields, on one hand, more reliable and accurate diagnosis, on the other hand, fast degradation of the sample, which dries up after 3-4 hours. The use of digital methods of recording microscopic images provides a solution to this problem. Because the evaluation of hundreds or thousand of images is a tedious task an automated image analysis seems to be indispensable.

In this chapter, a method is presented that simplifies evaluation of images obtained from the phase contrast microscope. It is aimed to automatically analyze images, generated during an examination, and present the physician only regions of interests that contain objects essential for oncological screening, namely epithelial cells. Non epithelial elements such as granulocytes, semen, lymphocytes, erythrocytes, vaginal microflora (bacterias or viruses) and artifacts that result from false sample preparation (dust particles, pieces of glass or air) obscure the diagnosis and as irrelevant should be removed from images.

4.2. Evaluation of segmentation methods

The epithelial cells are located in three layers in the cervix tissue. Basal and parabasal cells in the lowest layer transform into intermediate and superficial cells in upper layers. The transition between these forms is continuous, which makes the cell type detection based on their size or shape difficult. Moreover, due to various lighting conditions and similar intensity profile of many objects, such as nuclei or granulocytes, the intensity also does not provide reliable discrimination properties (see Fig.4.3).

Different edge detectors (Roberts, Sobel, Prewitt, Laplace of Gaussian and Canny) were evaluated [12, 93, 86]. Although the most reliable detection of the cell contour is provided by the Canny operator, the edge detector alone is not sufficient for detection of cells (Fig.4.4(b)).

Segmentation with Markov Random Fields.

As MRF proved to be efficient in segmentation of medical images [73, 92, 102] a simple MRF was also evaluated.

From Eq.(2.11) the segmentation of the image is equivalent to the labeling f which maximizes $P(f|I)$. According to the Bayes' rule, $P(f|I) = P(I|f) \cdot P(f)/P(I)$. As $P(I)$ does not depend on the
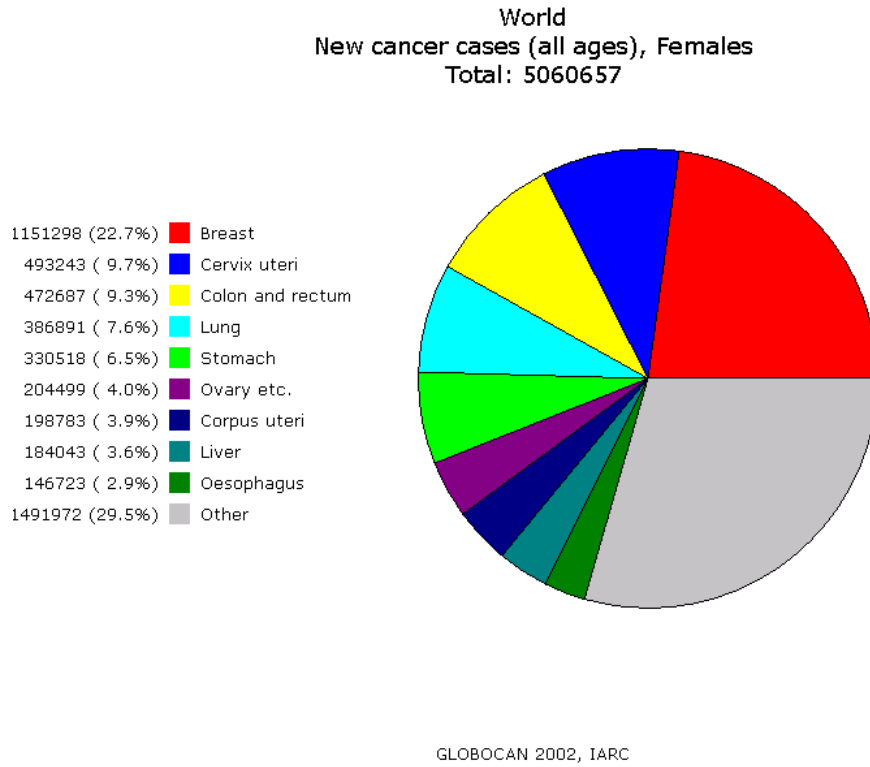
World
New cancer cases (all ages), Females
Total: 5060657

1151298 (22.7%)	Breast
493243 (9.7%)	Cervix uteri
472687 (9.3%)	Colon and rectum
386891 (7.6%)	Lung
330518 (6.5%)	Stomach
204499 (4.0%)	Ovary etc.
198783 (3.9%)	Corpus uteri
184043 (3.6%)	Liver
146723 (2.9%)	Oesophagus
1491972 (29.5%)	Other

GLOBOCAN 2002, IARC

Figure 4.1. New cancer cases worldwide (2002)

labeling f, and plays the same role as the normalization factor Z in Eq.(2.11), it can be omitted. By assuming that

$$P(I|f) = \prod_{i=1}^{N_L} P(I_i|f_i) \tag{4.1}$$

a posteriori probability is proportional to:

$$P(f|I) \propto P(f) \prod_{i=1}^{N_L} P(I_i|f_i). \tag{4.2}$$

Further, the image segmentation model is defined as follows. Let's assume the Gaussian form of $P(I_i|f_i)$

$$P(I_i|f_i) = \frac{1}{2\pi\sigma_{f_i}^2} \exp\left(-\frac{I_i - \mu_{f_i}}{2\sigma_{f_i}^2}\right) \tag{4.3}$$

where μ_{f_i} (f_i takes values from L, $\#L = N_L$ is a number of labels) and σ_{f_i} denote statistics computed for a image region labeled with f_i (the mean and the standard deviation). This expression multiplied by the $1/T$ corresponds to the energy potential of cliques of the first order (cf. (4.5)). The multi-logistic MRF model of $P(f)$ is assumed and given by

$$P(f) = \exp(-\frac{U(f)}{T}) = \exp(-\frac{1}{T}\sum_{c \in C} V_c(f)) = \exp(-\frac{1}{T}\sum_{\{i,j \in C\}} \beta \cdot \gamma(f_i, f_j)) \tag{4.4}$$
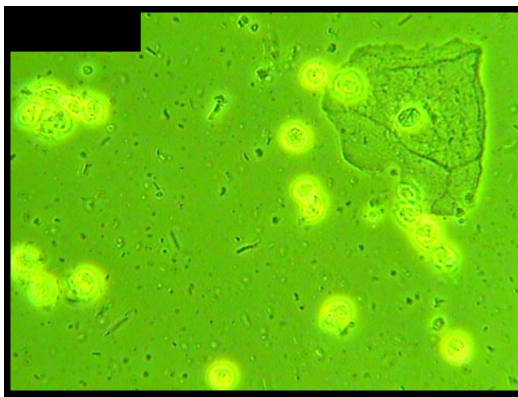
with cliques $c \in C$ of the first and the second order. In the first case (Eq.(4.3)) c consist of a single site, in the second (Eq.(4.4)), of a pair of neighboring sites. The energies of cliques of first order directly
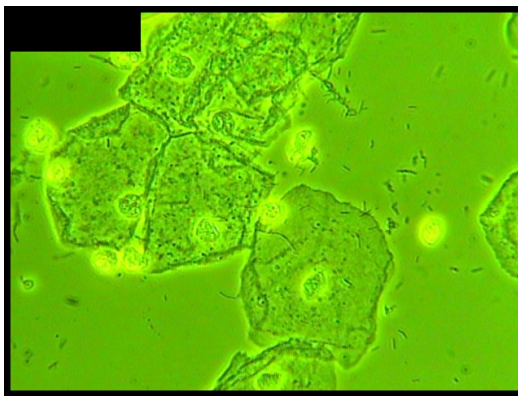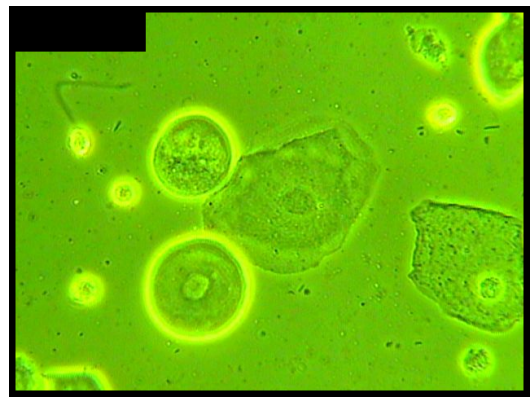
(a) Overlapped cells with some granulocytes.
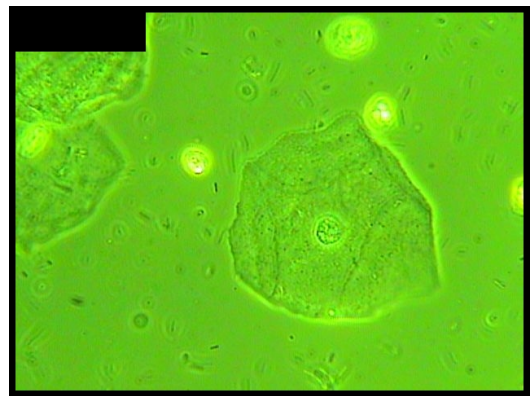
(b) A cell with not fully distinguishable membrane.

(c) A cell with numerous granulocytes (bright oval objects) and bacteria.

(d) Basal cells (big, round objects in the center) with semen.

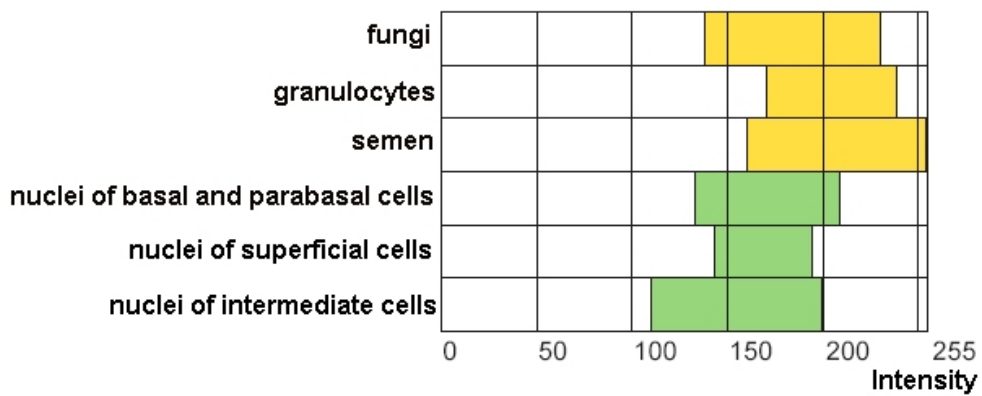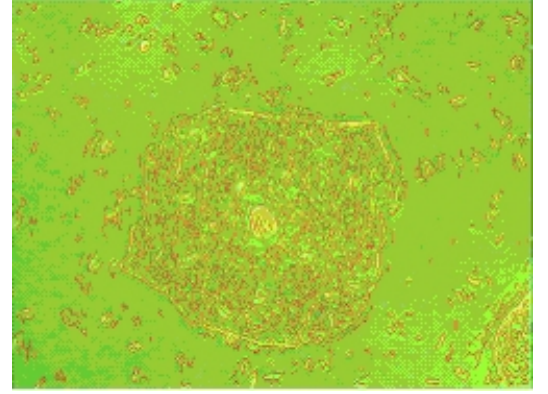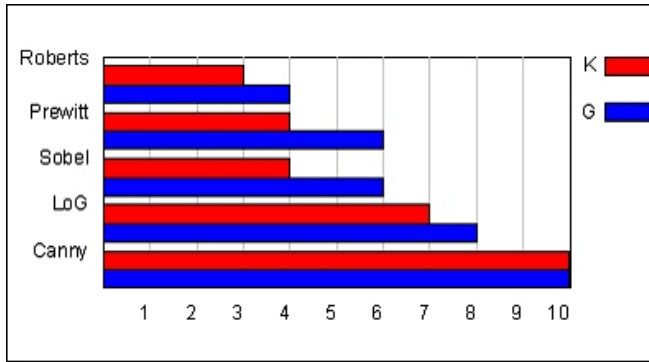Figure 4.2. Phase contrast images of epithelial cells.

Figure 4.3. Intensity of typical elements in phase contrast image. Data were collected from manually segmented elements.

(a) Comparison of different edge detectors. The measure *K* corresponds to the number of correctly detected contour pixels, the measure *G* is the ratio of grouped and manually segmented contours. The results were obtained from 30 manually segmented images and further normalized (the best value for both measures is 10).

(b) Canny detector.

Figure 4.4. Evaluation of simple edge detectors.

reflect the probabilistic modeling of labels without context, which is used for classifying or labeling the pixels independently. β is the model parameter controlling the homogeneity of regions. Owing to its simplicity, $\gamma(f_i, f_j)$ is defined as

$$\gamma(f_i, f_j) = \begin{cases} -1 & \text{if } f_i = f_j \\ +1 & \text{otherwise.} \end{cases}$$

Such a model has been widely used for modeling regions and textures [57] and tend to generate texture-like patterns. The estimation of f, denoted as $\hat{f}$ is computed as follows

$$\hat{f} = \arg\max_{f \in \mathbb{F}} \left(\frac{1}{T} \ln P(I|f) + \ln P(f) \right) = \tag{4.5}$$

$$= \arg\max_{f \in \mathbb{F}} \left(\sum_{i=1}^{N_L} -\frac{1}{T} \left(\ln \sqrt{2\pi\sigma_{f_i}} + \frac{(I_i - \mu_{f_i})^2}{2\sigma_{f_i}^2} \right) - \frac{1}{T} \sum_{\{i,j \in C\}} \beta \cdot \gamma(f_i, f_j) \right) =$$

$$= \arg\min_{f \in \mathbb{F}} \left(\sum_{i=1}^{N_L} \frac{1}{T} \left(\ln \sqrt{2\pi\sigma_{f_i}} + \frac{(I_i - \mu_{f_i})^2}{2\sigma_{f_i}^2} \right) + \frac{1}{T} \sum_{\{i,j \in C\}} \beta \cdot \gamma(f_i, f_j) \right). \tag{4.6}$$

The estimate of f was done through energy minimization with two iterative optimization methods: ICM [6] and Gibbs sampler [34]. The first method uses the "greedy" strategy in the iterative local minimization and its convergence is guaranteed after only a few iterations. Gibbs sampling is an algorithm to generate a sequence of samples from the distribution of each variable in turn, conditional on the current values of the other variables.

The image was segmented into three classes that correspond to background, cell and the cell membrane in the open source software [5, 45, 47]. Initially $T = 4$ and $\beta = 0.9$. The performance was evaluated in two respects of each algorithm: the reached global minimum of the energy function (computed from Eq.(4.5)) and computational time. In both cases the execution was stopped when the energy change ΔU was less than 0.1% of the current value of U. In the initial step, a random configuration f was chosen. Tab. 4.1 presents comparison study. Segmentation results depicted in Fig.4.5 [1] show that

---

[1] Here and later on black rectangles in the left-upper corner were shaded because they contained personal data of patients.

	Iterations	CPU time [sec]	Global energy
Gibbs sampler	202	99	1733620
ICM	17	10	1782860

Table 4.1. Comparison of minimization algorithms.
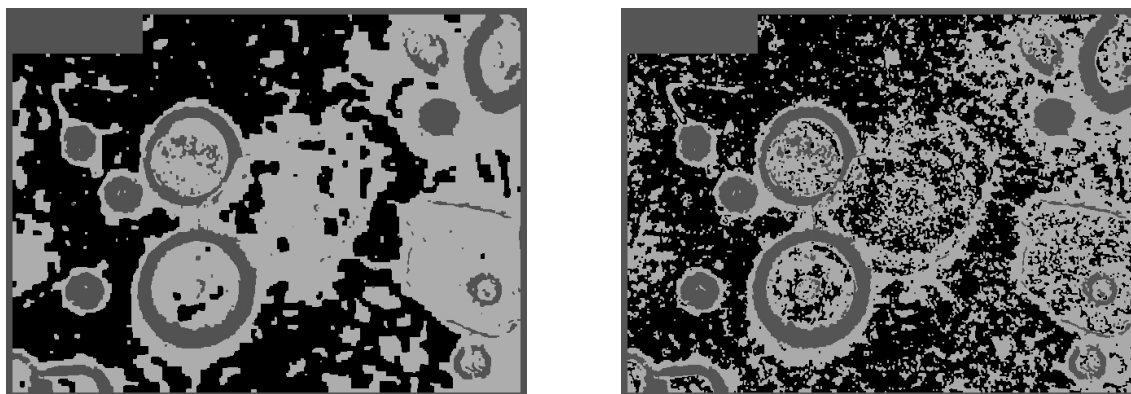
(a) Gibbs sampler.   (b) ICM

Figure 4.5. Segmentation with Markov Random Fields.

optimal configuration (labeling) was not satisfactory. Many pixels were assigned to wrong classes. Moreover, minimization of energy was computationally expensive and practically not applicable in real applications.

4.3. Segmentation with Statistical Geometrical Features

Observation that the phase contrast microscopy distinguishes these parts of cells that contain a higher level of proteins has lead to an approach which uses texture features [89]. As cell structures such as cell membranes, cytoplasm or nuclei contain different protein level, they also display different texture patterns than the medium. Therefore, a texture seems to be an important factor to distinguish cells from other regions.

Texture features were successively used in many applications. Santos [87] used texture features derived from the histogram and a gray level co-occurence matrix to perform segmentation of epithelial cell cultures. Once the image is segmented, the approximate number of cells, computed as a quotient of area size and the average cell size, can be determined. His approach does not allow to segment any single cell.

Vliet [103] has proposed a method to detect malignant and normal cells in Pap smears as a support in a breast cancer diagnosis. The author used a combination of morphological and clustering methods with watershed to segment both types of cells. The problem of under- and oversegmentation was not addressed, and the report does not contain any numerical results.

Results obtained by Ji, Engel and Craine [44] are based on texture features that help a physician to evaluate various patterns in colposcopic images. Vascular structures are extracted from original cervical lesion images that are later on vectorized by line segments. First and second order statistics calculated from the distribution of extracted line segments (in terms of length and orientation) are then used to construct 24 features. The classification was performed with the minimum-distance classifier for all features and their subset representing most discriminant ones.

Walker [105] overviewed texture based methods aimed at classifying images of Pap smears from the

cervix. The features obtained from the gray level co-occurence matrix, Gibbs and Markov fields, statistical geometrical features [106] were compared with each other. The author concluded that methods based on random fields outperforms the others. It was also shown that author's original self-adaptive multi-scale technique allows the simultaneous capture of texture characteristics at, and across, several spatial resolutions. The method proved to be more accurate than standard approaches. It also captures characteristics that can be used to identify image locations where differences between texture classes occur. Finally, the broad applicability of all methods by classifying a wide spectrum of texture images from natural, industrial and biological origins was demonstrated.

However, to the best of our knowledge, the use of texture analyzing techniques to support the diagnosis of cervical cancer with the phase contrast microscopy has not been addressed so far in the literature.

A statistical algorithm is proposed to characterize and recognize textural patterns in epithelial cells. It follows a three stage process. At first, the original image is divided into regions. From each Statistical Geometrical Features (SGF) are extracted. Then, the most discriminant features are selected and used to classify image regions. Finally, post processing steps refine the classification results and an active contour model is employed to locate membranes of epithelial cells.

The proposed approach captures Statistical Geometrical Features that are essential for detection of epithelial cells in phase contrast images. These features are used to classify image regions into three classes: background, cell membrane and cell cytoplasm. The process includes three steps: pre-processing, feature extraction and selection, classification. Detection of exact shape of cell membranes is achieved by combining an active contour model with a gradient vector field and postprocessing steps. Detailed description of the stages follows.

Pre-processing

At first, an original image was linearly transformed into 8-bit gray level image with a contrast stretching technique [24]. Because the calculation of SGF for common 255 gray-scale levels is a tedious task, the number of gray levels was reduced to 16. The similar approach employed in [106] did not cause a remarkable lost of texture information. In the next stage, each image was divided into 1131 overlapping regions of the size 32×32 pixels each. The size of windows was chosen taking into account a constant magnification of the sample, the image size and ability of a window to capture essential texture features. For each region a set of statistical geometrical features was generated. As various features differ in range of their values, the scaling of features was performed to ensure reliable distance calculations in the features' space. The normalization guaranteed that each feature has the zero mean and the unit standard deviation [13].

Finally, the feature vector was used to assign a class label to the center of each 32×32 window. Because not always the boundary between different textures overlayed with windows, the latter ones were additionally shifted half of the window size.

Feature extraction and selection

Statistical Geometrical Features are recalled following Chen work [13] where a discrete gray-level image window[2] of $M \times N$ size is described as 2D function $I(x,y)$ where $(x,y) \in [0,1,...,M-1] \times [0,1,...,N-1]$ and $I(x,y) \in L = \{0,...,N_L-1\}$. $I(x,y)$ corresponds to the intensity of the pixel at (x,y). The image is then decomposed into a set of thresholded images with a threshold value $\alpha \in L$:

$$I_k(x,y;\alpha) = \begin{cases} 1 & \text{if } I(x,y) \geq \alpha, \\ 0 & \text{otherwise} \end{cases} \qquad (4.7)$$

---

[2] Here, the window is equivalent to region of the size 32×32. The number of gray levels $\#L = 15$.

where $I_k(x, y; \alpha)$ denotes a binary image after the threshold operation with the cut-off value α. The original image is then split into $N_L - 1$ binary images

$$I(x, y) = \sum_{\alpha=1}^{l-1} I_k(x, y; \alpha) \tag{4.8}$$

and the mapping is bijective, i.e. no information is lost. For each image $I_k(x, y; \alpha)$, the number of connected regions is calculated and denoted $NOC_1(\alpha)$ for connected regions of 1-valued pixels and $NOC_0(\alpha)$ for connected regions of 0-valued pixels. The connected region is understood as a set of pixels of the same value (0 or 1) that are adjacent to each other in 4-neighborhood sense. These measures are used to define 16 features that are further characterized by five statistics: minValue, max-Value, averageValue, sampleMean and sampleStandardDeviation. Therefore, for each texture image 80 features are obtained. Their definition can be found in Appendix A.

The aim of the feature selection algorithm is to select the optimal subset of features from the original feature set [42, 108]. There are many methods discussed in the literature to deal with this task. Generally they can be divided into 'bottom-up' and 'top-down' approaches, both including optimal and sub-optimal methods. The first approach starts with an empty feature set and the optimal subset is built up incrementally. The second one starts with the full feature set and removes redundant features successfully. Optimal methods, like Monte Carlo methods, simulated annealing, genetic algorithms or branch and bound procedure, involve a deep search for the solution and they are feasible for simple problems only, whereas suboptimal methods use different optimization techniques to reduce computational costs. They include sequential forward selection (SFS) and sequential backward selection methods (SBS). During this incremental process a feature that yields the extremal value of a criterion function $J(\cdot)$ is added or removed to the current feature set until the prescribed number of features is obtained or the feature set deteriorates the classification. The criterion function $J(\cdot)$ is related to some measures of distance or dissimilarity between distributions of features. A clear disadvantage of these methods is that no revision of previously made decisions is allowed. However, updates are possible in sequential forward floating selection (SFFS) method [11]. The algorithm starts with an empty feature set and, in each step, the best feature that satisfies the given criterion function is added to the current feature set, i.e. one step of the SFS is performed. The algorithm also verifies possibility of improvement of the criterion if one feature is excluded. In this case, the worst feature (w.r.t. the criterion) is eliminated from the set and one step of the SBS is carried out. Therefore, the SFFS proceeds dynamically by increasing and decreasing the number of features until their prescribed number is reached.

Basically, there are two approaches to define a criterion function $J(\cdot)$. The first one designs a classifier for a reduced number of features and chooses the features' set that performs well on separated training/test sets by calculating its error rate. The second approach estimates the distance between distributions of class-conditional probabilities and favors those features' sets that maximize the class separability. This approach is independent of the classifier and it is relatively cheap to implement but certain assumptions about the form of distribution have to be made.

In our case, n d-dimensional feature vectors $\mathbf{x} = (x_1, ..., x_d)$ ($x \in \mathcal{X}^d, d = 80$) were generated (number of vectors $n = 1131$). To select optimal combination of d^* features ($1 < d^* < 80$) the SFFS selection method was used with one of three criterion functions (classification error rate of Fisher Linear Discriminant (FLD) classifier, Bhattacharyya Distance and scatter matrices). The latter two measures are defined only for bi-class case. Therefore, in multi-class problems ($\Omega = \{\omega_i\}$, $i = 1..C$), the pairwise distance measures must be adopted, where the final criterion function is equal to the sum of pairwise combinations[108]:

$$J(\omega_i, \omega_j) = \sum_{i,j=1}^{C} P(\omega_i) P(\omega_j) J_{ij}.$$

J_{ij} denotes a criterion function between two classes ω_i and ω_j.

The *Bhattacharyya distance* measures the distance between two distributions. Because the measure requires to estimate probability density functions and its numerical integration, the assumption about the form of these distribution usually simplifies the calculations. In our case normally distributed density functions were assumed with means μ_1 and μ_2 and covariance matrices Cov_1 and Cov_2 estimated from the training data. Therefore, the Bhattacharyya distance

$$J_{12}^B(\omega_1, \omega_2) = -\log \int\limits_X \left(p(\mathbf{x}|\omega_1)p(\mathbf{x}|\omega_2) \right)^{\frac{1}{2}} d\mathbf{x}. \tag{4.9}$$

can be simplified to the form

$$J_{12}^B(\omega_1, \omega_2) = \frac{1}{4}(\mu_2 - \mu_1)^T (Cov_1 + Cov_2)^{-1} (\mu_2 - \mu_1) + \frac{1}{2}\log\left(\frac{|Cov_1 + Cov_2|}{2\left(|Cov_1||Cov_2|\right)^{\frac{1}{2}}} \right) \tag{4.10}$$

where $|\cdot|$ denotes determinant of a matrix. The covariance matrix and the group mean for the class ω_i are defined as follows:

$$Cov_i = \frac{1}{n_i} \sum_{j=1}^{n} z_{ij} \left(x_j - \mu_i \right) \left(x_j - \mu_i \right)^T$$

$$\mu_i = \frac{1}{n_i} \sum_{\mathbf{x} \in \omega_i} \mathbf{x} \tag{4.11}$$

where n_i is the number of samples in class ω_i. $z_{ij} = 1$ if $x_j \in \omega_i$ and 0 otherwise.

Scatter matrices [108] define another distance measure between data sets that aims to find a set of features for which the within-class spread is small and the between-class one is large:

$$J^S = \mathrm{Tr}\left(\mathbf{S}_W^{-1} \mathbf{S}_B \right) \tag{4.12}$$

where

$$\mathbf{S}_W = \sum_{i=1}^{C} \frac{n_i}{n} Cov_i \tag{4.13}$$

denotes the scatter matrix within the class and

$$\mathbf{S}_B = \sum_{i=1}^{C} \frac{n_i}{n} (\mu_i - \mu)(\mu_i - \mu)^T \tag{4.14}$$

is the scatter matrix between classes. In Eq. (4.12) $Tr(\cdot)$ stands for the trace operator of a matrix and the sample mean is defined as

$$\mu = \sum_{i=1}^{C} \frac{n_i}{n} \mu_i$$

where n denotes number of patterns. The *recognition rate*, defined as the percentage of correct classified samples, can be also used to determine the optimal number of features. In this case, for a given subset of features a criterion function $J(\cdot)$ is equal to the recognition rate of FLD classifier.

In order to avoid the *apparent error rate* (present when data used to design a classifier are also used to estimate the classification error rate), each obtained feature set with a given d^* and the criterion function $J(\cdot)$ was verified using the cross-validation method [21] as follows. Data were separated into 10 disjoint sets. In turn, one of them served as a test set while the others formed a training set. The final classification error rate, defined as the mean value of error rates of FLD classifier calculated for each setting, derived the estimation of the optimal number of features.
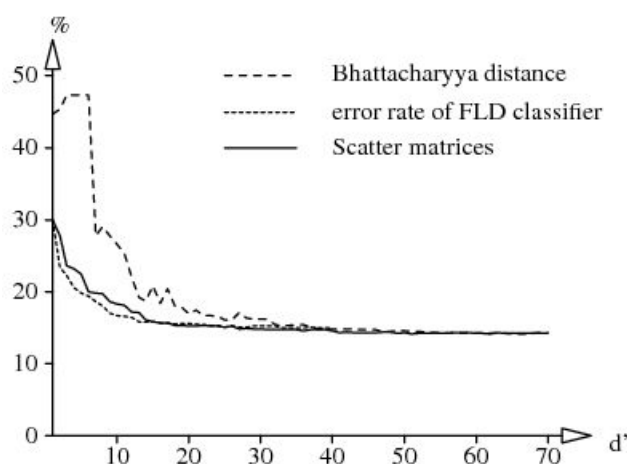
Figure 4.6. Comparison of feature selection methods. The diagram presents the optimal number of feature d^* vs. classification error.

Criterion function	FLD	Bhattacharyya distance	Scatter atrices
Classification error	15,6	16,9	15,2

Table 4.2. Classification error [%] for $d^* = 20$ features.

The mean classification error rates for different number of features are depicted in Fig. 4.6. It can be noticed that the classification error is relatively constant for at least 20 features. Therefore, three $J(\cdot)$ distance measures were compared for $d^* = 20$ (see Tab.4.2). Once, d^* was estimated, SFFS was again applied to select the best 20 features with a distance measure based on scatter matrices.

The list of selected features is presented in Appendix (Tab.A.1).

Classification

The following classifiers were tested with SFFS method and scatter matrices used as distance measures: k-nearest-neighbor classifier (kNN), Fisher Linear Discriminant (FLD) and Kernel Fisher Discriminant (KFD) as examples of linear and non-linear discriminants.

The kNN classifier assigns the feature vector $\mathbf{x}$ to this class that receives majority of votes amongst the k nearest neighbors in the feature space (see Fig.4.7):

Definition 9. *Assign a feature vector $\mathbf{x}$ to the class $\omega_m \Leftrightarrow \forall_i k_m \geq k_i$ where $k_m \in \omega_m$ and $\sum_{i=1}^{C} k_i = k$.*
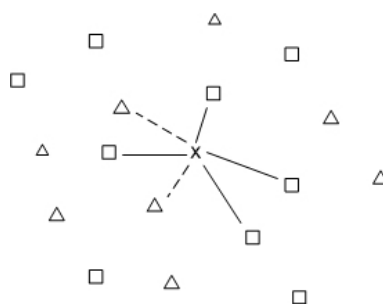

Figure 4.7. An example classification. Two classes from the training set are represented by rectangles (ω_1) and triangles (ω_2). A new feature vector $\mathbf{x}$ is assigned to the ω_1 because it received majority of votes amongst $k = 6$ nearest neighbors. In this example $k_1 = 4$ (solid lines) and $k_2 = 2$ (dotted lines).
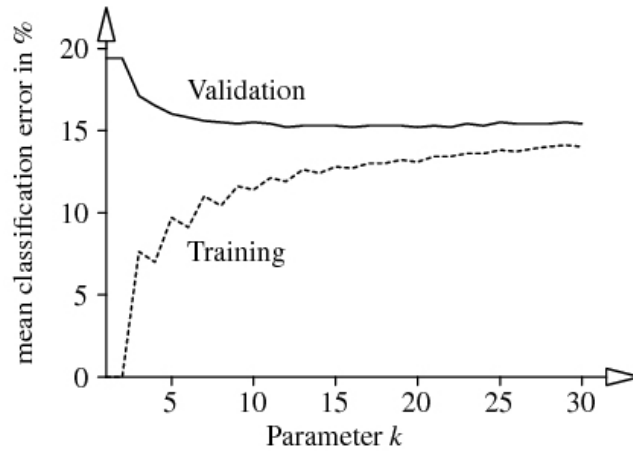
Figure 4.8. Estimation of the *k* parameter with cross-validation and Euclidean metric (Dasarthy,1991). The minimal value of the average classification error (15.2%) for $k = 20$.

The choice of the parameter *k* and the metric are crucial for classification. Here, the Euclidean distance was applied. The *k* parameter is estimated by previously described fivefold cross-validation technique where data are split into two parts, the validation (test) and training sets. The latter set is used to adjust the *k* variable. The validation set is used to estimate the generalization error which is a measure of the true error between the hypothesis and the true target function. Typically one can not measure it directly, instead it can approximated by measuring the performance of a parameter on an independent test set.

The classifier is trained until the minimum value of this error is found. The minimal value of the average classification error (15, 2%) corresponds to $k = 20$ (Fig.4.8). Therefore, this value was chosen as the classifier parameter. Classification results are presented in Tab. 4.3 in the form of a confusion matrix [108] which shows the decomposition of the error rate (see Chapter 2.1). The (i, j)th element of this matrix is the number of patterns of class ω_j that are classified as class ω_i by the classifier.

FLD projects high-dimensional data onto a line and performs classification in one dimensional space [108]. More precisely, a direction **w** that separates two classes is sought. The vector **w** that maximizes $J(\cdot)$ leads to the best separation between two sets:

$$J(\mathbf{w}) = \frac{\mathbf{w}^T \mathbf{S}_B \mathbf{w}}{\mathbf{w}^T \mathbf{S}_W \mathbf{w}} \tag{4.15}$$

where $\mathbf{S}_W$ and $\mathbf{S}_B$ are called within-class and between class scatter matrices (cf. Eqs. (4.13) and (4.14)). Because $\mathbf{S}_B \mathbf{w}$ points in the direction of $\mathbf{m_1} - \mathbf{m_2}$, the optimal **w** that optimizes $J(\cdot)$ can be written as:

$$\mathbf{w} = \mathbf{S}_w^{-1}(\mathbf{m_2} - \mathbf{m_2}) \tag{4.16}$$

where $\mathbf{m_1}$ and $\mathbf{m_2}$ are groups' mean.

The results of classification are presented in Tab 4.3. As previously, the fivefold cross-validation of data was performed.

For the case of *C* classes the One-Against-One methods is applied. $C - 1$ classifiers are constructed where each of them discriminates patterns between two classes. A pattern **x** is classified using each classifier in turn, and a majority vote is chosen. In the end, a feature vector is classified into the class that was chosen most frequently.

In contrary to linear classifiers, KFD performs the classification using non linear functions. The method, originally used in functional interpolation problems, was first applied for discrimination by
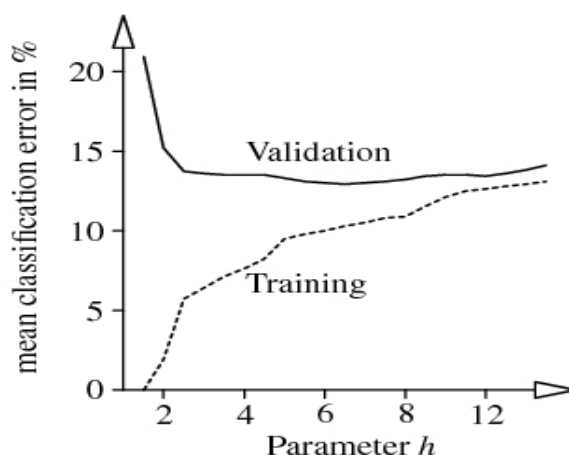
Figure 4.9. Estimation of the *h* with fivefold cross-validation. The minimal value of the average classification error (12.9%) for $h = 5.5$.

True class	Predicted class								
	Background			Cytoplasm			Cell membrane		
Classifier	kNN	FLD	KFD	kNN	FLD	KFD	kNN	FLD	KFD
Background	**49,1**	**49,2**	**50,7**	5,5	3,5	3,3	1,0	2,4	1,1
Cytoplasm	2,2	2,7	2,7	**30,3**	**27,6**	**29,7**	1,5	3,6	1,6
Cell membrane	1,9	1,2	2,1	3,8	1,8	2,5	**5,2**	**8,0**	**6,4**

Table 4.3. Confusion matrix on the training set for kNN, FLD and KFD classifier. Accuracies of each of classifiers, computed from the matrix trace, are equal to 84,6% ($= 49,1\% + 30,3\% + 5,2\%$), 84,8% and 86,8% respectively.

Broomhead and Lowe [9]. KFD may be described as a linear combination of radially symmetric non linear basis functions [108]. In our case, the exponential basis function $\phi(\cdot)$ was employed:

$$\phi(\mathbf{x}, \mu) = \exp \left\{ -\frac{\|\mathbf{x} - \mu\|^2}{h} \right\}. \tag{4.17}$$

Its parameter *h* was estimated by the fivefold cross-correlation method. The minimal value of classification error was obtained for $h = 5.5$ (Fig. 4.9). Therefore, this value was used as the parameter classifier.

Results of classification with kNN, FLD and KFD are presented in Tab. 4.3. The trace of the matrix corresponds to the accuracy of each classifier. The best accuracy is achieved by KFD and further justifies the choice of this classifier.

Post-processing

Image regions were classified independently with the KFD classifier. Therefore a certain misclassification error is likely to occur. By introducing three classes: background, cytoplasm and cell membrane and taking the a-priori knowledge into consideration, classification errors were reduced when the following rules were applied:

1. background regions surrounded entirely by the cytoplasm were marked as cytoplasm,
2. small regions classified as the cell membrane and cytoplasm were marked as background,

3. cell membrane regions must be adjacent to the background (Note: the true cell membrane between clustered or overlapped cells are considered as medically unimportant) and is limited in width. Redundant cell membrane regions were marked as background),

4. only large 4-neighborhood connected objects were considered as potential cells (the minimal cell size is induced by the microscope magnification. The average cells size was approximated manually),

5. the adjacency between potential cells and cell membrane regions was measured by the 8-connected neighborhood rule

Boundaries of potential cells formed final cell membrane regions where the active contour was initialized.

(a) Initial classification

(b) Post-processed image

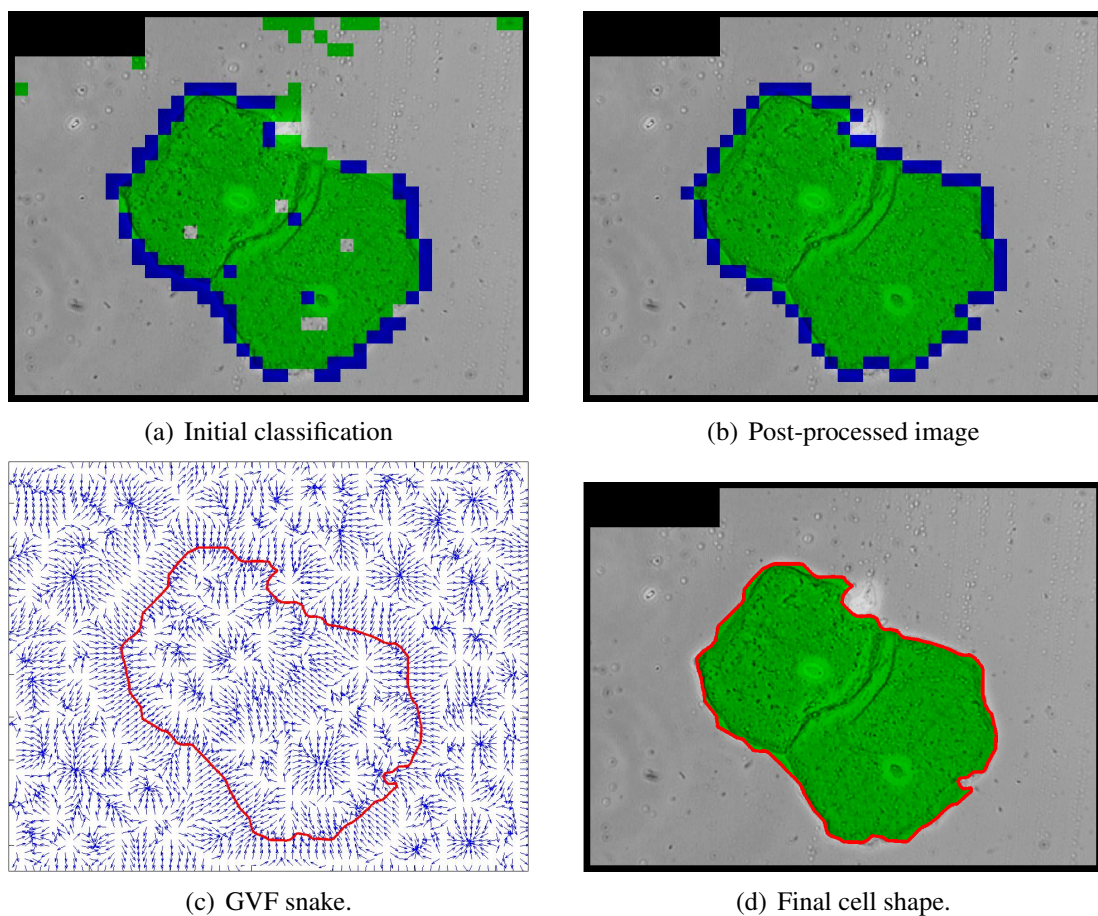(c) GVF snake.

(d) Final cell shape.

Figure 4.10. Segmented image (a) and its post-processed version (b). Detected cytoplasm is marked in light gray and the cell membrane in black. The snake initialized on the GVF (c) and final segmentation of the cell membrane (d).

GVF snakes in cell membrane detection

Precise detection of cells requires a reliable location of their membranes. The detected cell membrane contour should not include any holes and should fit to the real cell membrane. In our approach, an active contour model is applied that employs the Gradient Vector Field (GVF) developed by Xu and Prince[111]. Active Contour Models, often referred in the literature as snake models, have been extensively used in image processing and computer vision applications to detect boundaries of objects. To show advantages of the applied method, first, the classic snake model is recalled.

The traditional snake model is given as a 2-D parametric curve [111] $\mathbf{v}(s) = (x(s), y(s))^T$ where $s \in [0,1]$ is the running variable. The snake is moved in the image domain by minimizing the energy function:

$$E(\mathbf{v}(\cdot)) = \int_0^1 \left(\frac{1}{2} \left(\alpha \left| \mathbf{v}'(s) \right|^2 + \beta \left| \mathbf{v}''(s) \right|^2 \right) + E_{ext}(\mathbf{v}(s)) \right) ds \qquad (4.18)$$

where α and β are weighting parameters that control the snake's tension and rigidity, and $\mathbf{v}'(s) \; \mathbf{v}''(s)$ stands for the first and the second order derivatives w.r.t. the variable s:

$$\mathbf{v}'(s) = \begin{bmatrix} \frac{\partial x}{\partial s} \\ \frac{\partial y}{\partial s} \end{bmatrix}, \; \mathbf{v}''(s) = \begin{bmatrix} \frac{\partial^2 x}{\partial s^2} \\ \frac{\partial^2 y}{\partial s^2} \end{bmatrix},$$

E_{ext} is derived directly from an image and it attains small values at edges. A snake that minimizes the energy function must satisfy the Euler equation:

$$\alpha \mathbf{v}''(s) - \beta \mathbf{v}''''(s) - \nabla E_{ext}(s) = 0 \qquad (4.19)$$

where the internal force $F_{int}(s) = \alpha \mathbf{v}''(s) - \beta \mathbf{v}''''(s)$ prevents the snake from stretching and bending while the external force $F_{ext}(s) = -\nabla E_{ext}(s)$ moves the snake into the direction of gradients of intensity. ∇ denotes the gradient operator:

$$\nabla = \left(\frac{\partial}{\partial x}, \frac{\partial}{\partial y} \right)^T$$

The transient solution of Eq. (4.19) expresses $\mathbf{v}$ as the function of time t and space s variables:

$$\frac{\partial \mathbf{v}(s,t)}{\partial t} = \alpha \mathbf{v}''(s,t) - \beta \mathbf{v}''''(s,t) - \nabla E_{ext}(s). \qquad (4.20)$$

This term vanishes when the solution of Eq. (4.20) stabilizes and the solution of Eq. (4.19) is achieved.

The standard snake model that minimizes the energy defined as a sum of external and internal forces displays poor converge capabilities. The external forces point correctly toward concavities but when the concavity is reached forces point into opposite directions and no further snake deformations are possible. As cells often have irregular shapes, an improved snake model, called GVF snake, was applied to improve location capabilities. The model employs the GVF field [111] and replaces the external force $-\nabla E_{ext}(s)$ by a field ζ changing the standard model into:

$$\frac{\partial \mathbf{v}(s,t)}{\partial t} = \alpha \mathbf{v}''(s,t) - \beta \mathbf{v}''''(s,t) + \zeta. \qquad (4.21)$$

where the vector field $\zeta(x,y) = (a(x,y), b(x,y))^T$ is defined in the image domain and it minimizes the following energy functional:

$$\varepsilon(x,y) = \int_{x-\Delta x}^{x+\Delta x} \int_{y-\Delta y}^{y+\Delta y} \eta(a_x^2 + a_y^2 + b_x^2 + b_y^2) + ||\nabla e||^2 \cdot ||\zeta - \nabla e||^2 dxdy \qquad (4.22)$$

where Δx, Δy are some small parameters and $|| \cdot ||$ denotes the Euclidean norm. a_x, b_x, a_y, b_y are partial derivatives w.r.t coordinates x and y. $e(\cdot, \cdot)$ is an edge map derived from the image I, it is larger near image edges and can be computed by gradient operators. The regularization parameter η governs the trade-off between the first and second term in the integrand. It depends on the noise level in the image (more noise, increase η). The GVF snake is solved numerically by discretization and iteration [111].

The classified image and the results of post processing are presented in Fig 4.10(a) and Fig.4.10(b). The example of detection of the cell membrane with GVF Snakes is depicted in Fig 4.10(d).

True class	predicted class		
	Background	Cytoplasm	Cell membrane
Background	53,1	2,0	1,3
Cytoplasm	1,9	29,4	1,8
Cell membrane	1,9	2,7	5,9

Table 4.4. Confusion matrix on the test set (in %) for the KFD classifier with SGF-features. Accuracy of the classifier is 88,4 %.

True class	predicted class		
	Background	Cytoplasm	Cell membrane
Background	48,1	4,4	3,9
Cytoplasm	3,1	26,5	3,5
Cell membrane	1,2	1,7	7,6

Table 4.5. Confusion matrix computed on the test set (in %) for the FLD classifier with GLCM-features. Accuracy of the classifier is 82,2%.

Simulations

Available images were split into two disjoint data sets: test set included 69 images and training set was composed of 16 images. Each image was divided into 1131 overlapping regions of size 32×32 pixels. For each region a set of statistical geometrical features was generated and then normalized forming a feature vector. SSFS selection method reduced the number of features to the most discriminant ones (20 out of 80 features were selected). Each region was represented as a point in 20 dimensional feature space $\mathcal{X}$. The classification was performed with the Kernel Fisher Discriminant as follows. A window of size 32×32, was moved along the image and its middle part (16×16) was assigned to one of three pre-defined classes (background, cytoplasm or cell membrane). 30 regions in the left upper image corner that included the patient data were not considered.

The comparison of results with expert's segmentation showed that 88,4 % of windows were classified correctly. The algorithm was implemented in MATLAB and run on PC with AMD Sempron 1,67 GHz. Generation of SGF feature set took 114 [sec] per image. The training process, performed only once, took 8 min. and the classification of each image lasted 11 sec.

In order to compare the feasibility of SGF features, another set of texture features was chosen. This feature set was also used in a similar task where alive and dead cells observed in phase contrast images should be detected and classified [59]. Features were calculated from a histogram and the gray-level co-occurrence matrix (GLCM) for the same regions from the training set. Similarly, each region was represented by a feature vector and then classified into three classes: alive, dead cells and background.

Similarly to [59] original images were firstly pre-processed, where the number of gray-levels was reduced to 16, divided into regions and then classified with selected first order and second order features computed from the GLCM for distance $\pi = 1, 2, 3, 4, 5$ and angle $\theta = 0°, 45°, 90°, 135°$. The region size was again 32×32 and 16×16. The classification was performed with FLD. The classification results with GLCM features are presented in Tab. 4.5. Calculation of GLCM features requires 267 [sec] per image. The training took 13 [sec] and classification of each image 5 [sec]. Definitions of GLCM features are presented in Appendix A.

The alternative method, although much faster, brings worse results, only 82,2% of regions were classified correctly.

Also, the detection of the cell membrane with GVF snake was compared against standard snake model
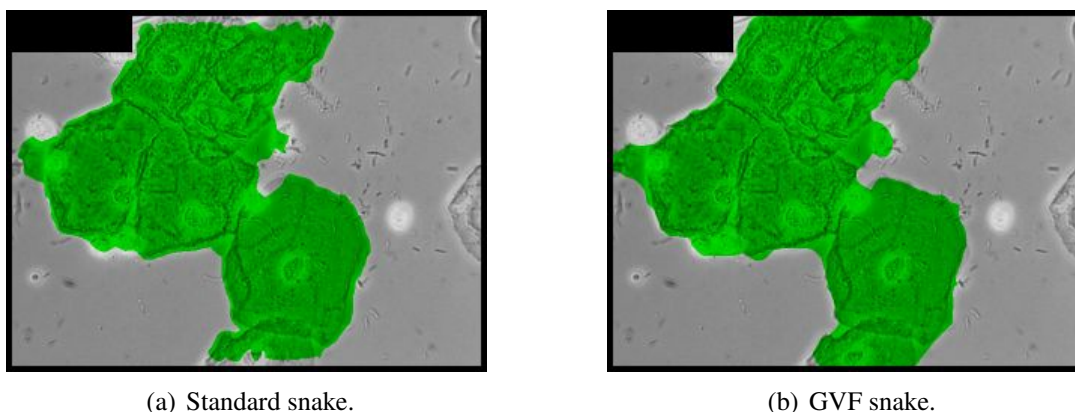
(a) Standard snake.

(b) GVF snake.

Figure 4.11. Comparison of standard and GVF snake.

(a) Intermediate cells

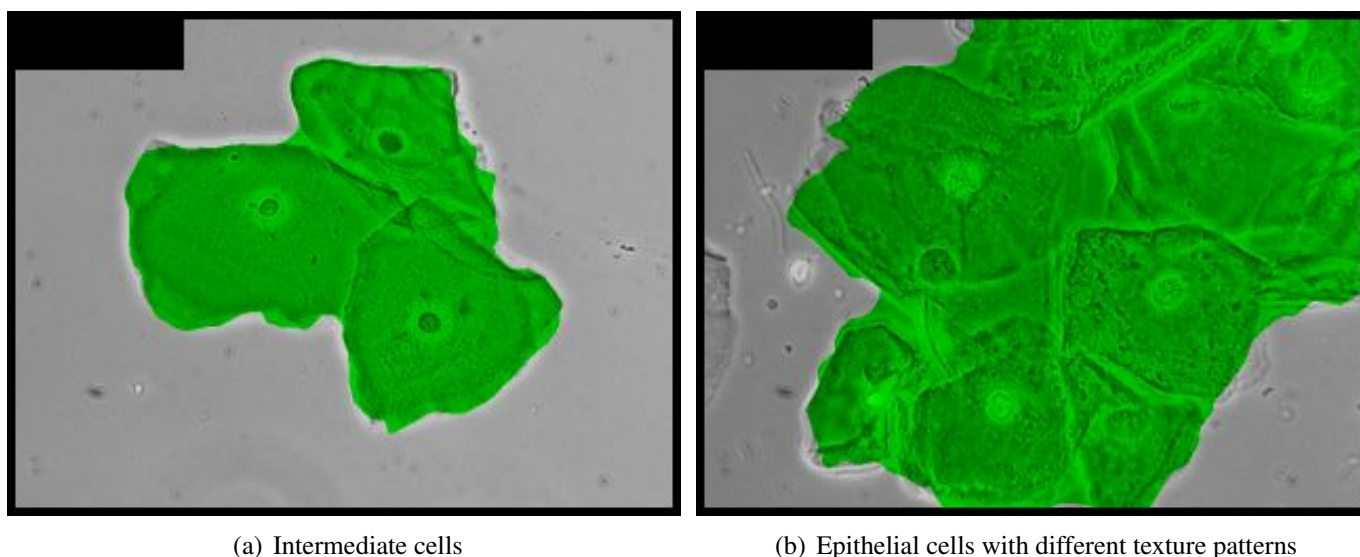(b) Epithelial cells with different texture patterns

Figure 4.12. Segmented intermediate cells (a). Segmented epithelial cells with different texture patterns (b)

where the external force was calculated directly from the smoothed image. The calculation of the first model took at average 2 [sec]. The snake overlapped true cell membrane in 94% of cells in average.

The calculation of 50 iterations of the GVF field took about 104 [sec] per image. Next, the field was used to calculate the GVF Snake. 3 [sec] was enough to achieve accuracy of 95% at average. These results show that the GVF snake offers only a slightly better segmentation and much longer computational time. However, the method is less sensitive to local intensity fluctuations at the cell membrane and performs better at image borders (see Fig. 4.11). Therefore, its usage should be limited to poor quality images and those applications where the entire cell should be segmented.

Figs. 4.11, 4.12 and 4.13 present a few segmentation examples. It can be noticed that the method works well for different kinds of cytoplasm. Basal, parabasal, intermediate and superficial cells were detected. While the background and numerous bacteria were not captured. When granulocytes were inside the cytoplasm or when cells overlapped the method failed. In the first case, the algorithm left them untouched because of their similarity to nuclei. Snake seems to be pulled in the direction of the inner cell membrane which results in false outline of the cytoplasm.
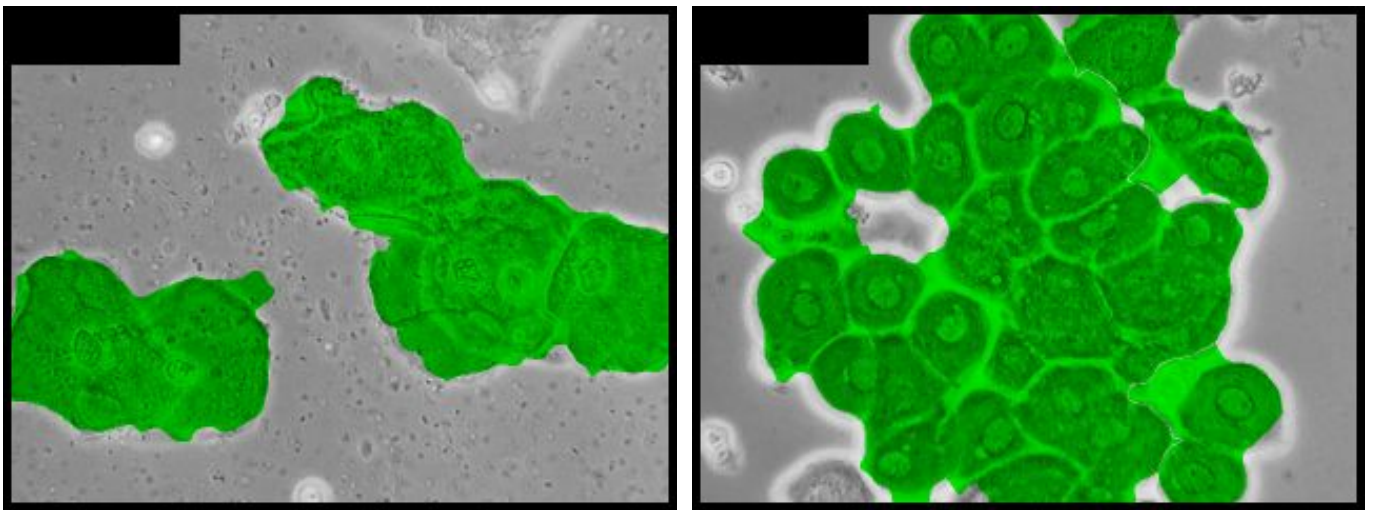
<div align="center">(a) Contaminated medium   (b) Basal cells</div>

Figure 4.13. Segmented cells flowing in the contaminated medium (a) and an example of segmented basal cells (b).

5. esiImage Software

Recently automated microscopes have been developed that acquire large amounts of images of biological samples. The huge amount of data collected in these experiments require the development of image processing software to find and quantify differences and similarities within the data sets. To allow flexible analysis of large numbers of microscopy images the esiImage application was developed [70]. In comparison to commercial software like [27, 58], Velocity[1], Imaris[2] or Cellenger[3] that offer a limited number of algorithms which implementation is hidden from the user, the open architecture of esiImage and access to the ImageJ [82] image processing library allows a simple integration of any image processing algorithm. Generated results can be easily incorporated in other systems for further analysis. The software was written in Java.

There is a graphical user interface (see Fig. 5.1) and a list of available algorithms that analyze images. The user interface simplifies the choice of images to analyze and presents the results immediately. The esiImage allows processing of images acquired by any type of microscopy technique. It is also possible to process the combination of fluorescence channels or different modalities (fluorescence and phase contrast) in cases when the sample is imaged with multiple microscopy techniques. The number of fluorescence channels and declaration of modalities as well as other settings (experiment description) is defined in separated XML file and loaded at the application startup. It allows to automate processing of images and set-up specific for the machine. This feature is useful to process numerous images when the module is run in parallel on different machines as separated software.

The software has been extensively used in the Max Planck Institute of Cell Biology and Genetics (Dresden, Germany) in a high-throughput screening experiment where 1389 genes, essential for cell cycle progression in human cells, were examined [52]. The software analyzed about a hundred of thousand images and calculated the mitotic index as one among nine parameters that formed a phenotypic signature. This pattern was later used to assign novel cell cycle functions to genes by combining hierarchical clustering, bioinformatics and proteomic data mining.

The current implementation of the software comprises methods described in Sec. 3 and was applied to evaluate the algorithms.

The next step is a combination of the esiImage with a larger system, called Open Screening Environment. The system is designed for managing and analyzing all areas of high throughput screening experiments. It integrates information about produced biological compounds, their use, screen parameters (date, experiment conditions, equipment) and imaging techniques applied and provides access to most common biological databases. The system tracks the complete screening process starting from production of biological and chemical compounds, their application in assays and evaluates their influence on cells by analyzing images generated during experiments. The role of the esiImage will be to store and process images or movies. Its results will be later analyzed by other data mining modules to describe relations between existing phenotypes or to detect new ones.

---

[1] www.improvision.com
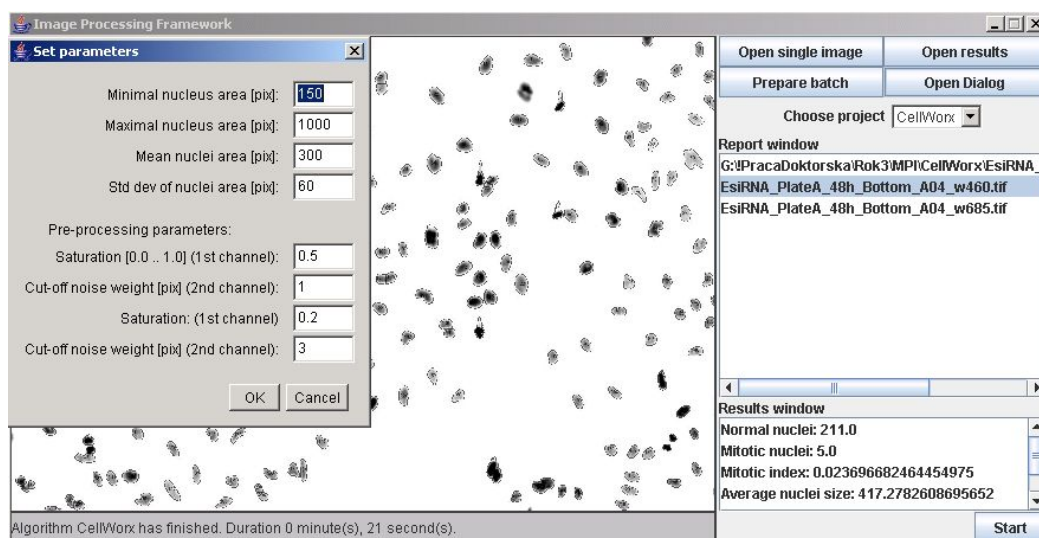[2] www.imaris.com
[3] www.cellenger.com

Figure 5.1. The graphical user interface of the esiImage.

6. Conclusions

The PhD thesis presents two algorithms that process multimodal, microscopic images and is aimed at supporting the gene function study and the diagnosis of the cervical cancer. Both methods analyze raw, noisy and uneven illuminated images with target objects often being unstructured and contaminated.

The first method analyzes images from two different sources (phase contrast and fluorescence) and calculates the mitotic index. It detects and classifies mitotic, normal and dead cells from fluorescence and phase contrast images. The method was tested on different cell lines imaged by different phase contrast and fluorescence techniques. The algorithm comprises a number of image processing methods adopted for the image class or originally developed. The method was experimentally evaluated to calculate the mitotic index in time lapse movies of the gene CDC16. Results derived by the algorithm were consistent with the theory. Further, the method allows to analyze the characteristics of the mitotic index and may result in a detection of additional phenotypes. Alternative cell segmentation method based on the Markov Random Fields was also evaluated.

Different filtering and pre-processing methods emphasizing fluorescence signal were evaluated, such as contrast stretching followed by band-pass filter in the Fourier space or the rolling ball algorithm as a shading correction method. It was shown that pre-processing methods effectively improved the watershed segmentation applied to detect nuclei. The cross-correlation method of the phase contrast image with a set of templates resulted in a correlation map from which the exact position of mitotic cells could be deduced. The decision was supported by post-processing steps based on the innovative, evolutionary validation approach. For comparison purposes a gradient based original method was also considered. There are three main contributions. The first is the original method flow that includes three stages of analysis: pre-processing, segmentation and classification. Each of the stage was considered equally important and a considerable effort was made to combine the stages into a complementary and consistent system. The second one is the demonstration that multimodality simplified detection and classification of cells by combining features from different sources. The experimental advantage of the method is a reduced exposure of cells to fluorescence light. The addition of least harmful stain allows to analyze living cells and limit the effect of photobleaching. A novelty is also present in the combination of classifiers into a "cascade" which allows background regions of the image to be quickly discarded while spending more computation time on promising regions.

The active vision based analysis of regions of interest consisted in a segmentation of a filtered fluorescence signal and focusing the attention only on those image regions that contained information. More sophisticated classifiers could reason about the cell type on the basis of chosen features. Linear discriminant proved to be more efficient than its quadratic equivalent.

Since the majority of dyes immobilize cells, multimodal analysis that combined a less harmful fluorescence stain with the phase contrast microscopy - the least toxic observation method - extend possible applications to those that also examine the cell behavior and kinematics. Although not realized, a cell tracking algorithm is a natural extension of presented considerations. However, it seems that independent recognition of cells in consecutive frames is a rather futile approach because results from previous frames are not considered and misclassification is more likely to occur. Also, features of higher order, such as texture features, could be sufficient to classify cells only from fluorescence images.

The analysis of phase contrast images in the gynecology is treated in sequel. A method supporting cervical cancer diagnosis was developed that processes images acquired by phase contrast microscope. The method analyzes images, removes elements that are not important for the diagnosis and marks only epithelial cells. The method comprises algorithms known from the literature, adapted to the problem. Statistical Geometrical Features were used to construct a feature set used to classify image regions. By using the Sequential Forward Floating Selection method the number of features was reduced to most significant ones. k-Nearest Neighbors classifier, Fisher Linear Discriminant and Kernel Fisher Discriminant were evaluated as potential classifiers. The last method seemed to be most reliable. An active contour model was chosen to detect a cell contour. As an alternative approach features from GLCM matrix were evaluated. By presenting to a cytopathologist only images with relevant, cytological structures, the system unburdens a physician from examination of messy data and, in that way, improves the diagnosis of cervical cancer.

The main contribution in this stream is a novel combination of already known methods into a reliable system. To the author's knowledge, there are no other systems that back the diagnosis of cervical cancer with phase contrast microscopy. Therefore, the method could contribute to the propagation of the phase contrast microscopy in cervical cancer screening.

Finally, to test the performance of algorithms, the application, called esiImage, was implemented. The software allows processing of images acquired by any type of microscopy technique. It is also possible to process a combination of fluorescence channels or different modalities (fluorescence and phase contrast) in cases when the sample is imaged with multiple microscopy techniques. Currently methods presented in Chapter 3 are implemented.

The developed software was extensively used in the Max Planck Institute of Cell Biology and Genetics to evaluate the function related to the cell cycle of novel genes. Selective filtering of images with cervical smears was also successfully employed as a first analysis step in the application where malignant lesions were detected. The computational time of each of algorithm was acceptable in both cases.

A. Definition of texture features

Statistical geometrical features [13, 105] are defined as follows. Irregurality of the jth region in the image $I_k(\cdot, \cdot; \alpha)$ is defined as:

$$IRGL_k(j, \alpha) = \frac{1 + \sqrt{\pi} \cdot \max_{i \in I} \sqrt{(x_i - \bar{x})^2 + (y_i - \bar{y})^2}}{\sqrt{\#I}} - 1, \tag{A.1}$$

where

$$\bar{x} = \frac{\sum_{i \in I} x_i}{\#I}, \quad \bar{y} = \frac{\sum_{i \in I} y_i}{\#I} \tag{A.2}$$

and $k \in \{0, 1\}$. I is the set of indices of all pixels connected in the jth region, $\#I$ denotes the number of elements in set I and $(\bar{x}, \bar{y})$ can be thought as the center of mass of the connected region.

The average of the irregularity of the region of k-valued pixels is defined as follows:

$$\overline{IRGL}_k(\alpha) = \frac{\sum_{j=1}^{NOC_k(\alpha)} NOP_k(j, \alpha) \cdot IRGL_k(j, \alpha)}{\sum_{j=1}^{NOC_k(\alpha)} NOP_k(j, \alpha)} \tag{A.3}$$

where $NOP_k(i, \alpha)$ is the number of k-valued pixels in the ith connected region in the $I_k(\cdot, \cdot, \alpha)$. Walker [105] defines other geometric measures:

$$MEANAREA_k(\alpha) = \frac{\sum_{j=1}^{NOC_k(\alpha)} NOP_k(j, \alpha)}{NOC_k(\alpha)} \tag{A.4}$$

where $NOC_k(\alpha)$ denotes the number of regions formed by k-valued pixels. The area size of regions built of k-valued pixels

$$TAREA_k(\alpha) = \sum_{j=1}^{NOC_k(\alpha)} NOP_k(j, \alpha), \tag{A.5}$$

the minimal size of the region

$$MINAREA_k(\alpha) = \min_{1 \leq j \leq NOC_k(\alpha)} NOP_k(j, \alpha), \tag{A.6}$$

the maximal size of the region

$$MAXAREA_k(\alpha) = \max_{1 \leq j \leq NOC_k(\alpha)} NOP_k(j, \alpha), \tag{A.7}$$

the variance of maximal regions

$$VARAREA_k(\alpha) = \frac{1}{NOC_k(\alpha) - 1} \sum_{j=1}^{NOC_k(\alpha)} (NOP_k(j, \alpha) - MEANAREA_k(\alpha))^2 \tag{A.8}$$

and the standard deviation of regions' size

$$STDAREA_k(\alpha) = \sqrt{MEANAREA_k(\alpha)}. \tag{A.9}$$

Therefore for given α and k there are 16 functions, which are further characterized by following statistics:

$$\text{max value} = \max_{1 \leq \alpha \leq N_L - 1} g(\alpha), \tag{A.10}$$

$$\text{min value} = \min_{1 \leq \alpha \leq N_L - 1} g(\alpha) \tag{A.11}$$

$$\text{mean} = \frac{1}{N_L - 1} \sum_{\alpha=1}^{N_L - 1} g(\alpha), \tag{A.12}$$

$$\text{sample mean} = \frac{1}{\sum_{\alpha=1}^{N_L - 1} g(\alpha)} \sum_{\alpha=1}^{N_L - 1} \alpha \cdot g(\alpha), \tag{A.13}$$

$$\text{std dev} = \sqrt{\frac{1}{\sum_{\alpha=1}^{N_L - 1} g(\alpha)} \sum_{\alpha=1}^{N_L - 1} (\alpha - \text{sample mean})^2 \cdot g(\alpha)}, \tag{A.14}$$

where N_L is the number of gray-scale levels and g is one of the functions NOC_k, $\overline{IRGL_k}$, $MEANAREA_k$, $TAREA_k$, $MINAREA_k$, $MAXAREA_k$, $VARAREA_k$ and $STDAREA_k$.

Altogether, there are 8 functions of α for regions made of 0-valued pixels and 8 for 1-valued pixels. For each of them 5 measures are calculated resulting in 80 features for an image.

	Feature	Region	SGF name
1.	max value	0	NOC
2.	std dev	0	NOC
3.	mean	1	NOC
4.	sample mean	1	NOC
5.	max value	0	IRGL
6.	min value	1	IRGL
7.	min value	0	TAREA
8.	std dev	0	TAREA
9.	min value	1	TAREA
10.	mean	1	TAREA
11.	min value	0	MAXAREA
12.	mean	0	MAXAREA
13.	std dev	0	MAXAREA
14.	mean	1	MAXAREA
15.	std dev	1	MAXAREA
16.	sample mean	1	MAXAREA
17.	mean	0	MINAREA
18.	mean	0	MEANAREA
19.	sample mean	1	MEANAREA
20.	mean	0	VARAREA

Table A.1. List of 20 features chosen with feature selection method based on scatter matrices.

List of 20 features chosen with feature selection method based on scatter matrices

GLCM features The gray-level co-occurrence matrix (GLCM) can reveal certain properties concerning the spatial distribution of the gray levels in the texture image. Each component of the GLCM,

$p_{\pi,\Theta}(z_i, z_j)$ is obtained by calculating how often a pixel with the intensity (gray-level) value z_i occurs in a specific spatial relationship (at the distance π and the angle Θ) to a pixel with the value z_j. The size of the GLCM is defined by the number of gray levels N_L. The following statistics can be computed from the GLCM.

$$\text{Second order angular moment:} \quad = \quad \Sigma_{z_i,z_j=0}^{N_L-1}[p(z_i,z_j)]^2 \tag{A.15}$$

$$\text{Contrast:} \quad = \quad \Sigma_{z_i,z_j=0}^{N_L-1}(z_i-z_j)^2 p(z_i,z_j) \tag{A.16}$$

$$\text{Correlation:} \quad = \quad \Sigma_{z_i,z_j=0}^{N_L-1}\frac{z_i z_j p(z_i,z_j)-\mu_x\mu_y}{\sigma_x\sigma_y} \tag{A.17}$$

$$\text{Sum of Squares:} \quad = \quad \Sigma_{z_i,z_j=0}^{N_L-1}(z_i-\mu_x)^2 p(z_i,z_j) \tag{A.18}$$

$$\text{Inverse Difference Moment:} \quad = \quad \Sigma_{z_i,z_j=0}^{N_L-1}\frac{p(z_i,z_j)}{1+(z_i-z_j)^2} \tag{A.19}$$

$$\text{Entropy:} \quad = \quad -\Sigma_{z_i,z_j=0}^{N_L-1}p(z_i,z_j)\log\left[p(z_i,z_j)\right] \tag{A.20}$$

$$\text{Sum Average:} \quad = \quad \Sigma_{z_i=0}^{2(N_L-1)}z_i p_{x+y}(z_i) \tag{A.21}$$

$$\text{Sum Variance:} \quad = \quad \Sigma_{z_i=0}^{2(N_L-1)}(z_i-\text{Sum Average})p_{x+y}(z_i) \tag{A.22}$$

$$\text{Sum Entropy:} \quad = \quad -\Sigma_{z_i=0}^{2(N_L-1)}p_{x+y}(z_i)\log\left[p_{x+y}(z_i)\right] \tag{A.23}$$

$$\text{Difference Variance:} \quad = \quad \Sigma_{z_i=0}^{2(N_L-1)}(z_i-\mu_{x-y})^2 p_{x-y}(z_i) \tag{A.24}$$

$$\text{Difference Entropy:} \quad = \quad \Sigma_{z_i=0}^{2(N_L-1)}p_{x-y}(z_i)\log\left[p_{x-y}(z_i)\right] \tag{A.25}$$

where

$$\mu_x \quad = \quad \Sigma_{z_i=0}^{N_L-1}z_i\left(\Sigma_{z_j=0}^{N_L-1}p(z_i,z_j)\right) \tag{A.26}$$

$$\mu_y \quad = \quad \Sigma_{z_j=0}^{N_L-1}z_j\left(\Sigma_{z_i=0}^{N_L-1}p(z_i,z_j)\right) \tag{A.27}$$

$$\sigma_x \quad = \quad \sqrt{\Sigma_{z_i=0}^{N_L-1}(z_i-\mu_x)^2\cdot\Sigma_{z_j=0}^{N_L-1}p(z_i,z_j)} \tag{A.28}$$

$$\sigma_y \quad = \quad \sqrt{\Sigma_{z_j=0}^{N_L-1}(z_j-\mu_y)^2\cdot\Sigma_{z_i=0}^{N_L-1}p(z_i,z_j)} \tag{A.29}$$

$$p_{x+y}(k) \quad = \quad \Sigma_{z_i,z_j=0}^{N_L-1}p(z_i,z_j) \tag{A.30}$$

$$\text{with } z_i+z_j \quad = \quad k \text{ and } k=0,1,2,...,2(N_L-1)$$

$$p_{x-y}(k) \quad = \quad \Sigma_{z_i,z_j=0}^{N_L-1}p(z_i,z_j) \tag{A.31}$$

$$\text{with } |z_i-z_j| \quad = \quad k \text{ and } k=0,1,2,...,N_L-1$$

$$\mu_{x-y} \quad = \quad \Sigma_{z_i=0}^{N_L-1}z_i p_{x-y}(z_i) \tag{A.32}$$

and N_L is the number of gray-levels, z_i denotes a gray level. $p(z_i)$ or $p(z_i,z_j)$ denotes the number of occurrences of a gray level z_i or a pair of gray levels z_i and z_j, respectively. Additionally, first order statistics could derived directly from the histogram:

$$\text{Mean: } \mu \quad = \quad \Sigma_{z_i=0}^{N_L-1}z_i p(z_i) \tag{A.33}$$

$$\text{Variance: } \sigma^2 \quad = \quad \Sigma_{z_i=0}^{N_L-1}(z_i-\mu)^2 p(z_i) \tag{A.34}$$

$$\text{Skewness: } \mu_3 \quad = \quad \sigma^{-3}\Sigma_{z_i=0}^{N_L-1}(z_i-\mu)^3 p(z_i) \tag{A.35}$$

$$\text{Kurtosis: } \mu_4 \quad = \quad \sigma^{-4}\Sigma_{z_i=0}^{N_L-1}(z_i-\mu)^4 p(z_i)-3, \tag{A.36}$$

The second order statistics can be used to describe the texture of an image. For comparison purposes (see Sec. 4.3) textures collected in Tab.A were computed.

	Feature	Distance π
1.	Variance	from the histogram
2.	Second Order Angular Moment	1
3.	Correlation	1
4.	Inverse Difference Moment	1
5.	Sum Average	1
6.	Difference Variance	1
7.	Second Order Angular Moment	2
8.	Contrast	2
9.	Correlation	2
10.	Inverse Difference Moment	2
11.	Sum Average	2
12.	Difference Variance	2
13.	Inverse Difference Moment	3
14.	Second Order Angular Moment	4
15.	Inverse Difference Moment	4
16.	Sum Average	4
17.	Second Order Angular Moment	5
18.	Sum of Squares	5
19.	Inverse Difference Moment	5
20.	Sum Average	5

Table A.2. List of 20 GLCM features computed for different π and $\Theta = 0°, 45°, 90°, 135°$.

Bibliography

[1] N. Ahuja and B. J. Schachter. Image models. *Computing Surveys*, 13(4):373–397, 1981.

[2] J. Arabas. *Lectures on Evolutionary Algorithms (in Polish)*. WNT, 2001.

[3] S. Belongie, J. Malik, and J. Puzicha. Shape matching and object recognition using shape context. *IEEE Trans. Pattern Anal. Mach. Intell.*, 24(4):509 – 522, 2002.

[4] A.H. Bennett, H. Jupnik, H. Osterberg, and O.W. Richards. *Phase Microscopy: Principles and Applications*. Wiley & Sons, New York, 1951.

[5] M. Berthod, Z. Kato, S. Yu, and J. S. Zerubia. Bayesian image classification using Markov Random Fields. *Image and Vision Computing*, 14:285–295, 1996.

[6] J. Besag. On the statistical analysis of dirty pictures. *J. Roy. Stat. Soc. B*, 48:259–302, 1986.

[7] S. Beucher. The watershed transformation applied to image segmentation. In *1Oth Pfefferkorn Conf. on Signal and Image Processing in Microscopy and Microanalysis*, pages 299–314, Cambridge, UK, 1992. Scanning Microscopy International.

[8] H. Beyer. *Theorie und Praxis des Phasenkontrastverfahrens*. Akademische Verlagsgesellschaft Geest und Portig, Leipzig, 1965.

[9] D. S. Broomhead and D. Lowe. Multi-variable functional interpolation and adaptive networks. *Complex Systems*, 2:321–355, 1988.

[10] J. Cai and Z.Q. Liu. Pattern recognition using Markov Random Field models. *Pattern Recognition*, 35:725–733, 2002.

[11] T. E. Campos, I. Bloch, and R. M. Cesar. Feature selection based on fuzzy distances between clusters: first results on simulated data. Technical report, Computer Science Department - IME - USP, Sao Paulo, Brazil, 2000.

[12] R. Chellappa. *Digital Image Processing*. IEEE Computer University Press, Los Alamos, California, 1993. TUD Library.

[13] Y. Q. Chen, M. S. Nixon, and D. W. Thomas. Statistical geometrical features for texture classification. *Pattern Recognition*, 28(4):537–552, 1995.

[14] W. Chung-Ming, C. Yung-Chang, and H. Kai-Sheng. Texture features for classification of ultrasonic liver images. *IEEE Trans. Med. Imag.*, 11(2):141–151, 1999.

[15] J.C. Clemens and C.A. Worby. Use of double-stranded RNA interference in Drosophila cell lines to dissect signal transduction pathways. *Proc Natl Acad Sci USA*, 97:6499–6503, 2000.

[16] C. Conrad, H. Erfle, P. Warnat, N. Daigle, T. Loerch, J. Ellenberg, R. Pepperkok, and R. Eils. Automatic identification of subcellular phenotypes on human cell arrays. *Genome Research*, 14:1130–1136, 2004.

[17] M. K. Cowles and B. P. Carlin. Markov chain Monte Carlo convergence diagnostics: A comparative review. *Journal of the American Statistical Association*, 91(434):883–904, 1996.

[18] M.C. de Andrade. An interactive algorithm for image smoothing and segmentation. *Electronic Letters on Computer Vision and Image Analysis*, 4(1):32–48, 2004.

[19] H. Deng and D. A. Clausi. Unsupervised image segmentation using a simple MRF model with a new implementation scheme. *Journal of the Pattern Recognition Society*, 37(12):2323–2335, 2004.

[20] J. Dias and J. Leitao. Wall position and thickness estimation from sequences of echocardiographic images. *IEEE Trans. Med. Imag.*, 15(1):25–38, 1996.

[21] R. O. Duda, P. E. Hart, and D. G. Stork. *Pattern Classification*. John Wiley & Sons, 2002.

[22] R. M. Dufour and E. L. Miller. Template matching based object recognitioin with unknown geometric parameters. *IEEE Trans. Im. Proc.*, 11(12):1385–1396, 2002.

[23] Landers E.S. Initial sequencing and analysis of the human genome. *Nature*, 409:860–921, 2001.

[24] B. Fisher, S. Perkins, A. Walker, and E. Wolfart. Hypermedia image processing reference. online, Retrieved from http://www.cee.hw.ac.uk/hipr/.

[25] B. Flach, E. Kask, D. Schlesinger, and A. Skulish. Unifying registration and segmentation for multi-sensor images. In Luc Van Gool, editor, *Proceedings of the 24th DAGM Symposium on Pattern Recognition*, volume 2449 of *Lecture Notes in Computer Science*, pages 190–197. Springer Verlag, 2002.

[26] E. B. Ford. *Ecological Genetics*. Chapman and Hall, London, 1975.

[27] J. Frank and M. Radermacher. Spider and web: Processing and visualization of images in 3d electron microscopy and related fields. *J Struct Biol*, 116:190–199, 1996.

[28] N. Freuderberg, C. Kortsik, and A. Ross. *Grundlagen der Zytopathologie*. Karger, 2002.

[29] K. Fukunaga and L.D. Hostetler. The estimation of the gradient of a density function with application in pattern recognition. *IEEE Transaction on Information Theory*, 21:32–40, 1975.

[30] T. Fumiaki and S. Tsuji. *Computer Analysis of Visual Textures*. Kluwer Academic Publisher, Boston, 1990.

[31] R. Galar. *Soft selection in random global Adaptation in R^n (in Polish)*. Monograph series No.84. Sc. Works of Inst. of Engineering Cybernetics, Wroclaw Univ. of Technology, 1984.

[32] R. Galar. Simulation of local evolutionary dynamics of small populations. *Biological Cybernetics*, 65:37–45, 1991.

[33] R. Galar. Evolutionary simulations and insights into progress. In A.V. Sebald and L.J. Fogel, editors, *Proceedings of the Third Annual Conference on Evolutionary Programming*, World Scientific, pages 344–351, San Diebo CA, 1994.

[34] S. Geman and D. Geman. Stochastic relaxation, Gibbs distribution and the Bayesian restoration of images. *IEEE Trans. Pattern Anal. Mach. Intell.*, 6(6):721–741, 1984.

[35] C. Genovese. Statistical inference in functional magnetic resonance imaging. Technical Report 674, Carnegie Mellon Department of Statistics, 1997.

[36] G. Glab, K. Florczak, J. Jaronski, and T. Licznerski. *Cyto-gynaecological diagnoses in phase contrast microscopy (in Polish)*. Blackhorse Publishing, 2001.

[37] V. Grau, A.U.J. Mewes, and M. Alcaniz. Improved watershed transform for medical image segmentation using prior information. *IEEE Trans. Med. Imag.*, 23(4):447–458, 2004.

[38] G.J. Hannon. RNA interference. *Nature*, 418:244–251, 2002.

[39] R. M. Haralick, K. Shanmugam, and I. Dinstein. Texture parameters for image classification. *IEEE Trans. Syst. Man Cybern.*, 3:610–621, 1973.

[40] S. Herlidou, I. Idy-Peretti, R. Grebe, F. Grados, N. Lecuyer, and P. Fardellone. Quantitative evaluation of trabecular bone structure by calcaneus MR images texture analysis of healthy volunteers and osteoporotic subjects. In *Engineering in Medicine and Biology Society, Proceedings of the 23rd Annual International Conference of the IEEE*, volume 3, pages 2340–2342, 2001.

[41] K. Huang and R.F.Murphy. From quantitative microscopy to automated image understanding. *Journal of Biomedical Optics*, 9(5):893–912, 2004.

[42] A. K. Jain, R. P.W. Duin, and J. Mao. Statistical pattern recognition: A review. *IEEE Trans. Pattern Anal. Mach. Intell.*, 22(1):4–37, 2000.

[43] J. Jenny. *Die Phasenkontrastmikroskopie in der taeglichen Praxis*. Jenny und Artusi, 1977.

[44] Q. Ji, J. Engel, and E. Craine. Texture analysis for classification of cervix lesions. *IEEE Trans. Med. Imag.*, 19(11):1144–1149, 2000.

[45] Z. Kato. *Multi-scale Markovian Modelisation in Computer Vision with Applications to SPOT Image Segmentation*. PhD thesis, INRIA Sophia Antipolis, France, 1994.

[46] Z. Kato, T. C. Pong, and J. C. M. Lee. Color image segmentation and parameter estimation in a Markovian framework. *Pattern Recognition Letters*, 22(3-4):309–321, 2001.

[47] Z. Kato, J. Zerubia, and M. Berthod. Satellite image classification using a modified Metropolis dynamics. In *IEEE Int. Conf. on Acoust. Speech and Sig. Proc.*, pages 573–576, 1993.

[48] J.H. Kim, S.K. Kuo, and C. H. Menq. An ultraprecision six-axis visual servo-control system. *IEEE Trans Robotics Automation*, 21(5):985–993, 2000.

[49] S. Kirkpatrick, C. D. Gelatt, and M. P. Vecchi. Optimization by simulated annealing. *Science*, 220(4598):671–680, 1983.

[50] J. Kittler, J. Illingworth, and J. Figlein. Threshold selection based on a simple image statistic. In *Comp. Vision Graph. Image Proc*, volume 30, pages 125–147, 1985.

[51] R. Kittler and F. Buchholz. RNA interference: gene silencing in the fast line. *Seminars in Cancer Biology*, 13:259–265, 2003.

[52] R. Kittler, L. Pelletier, A. Heninger, M. Slabicki, M. Theis, L. Miroslaw, I. Poser, H. Grabner, K. Kozak, J. Wagner, V. Surendranath, C. Richter, W. Bowen, B. Habermann, A.A. Hyman, and F. Buchholz. Genome-wide RNAi profiling of cell cycle progression in human tissue culture cells. *Nature*, 2006. submitted.

[53] R. Kittler, G. Putz, L. Pelletier, I. Poser, A.K. Heninger, D. Drechsel, S. Fischer, I. Konstantinova, B. Habermann, H. Grabner, M.L. Yaspo, H. Himmelbauer, B. Korn, K.Neugebauer, M.T. Pisabarro, and F. Buchholz. An endoribonuclease-prepared siRNA screen in human cells identifies genes essential for cell division. *Nature*, 432:1036–40, 2000.

[54] T. Kivioja, J. Ravantti, A. Verkhovsky, E. Ukkonen, and D. Bamford. Local average intenstiy-based method for identifying spherical particles in electron micrographs. *J Struct Biol*, 131:126–134, 2000.

[55] J. P. Lewis. Fast normalized cross-correlation. *Vision Interface*, pages 120–123, 1995.

[56] O. Lezoray, A. Elmoataz, H. Cardot, and M. Revenu. A color morphological segmentation. 2000.

[57] S.Z. Li. *Markov Random Field Modeling in Computer Vision*. Springer-Verlag, 2001.

[58] S. J. Ludtke, P.R. Baldwin, and W Chiu. EMAN: Semiautomated software for high-resolution single-particle reconstruction. *J Struct Biol*, 128:82–97, 1999.

[59] N. Malpica, A. Santos, A. Tejedor, A. Torres, M. Castilla, P. Garcia-Barreno, and M. Desco. Automatic quantification of viability in epithelial cell cultures by texture analysis. *J Microsc*, 209(1):34–40, 2003.

[60] I.M. Boier Marti, D. C. Marinescu, R. E. Lynch, and T. S. Baker. Identification of spherical virus particles in digitized images of entire electron micrographs. *J Struct Biol*, 120:146–157, 1997.

[61] A. Materka, P. Cichy, and J. Tuliszkiewicz. Texture analysis of X-ray images for detection of changes in bone mass and structure. In M. K. Pietikainen, editor, *Texture Analysis in Machine Vision, Series in Machine Perception & Artificial Intelligence*, volume 40, pages 189–195, 2000.

[62] Sharp P.A. McManus M.T. Gene silencing in mammals by small interfering RNA. *Nat Rev Genet*, 3:737–747, 2002.

[63] N. Metropolis, A. W. Rosenbluth, M.N. Rosenbluth, A.H. Teller, and E. Teller. Equations of state calculations by fast computing machines. *J. Chem. Phys.*, 21:1097–1091, 1953.

[64] Z. Michalewicz. *Genetic Algorithms + Data Structures = Evolution Programs*. Springer, 2002.

[65] G. Miniello. *Colposcopy and Phase Contrast Microscopy*. CIC Edizioni Internationale, 1998.

[66] G. Miniello. *Vaginal Fungal Infections by Phase Contrast Microscopy*. CIC Edizioni Internationale, 2001.

[67] L. Miroslaw. Binary object filtering using logical operators (in Polish). In K.Tchon, editor, *Advances in Robotics*, volume Robot control with perception, pages 21–28, Warsaw, 2005. Communication and Connection Publishers.

[68] L. Miroslaw, A. Chorazyczewski, F. Buchholz, and R. Kittler. Ea validation method in detection of mitotic cells. In *8th National Conf. Evolutionary Algorithms and Global Optimization*, Korbielow, 2005.

[69] L. Miroslaw, A. Chorazyczewski, F. Buchholz F., and R. Kittler. Correlation-based method for automatic mitotic cell detection in phase contrast microscopy. In M. Kurzynski, E. Puchala, M. Wozniak, and A. Zolnierek, editors, *Computer Recognition Systems*, pages 627–634. Springer, 2005.

[70] L. Miroslaw, K. Kozak, A. Chorazyczewski, L. Pelletier, and F. Buchholz. esiImage: An image-based analysis tool for the automated mitotic index determination of tissue culture cells (submitted). *Journal of Biomolecular Screening*, 2006.

[71] L. Miroslaw and F. Uhlemann. Automated detection of circular cells in images from contrast phase microscopy. In *Beitraege zur 38. Jahrestagung der Deutschen Gesellschaft fuer Biomedizinische Technik im VDE*, pages 68–70, TU Ilmenau, September 2004. VDE.

[72] M. Mitchel. *An Introduction to Genetic Algorithms*. MIT-Press, 1996.

[73] A. Mohammad-Djafari and K. Sauer. Shape reconstruction in X-ray tomography from a small number of projections using deformable models. In *Proc. CGIP*, pages 170–176, 2000.

[74] L. Najman and M. Couprie. Watershed algorithms and contrast preservation. In *DGCI*, pages 62–71, 2003.

[75] B. Neumann, M. Held, U. Liebel, H. Erfle, P. Rogers, R. Pepperkok, and J. Ellenberg. High-throughput RNAi screening by time-lapse imaging of live human cells. *Nature Methods*, 3(5):385 – 390, 2006.

[76] W. V. Nicholson and R. M. Glaeser. Review: Automatic particle detection in electron microscopy. *J Struct Biol*, 133:90–101, 2001.

[77] W.V. Nicholson and R. Malladi. Correlation-based methods of automatic particle detection in electron microscopy images with smotothing by anisotropic diffusion. *J Microsc*, 213:119–128, 2004.

[78] J. Park and J.M. Keller. Snakes on the watershed. *IEEE Trans. Pattern Anal. Mach. Intell.*, 23(10):1201–1205, 2001.

[79] P. Perner. Classification of hep-2 cells using fluorescent image analysis and data mining. In J. Crespo, V. Maojo, and F. Martin, editors, *Medical Data Analysis*, pages 219–224. Springer Verlag, 2001.

[80] W. K. Pratt. *Digital Image Processing, Third Edition*. John Wiley & Sons, 2001.

[81] W. H. Press, S. A. Teukolsky, W. T. Vetterling, and B. P. Flannery. *Numerical Recipes in C*. Press Syndicate of the University of Cambridge, 2002.

[82] W. S. Rasband. ImageJ. Technical report, National Institutes of Health, Bethesda, Bethesda, Maryland, USA, 2006.

[83] T.W. Ridler and S. Calvard. Picture thresholding using an iterative selection method. *IEEE Trans. Syst. Man Cybern.*, 8:630–632, 1978.

[84] O. Ronneberger, E. Schultz, and H. Burkhardt. Automated pollen recognition using 3d volume images from fluoerescence microscopy. *Aeorobiologia*, 18(18):107–115, 2002.

[85] A. M. Roseman. Particle finding in electron micrographs using a fast local correlation algorithm. *Ultramicroscopy*, pages 225–236, 2003.

[86] J. C. Russ. *The Image Processing Handbook, Third Edition*. CRC Press, Boca Raton, 1998.

[87] M. Desco et al. Santos A., C. Ramiro. Automatic detection of cellular necrosis in epithelial cell cultures. In Kenneth M. Hanson Milan Sonka, editor, *Proceedings of SPIE*, volume 4322, pages 1836–1844, 2001.

[88] T. Schilling. Analysis and comparison of cell segmentation methods in the microscopy (in German). Master's thesis, Dresden Technical Univeristy, 2004.

[89] T. Schilling, L. Miroslaw, G. Glab, and M. Smereka. Towards rapid cervical cancer diagnosis: automated detection of cells in phase contrast images with texture features and active contours (accepted). *Journal of Gynecological Cancer*, 2006.

[90] H.S. Sheshadri and A. Kandaswamy. Detection of breast cancer by mammogram image segmentation. *J Can Res Ther*, 1(4):232–234, 2005.

[91] K. Siddiqi, A. Shokoufandeh, S. J. Dickinson, and S. W. Zucker. Shock graphs and shape matching. *International Journal of Computer Vision*, 35(1):13–32, 1999.

[92] V. Singh, D. C. Marinescu, and T. S. Baker. Image segmentation for automatic particle identification in electron micrographs based on hidden Markov Random Field models and expectation maximization. *J Struct Biol*, 145:123–141, 2004.

[93] W. Skarbek. *Representation methods of digital images (in Polish)*. Academic Publisher, Warsaw, 1993.

[94] S. Sternberg. Biomedical image processing. *IEEE Computer*, 16(1):22–34, 1983.

[95] P. Stoll and G. Dallenbach-Hellweg. *Cytology in Gynecological Practice: An Atlas of Phase-Contrast Microscopy*. Springer-Verlag, Berlin and Heidelberg, 1993.

[96] R. Tadeusiewicz and P. Korohoda. *Computer analysis and image processing (in Polish)*. Foundation of Progress and Telecomunication, Krakow, 1997.

[97] D. Tomazevic, B. Likar, and F. Pernus. Comparative evaluation of retrospecive shading correction methods. *J Microsc*, 208(3):212–223, December 2002.

[98] M. Tuceryan and A. K. Jain. Texture segmentation using voronoi polygons. *IEEE Trans. Pattern Anal. Mach. Intell.*, 12:211–216, 1990.

[99] M. Tuceryan and A. K. Jain. *The Handbook of Pattern Recognition and Computer Vision*, chapter Texture Analysis, pages 207–248. World Scientific Publishing Co., 1998.

[100] H. Vaucheret, C. Beclin, and M. Fagard. Post-transcriptional gene silencing in plants. *J Cell Sci*, 114:3083–91, 2001.

[101] B. Vikramaditya and B.J. Nelson. Visually guided microassembly using optical microscopes and active vision techniques. In *1997 IEEE Int Conf Robotics and Automation*, volume 4, pages 3172–3177, 1997.

[102] N. F. Vittitoe, R. Vargas-Voracek, and C.E. Floyd. Markov random field modeling in posteroanterior chest radiograph segmentation. *Medical Physics*, 26(8):1670–1677, 1999.

[103] N. Van Vliet. Image segmentation applied to cytology. Technical report, Laboratoire de Recherche et Developpement de l'Epita, Le Kremlin-Bictre cedex, France, 2003.

[104] D. Richter J. Vranic, D.V. Saupe. Tools for 3d-object retrieval: Karhunen-Loeve transform and spherical harmonics. In *2001 IEEE Fourth Workshop on Multimedia Signal Processing*, pages 293–298, 2001.

[105] R. F. Walker. *Adaptive Multiscale Texture Analysis With Application to Automated Cytology*. PhD thesis, Department of Electrical & Computer Engineering, The University of Queensland, 1997.

[106] R.F. Walker and P.T. Jackway. Statistical geometrical features - extensions for cytological texture analysis. In *The 13th International Conference On Pattern Recognition*, volume 2, pages 790–794, Vienna, Austria, 1996.

[107] H. Wang and D. Suter. False-peaks-avoiding mean shift method for unspervised peak-valley sliding image segmentation. In *VIIth Digital Image Computing: Techniques and Applications*, pages 581–590, 2003.

[108] A. R. Webb. *Statistical Pattern Recognition*. John Wiley & Sons, 2002.

[109] M.H.F. Wilkinson, T. Wijbenga, G. de Vries, and M.A. Westenberg. Blood vessel segmentation using moving-window robust automatic threshold selection. In *Int. Conf. on Image Processing*, volume 2, pages 1093–6, 2003.

[110] T. Wurflinger, J. Stockhausen, D. Meyer-Ebrecht, and A. Bocking. Robust automatic coregistration, segmentation, and classification of cell nuclei in multimodal cytopathological microscopic images. *Computerized Medical Imaging and Graphics*, 28(1-2):87–98, 2004.

[111] C. Xu and J. L. Prince. Snakes, shapes, and gradient vector flow. *IEEE Trans. Im. Proc.*, 7(3):359–369, 1998.

[112] C. C. Yang and F. W. Ciarallo. Optimized sensor placement for active visual inspection. *J Robotic Systems*, 18(1):1–15, 2000.

[113] S. X. Yu, R. Gross, and J. Shi. Concurrent object recognition and segmentation by graph partitioning. In *NIPS*, volume 9, pages 1383–1390, 2002.

[114] C.T. Zahn and R.Z. Roskies. Fourier descriptors for plane close curves. *IEEE Trans. Computer*, C-21:269–281, 1972.

[115] F. Zernike. Phase contrast, a new method for microscopic observation of transparent objects. *Physica*, 9:686–698, 1942.

Index

Glossary

assay

    An analysis or examination 3.0

cell line

    A permanently established cell culture that will grow indefinitely given the appropriate medium and conditions, thus making the cell line immortal 3.0

DAPI

    DAPI or 4',6-diamidino-2-phenylindole is a fluorescent stain that binds strongly to DNA. It is used extensively in fluorescence microscopy. 1.0

DNA

    A nucleic acid that carries the genetic information in the cell and is capable of self-replication and synthesis of RNA. DNA consists of two long chains of nucleotides twisted into a double helix and joined by hydrogen bonds between the complementary bases adenine and thymine or cytosine and guanine. The sequence of nucleotides determines individual hereditary characteristics (from Answers.com) 1.0

Fisher Linear Discriminant (FLD)

    Fisher's linear discriminant are used to find the linear combination of features which best separate two or more classes of objects or events. The resulting combinations may be used as a linear classifier, or more commonly in dimensionality reduction before later classification. 4.3, **4.3**

GFP

    The green fluorescent protein (GFP) is a protein from the jellyfish Aequorea victoria that fluoresces green when exposed to blue light. The GFP is usually much less harmful when illuminated in living cells. 1.0

Gibbs Random Field (GRF)

    A set of random variables F which configurations obey the Gibbs distribution 2.1, **2.1**

HeLa cell line

    an immortal cell line used in medical research. The cell line was derived from cervical cancer cells taken from Henrietta Lacks, who died from her cancer in 1951. (from Wikipedia) 3.0

Iterated Conditional Modes (ICM)

    a deterministic algorithm which maximizes local conditional probabilities sequentially. Proposed by Besag (1986) due to difficulties in maximizing the joint probability of an MRF 2.1, **2.1**, 4.2

Markov Random Field (MRF)

    Markov random field (MRF) theory provides a convenient and consistent way to model context-dependent entities such as image pixels and correlated features. This is achieved by characterizing mutual influences among such entities using conditional MRF distributions. 2.1, **2.1**, 4.2

Maximum a posteriori (MAP)

    the MAP estimation can be used to obtain a point estimate of an unobserved quantity on the basis of empirical data 2.1, **2.1**, 3.1

meniscus

The curved upper surface of a nonturbulent liquid in a container that is concave if the liquid wets the container walls and convex if it does not. 1.0

mitosis

the entire process of cell division including division of the nucleus and the cytoplasm 3.0

Pap smear

Pap test, Pap smear, or Papanicolaou test, medical procedure used to detect cancer of the uterine cervix. A scraping, brushing, or smear, is taken from the surface of the vagina or cervix and is prepared on a slide and stained for microscopic examination and cytological analysis. The appearance of the cells determines whether they are normal, suspicious, or cancerous. Although the test is 80% to 95% reliable, results termed suspicious may indicate infection or some abnormal condition other than cancer. The smear technique is also used to detect cancer of other tissues, e.g., in the bladder. The Pap test was developed by G. N. Papanicolaou and H. F. Traut in 1943. (The Encyclopedia of the Columbia University Press) 4.1

phenotype

The observable physical or biochemical characteristics of an organism, as determined by both genetic makeup and environmental influences. 3.0

photobleaching

Photobleaching is the destruction of a photochemical fluor by high-intensity light. In microscopy, photobleaching may complicate the observation of fluorescent molecules, since they will eventually be destroyed by the light exposure necessary to stimulate them into fluorescing. This is especially problematic in time-lapse microscopy (from answers.com) 3.2

RNA

Ribonucleic acid, a nucleic acid that transmits messages in the DNA to other elements in the cell (from gale Encyclopedia of Neurological Disorders). 1.0

staining

the use of a dye to color specimens for microscopic study 1.0

transfection

Introducing DNA into eukaryotic cells (with nucleus) 3.0